PERFORMANCE MEASURES FOR RESIDENTIAL PV STRUCTURAL RESPONSE TO WIND EFFECTS

A Thesis
Presented to
The Academic Faculty

by

Joseph Neal Goodman

In Partial Fulfillment
of the Requirements for the Degree
Doctor of Philosophy in the
School of Architecture

Georgia Institute of Technology
December 2015

PERFORMANCE MEASURES FOR RESIDENTIAL PV STRUCTURAL RESPONSE TO WIND EFFECTS

Approved by:

Professor Fried Augenbroe, Advisor
School of Architecture
Georgia Institute of Technology

Professor Russell Gentry
School of Architecture
Georgia Institute of Technology

Kevin Caravati
Georgia Tech Research Institute
Georgia Institute of Technology

Dr. David Banks
Solar and Special Services
CPP

Dr. Jason Brown
School of Architecture
Georgia Institute of Technology

Date Approved: August 19, 2015

This work is dedicated to my Father for sharing his love of the wind and to Wyatt and Leo who I hope will find loves of their own.

ACKNOWLEDGEMENTS

This thesis proposal and thesis work completed to date has been supported by the U.S. Department of Energy project D6596, SIMPLE BoS. Georgia Tech students, and faculty have enabled the accomplishments to date. Florida International University collaborated to implement the wind tunnel test and process measurements into pressure coefficients. Generous advise and patience have been provided by thesis committee members. Dr. Bruce Ellingwood provided insight into the structural code development process, intent and opportunities for improvement. Finally, the opportunity to work with Professor Augenbroe for the past five years has been valuable beyond a degree or title. My gratitude for his time and patience know no limit.

TABLE OF CONTENTS

LIST OF TABLES

LIST OF FIGURES

SUMMARY

This thesis applies structural reliability measures for the performance based design of residential PV system structures. These measures are intended to support designers in delivering systems with quantified and consistent reliability. Existing codified practices prescribe global factors (allowable stress design) and partial factors (load and resistance factor design) intended to provide an acceptable level of reliability as defined by historical practice. When applied to residential PV systems this prescriptive approach has two flaws, (1) calibration efforts needed to ensure consistency across structural system types have not kept up with the commercially available system types and (2) the actual expected reliability is not quantified and available to support decisions. The proposed reliability measures include probability of failure conditioned to wind speed in a fragility curve and the reliability index β, both of which are commonly used in performance based design. The approach is demonstrated through the application of the reliability measures to code compliant designs. Diverse system types are utilized to demonstrate how the existing code prescribed approach may lead to non-uniform structural performance. For each of the system types on which the reliability measures are demonstrated, a code compliant design is developed for three roof slopes, wind tunnel testing is conducted to provide an experimental measure of wind pressure coefficients, system specific fragility curves are generated to quantify the probability of failure conditioned to a set of wind speeds, and then, a site specific wind model is applied to produce a probability of failure and reliability index β. Through the performance based approach proposed in this thesis, two key outputs show non-uniform and unanticipated structural performance of PV systems designed according to the prescriptive code method. The two key outputs

which illustrate this finding are fragility curves which illustrate the probability of failure over a range of wind speeds and reliability index, β values which couple the structural and wind distributions for a single measure of reliability.

CHAPTER I

INTRODUCTION

1.1 Motivation

1.1.1 PV Balance of System Importance and characteristics

A power generation device such as a fuel cell or photovoltaic (PV) cell may require structural, electrical, pneumatic, or thermal functions for operation. The hardware, software and other technology required to fulfill these functions is generally characterized as the balance of system (BoS). In a solar PV system, a PV cell is a component of a PV module, the power generation device. Utilization of a PV module in applied[1] residential systems requires balance of system hardware including racking and electrical protection. As illustrated in Figure 1 racking is composed of module attachment hardware (mounting clamps), structural members (rails) and roof attachment hardware (L-feet) lag screws and flashing. Electrical protection is composed of wire management hardware and ground protection. Typically[2] all of this hardware is assembled on site by hardware and electrical installation professionals. The associated installation labor cost, a component of soft cost, is influenced by contextual and technological factors including system layout and racking and mounting hardware selection. For analysis purposes, labor and other soft cost, are often included in the general balance of system cost category. [59].[3] Until the 2010 Department of Energy hosted BoS workshop focused on cost reduction, the majority of federal and privately funded research was targeted at advancing PV cells and PV modules [28]. Due to

[1]building applied refers to systems installed in addition to a complete building system in lieu of building integrated in which the PV systems fulfills a part of the building envelope functionality.

[2]some approaches under are exploring factory assembly of subsystems

[3]PV inverters are often considered an independent power conversion component and not included in the balance of systems definition

great cell and module research and development success, along with external factors, PV markets have grown and system cost have declined. In an effort to achieve aggressive cost reduction goals , BoS cost and reliability are receiving increased industrial and scientific attention [73].

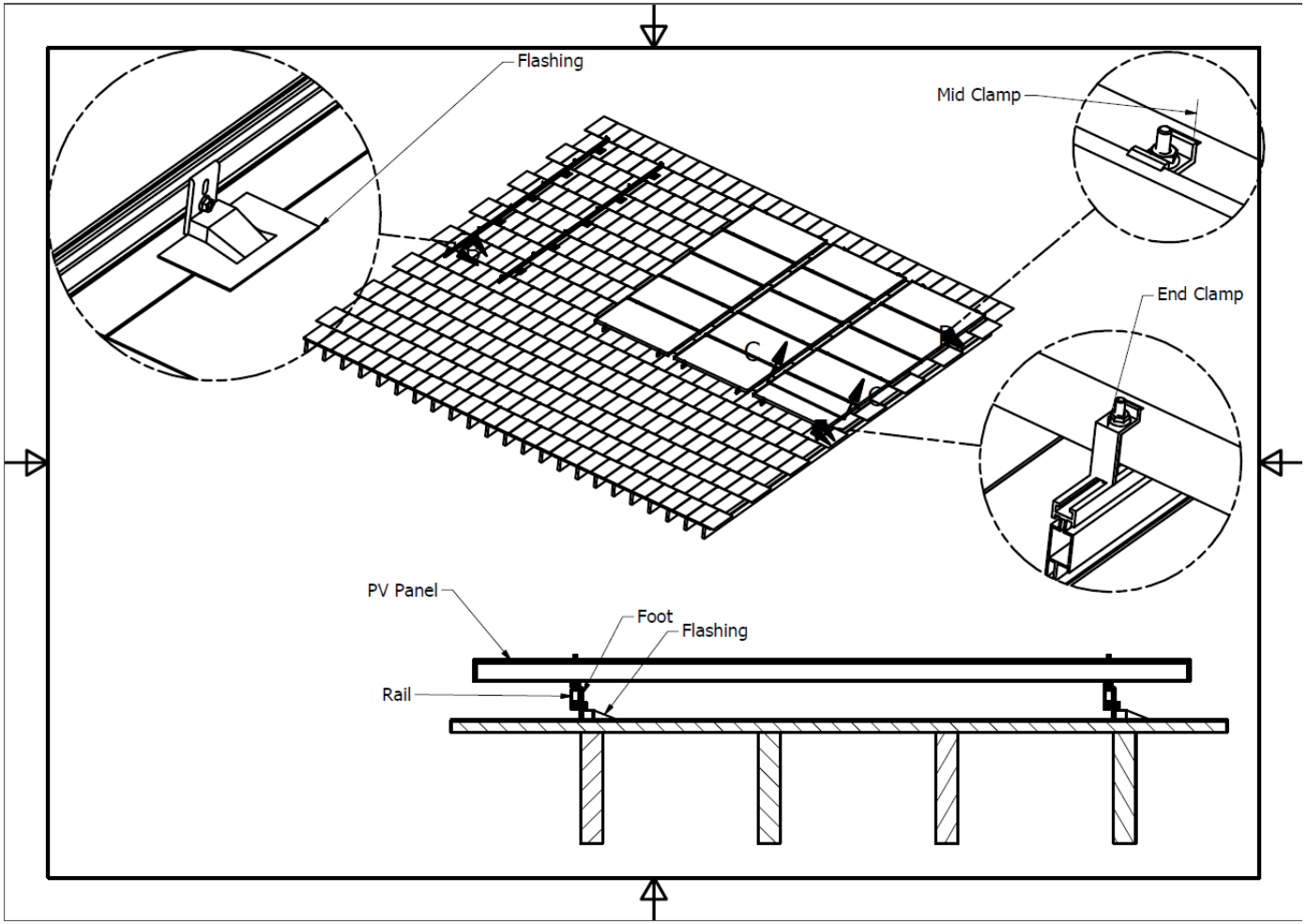

Figure 1: Typical residential PV system with 1-D rail

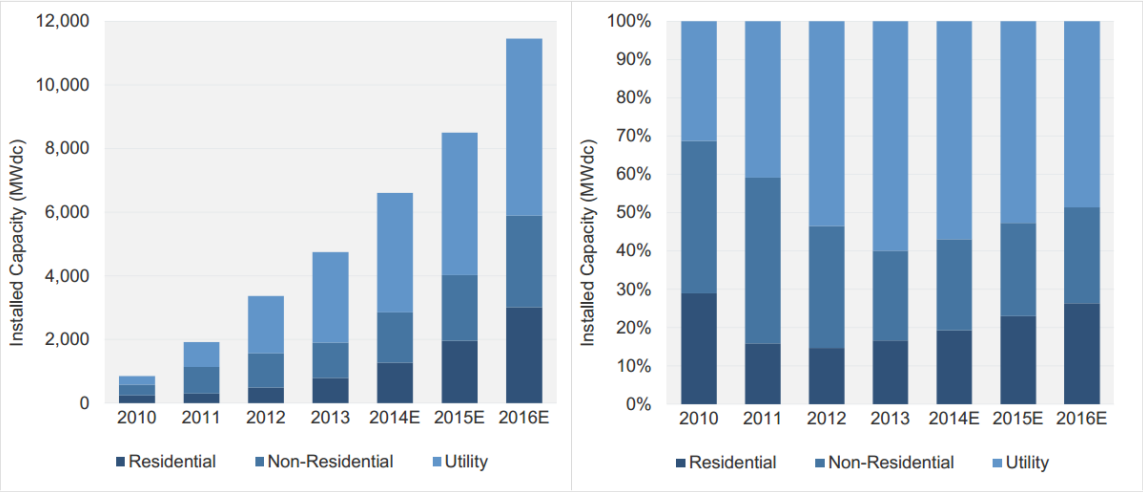

Figure 2: U.S. PV Installation actuals and forecast for 2010-2016 by sector. [49]

Among the areas of PV BoS investigation, reliability and risk management are critical for supporting continued adoption. The importance of safety risk management was highlighted in a recent response to a Florida public service commission request for comment on solar energy by Duke Energy with the following quote:

> All stakeholders interested in advancing solar in a sustainable way for Florida must be committed to safety first. Public safety, health, and power grid reliability should never come second to advancing any energy resource [30].

1.1.2 Balance of system drivers and stakeholders

Hardware cost and risk management are not the only drivers of PV balance of system design. Installation time, logistics, and layout flexibility have motivated development of divergent BoS technologies that all meet a common set of functional requirements. At a 2010 industry PV BoS workshop, the racking and electrical components of BoS were functionally described as the electrical system for aggregating and conveying power and the structural system for resisting natural forces. Forces applied to a PV system include self weight, wind, snow, and seismic. Analysis of the structural system

revealed that in most high growth PV markets, wind forces have the greatest influence of structural member sizing. Workshop attendees postulated that without wind loads on a PV system, structural cost could be reduced by 75% [18]. While reducing wind loads through improved aerodynamic design and understanding has resulted in cost reductions for commercial flat roof PV systems, wind loads have had little influence on the design of pitched roof residential PV systems [16].

Requirements associated with installation time, logistics cost and layout flexibility are reflected by system types introduced to the market over the past 5 years. The installation time required for positioning and attaching the roof attachment hardware is significantly greater in the U.S. than in Germany for reasons including the geometric imprecision of U.S. construction [59]. Technology advances have improved installation tolerance to as built U.S. roof conditions such as imprecise rafter spacing [22]. Logistical cost are influenced by the weight and length of racking structural members, rails, that must be transported to site and conveyed to the roof. Logistical cost have motivated elimination of continuous rails in favor of light weight discretized racking configurations. The rapid change in structural systems and continued drive for cost reduction further motivates an improved understanding of failure risk across prevalent residential PV system types.

1.1.3 Structural reliability

1.1.3.1 Theoretical basis

The "reliability" concept is loosely applied throughout the literature with varying implied and explicit definitions. Often the definition is excessively broad, for example if a reliable system is thought of as one that does not fail, then the definition neglects specificity of operating life and operating scenarios. Further, such a broad definition ignores inherent uncertainties that result in a statistical likelihood of failure. To address these shortcomings, ISO 2394 defines reliability as the "ability of a structure or structural element to fulfill the specified requirements, including the working life,

for which it has been designed [2]. According to this definition "requirements" shall be defined with three components: a structural failure definition, a service life, and a scenario of use. Structural failure definitions are specified by the structural states beyond which the performance requirements are no longer satisfied; these states are commonly referred to as limit states [6]. In other words, a limit state is the threshold condition for failure. For example, a PV system limit requirement may specify that the structural rails shall remain in an elastic state below the yield stress. The structures service life, defined in the time domain commonly with units of years, is either established by the governing structural code or by the structures owner. For example, EN1990 establishes a design working life of 10-25 years for replaceable structural parts [3]. For many building applied PV system components, this definition may be appropriately adopted. A scenario of use is specified through load combinations which account for compatible load effects that may occur simultaneously [6]. For example, a load combination may account for the probable simultaneous occurrence of gravity and wind load effects [11]. Load combinations are necessary because in actual scenarios of use single load rarely occurs in isolation. In combination limit states, service life, and load combinations provide a basis for defining reliability requirements and more broadly contribute to the foundation for structural reliability.

A structure's reliability is commonly expressed through the probability of failure at a given hazard level as found in fragility models or over a specified time period as found in P_f. When expressing P_f over a time period, the reliability index β is often used because it is a more descriptive measure of reliability related to P_f through Equation 1

$$\beta = -\Phi_u^{-1}(P_f) \tag{1}$$

where $-\Phi_u^{-1}()$ denotes the inverse standard normal distribution function.

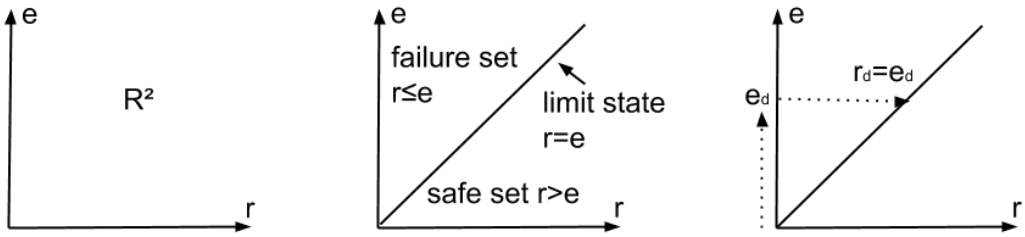

Figure 3: Theoretical deterministic structural design process

Both fragility curves and single reliability measures P_f or β are often useful together to provide a complete quantification of the risk because, where P_f and β convolute structural attributes with scenarios of use, fragility curves provide a primitive structural performance measure by conditioning the probability of failure to the hazard, wind speed. In order to further clarify the meaning of each reliability measure, context on the probabilistic nature of structural design must be provided.

Generally, structural design may be viewed as the combined processes of determining load effects, for use in load combinations, along with designing structural systems to have adequate resistance as defined by limit states. Depending on the design and the scenario of use, load effects e may take a value from the real set, $\mathbb{R}$ (S is also commonly used to represent load effects due to the prevalence of stress design). Similarly, a structural system may be designed with resistance, r, from the real set (Figure 3 left). Consequently a design may be characterized by the combination of design load effect, e_d and design resistance r_d noted as (r_d, e_d). As shown in figure 3 (center) (r_d, e_d) may exist anywhere in the real domain which is divided into two sets. Cases where $r_d \leq e_d$ are said to belong to the failure set according to the limit state definition, while cases where $r_d > e_d$ belong to the safe set. Graphically the limit state is shown to be the condition that separates the safe set from the failure set with the limit state included in the failure set. Mathematically the limit state, G, is shown to occur when $r_d = e_d$ and in alternative form $r_d - e_d = 0$ which is more commonly represented with Equation 2.

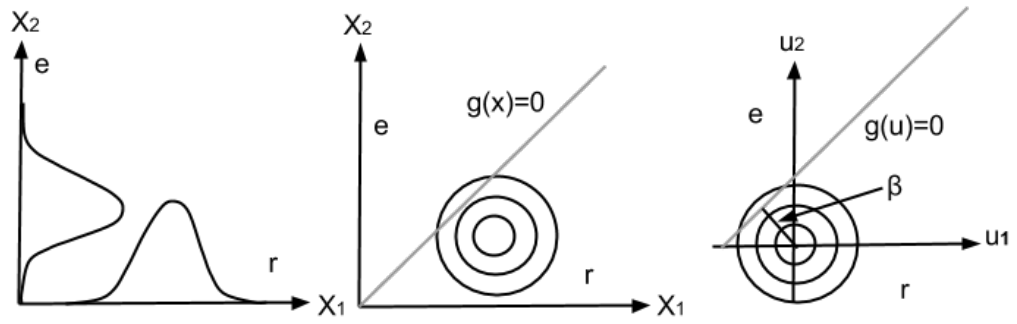

Figure 4: General probabilistic structural design process

$$G(X) = O \tag{2}$$

In a theoretical deterministic case where a designer is able to specify an exact value for e_d, the designer may engineer the structure with strength r_d (or stiffness) just greater than the limit state as illustrated in 3 (right).

Despite the simplicity of the aforementioned theoretical process, the structural engineering community has recognized neither e_d nor r_d are deterministic values because "uncertainties in structural performance can never be entirely eliminated and must be taken into account when designing any construction work" [5]. Uncertainties are recognized to occur throughout the basic set of variables $X = [x_1, ...x_n]$ characterizing material properties, geometries, load effects and model uncertainties from which r and e are determined [5]. Consequently, r and e must be treated as random variables, with example probability distributions for r and e illustrated in Figure 4 (left). Random variables r and e are not compatible with deterministic design methods and necessitate a probabilistic approach. The theory of structural reliability has been developed to meet structural engineering requirements under uncertainty. Figure 4 (center) represents a general approach for structural reliability where the stochastic distribution of load effects is characterized and the structural resistance is engineered such that random combinations of r and e have a statistically acceptable likelihood

of $e \geq r$. Transformation of the limit state from $G(x)$ to $G(u)$ by normalizing the random variables according to Equation 3 provides a geometric interpretation of the reliability index β shown in Figure 4 (right) and mathematical definition according to Equation 4 [35].

$$U_i = \frac{X_i - \mu_{xi}}{\sigma_{xi}} \tag{3}$$

$$\beta = \frac{\mu_M}{\sigma_M} \tag{4}$$

Historically, limit state design has been incorporated into multiple prescriptive methods. Each method has been structured with the intent to ensure that a design falls within the safe set through the use of coefficients or factors that create a safety margin between the design and limit state. Each of these methods rely on a linear limit states as shown in Figures 3 and 4 or utilization of linear approximation of the limit state. For a non-linear limit state a linear approximation is made using the tangent line through the most central failure point (on the limit state)[29]. Implementation of linear approximation methods is beyond the scope of this thesis, interested readers are referred to the bibliography.

1.1.3.2 Design methods in practice

In practice, three prescriptive methods have been utilized in U.S. codes to ensure structural reliability, these include permissible stress, global safety factor, and partial factor method. A brief background will follow on each method.

The permissible stress method reduces the critical stress to a permissible level based on coefficient, K as shown in Equation 5 and 6.

$$\sigma_{max} < \sigma_{per} \tag{5}$$

Where

$$\sigma_{per} = \frac{\sigma_{crit}}{k} \tag{6}$$

Coefficient k is greater than 1 and is intended to account for all sources of uncertainty. While simple procedurally, shortcomings exist because it is difficult to analyze which sources of uncertainty are accounted for and also precludes an engineer from calibrating the coefficient for different levels of uncertainty. Further, permissible stress does not allow for a more efficient design through global analysis methods including stress redistribution, ductility or other global behavior [5].

A second prescriptive method, the global safety factor method, only partly addresses the short comings of permissible stress. A broad approach is taken by prescribing a minimum safety factor, S_o that describes the ratio of resistance, R to load effects, E according to Equation 7 which adopts capital notation to denote random variables.

$$s = \frac{R}{E} > S_o \tag{7}$$

In determination of the resistance, global behavior may be taken into account. However, the single safety factor still lacks transparency required for calibration.

More recently introduced, the partial factor method addresses the remaining shortcoming by replacing the global factor with partial factors. This method accounts for specific sources of uncertainty and ensures through Equation 8 the design value of load effect, E_d do not exceed the design value of resistance, R_d.

$$E_d(F_d, f_d, a_d, \theta_d) < R_d(F_d, f_d, a_d, \theta_d) \tag{8}$$

As shown, E_d and F_d are dependent on design values for structural actions F_d, material properties f_d, dimensions a_d and model uncertainty θ_d. Further, each design value X_d is determined through applying factors to the respective characteristic value

X_k. Depending on the design value, factors may include partial factors γ and reduction factors Ψ. While this does constitute a significant improvement improvement most common implementations of the partial factor method including the ASCE version Load and Resistance Factor Design (LRFD) do not incorporate calibration for specific structural failure mode combinations. Consequently in practice the partial factor method commonly fails to provide quantified reliability. Further, in the absence of quantified reliability it may not be reasonable to assume the method delivers consistent reliability either.

As described, common to each method is the use of a linear limit state or linear approximation to provide a simple method for meeting reliability requirements. A limitation of this method is a failure to provide uniform reliability across structures [5]. Alternatively, when a non-linear limit is not approximated as linear, the design may exist any where along the acceptable probability contour to provide a uniform measure of safety according to $G(X) > 0$. Typically, this method results in a concave limit state which ensures that any design point falling between two limit state points falls within the safe set. This approach is the basis of "exact" methods including Monte Carlo analysis which have been more recently adopted in performance based reliability codes. The EU code EN1990 provides a performance path based on meeting target reliability levels with quantified design values for probability of failure P_d and reliability index β_d. Performance based methods will be further discussed in Chapter 3. Similarly, ASCE 7-10 introduced an allowance for performance-based procedures with the following section:

> Structural and nonstructural components and their connections shall be demonstrated by analysis or by a combination of analysis and testing to provide a reliability not less than that expected for similar components designed in accordance with the Strength Procedures of Section 1.3.1.1 when subject to the influence of dead, live, environmental, and other loads.

Consideration shall be given to uncertainties in loading and resistance.

. Under this provision a PV system, installed on residential home with occupancy category II, subject to sudden collapse is required to have a probability of failure $P_f = 3.0X10^{-5}/yr$ or $\beta = 3.0$ for a 50 year service period.

1.1.4 Fragility curves and probability of failure: risk management methods in practice

Currently, structural life safety risk is managed locally by a city or county building code official who may require stamped engineering drawings and Underwriter Laboratory (UL) certification. Stamped engineering drawings provide documentation that the system's structural design complies with the structural building code. This process is intended to ensure that the structure has an acceptable likelihood of failure during a design wind event. The design wind event is based on the prescribed recurrence interval for the occupancy category. In the U.S. building code, the threshold for acceptable performance is typically based on historical practices and not quantified as an explicitly accepted level [41]. In contrast the EU structural code probabilistic methods are more mature and more commonly used in practice. The result is that a structure designed according to EN1990 likely demonstrate compliant performance with a calculated β value while this is a nascent practice in the U.S. especially on residential scale projects.

State of art structural risk management has moved beyond factored design methods to better quantify the risk to building systems from earthquake and hurricane hazards. Performance engineering efforts focused on building response to earthquake hazards have identified the need to provide stakeholders with quantified performance measures. Stakeholders are recognized to be diverse in origin and may include building owners, financiers, and the public. Stakeholder concerns may be equally diverse including not only life safety risk but also operational risk, financial risk, repair cost and serviceability [32].

Performance based engineering commonly utilizes performance measures to synthesize risk analysis for communication with decision makers. These measures include fragility curves and the reliability metrics, probability of failure and reliability index, β. An important distinction between fragility curves and reliability metrics lies in the conditional nature of fragility curves. As shown in Figure 5 a single fragility curve quantifies the conditional probability of failure along the y-axis given a specific hazard level or structural demand on the x-axis, such as wind speed [75]. Multiple curves are commonly plotted together for two purposes (i) illustration of the fragility of a single technology with multiple limit states and (ii) illustration of fragility for multiple technology or component options with a common limit state. Regardless of the specific purpose, a few noteworthy characteristics are common to all fragility curves, a low demand region with 0 probability of failure and a high demand region with certain failure. In between, the fragility curve illustrates the probability of failure over a range of demand values. Fragility curves are commonly preferred by engineers because they provide explicit communication about the structural response of a system without convoluting the analysis with probabilistic demand models. In contrast, probability of failure metrics, incorporate a probabilistic demand model into a coupled analysis to derive a single scalar value that quantifies the expected probability of failure over a specified operating life such as 1 year or 25 years. Ultimately, the probability of failure is most useful for understanding structural risk in a specific location or with a specific demand model, and is often used by financial stakeholders to determine warranty reserves. Multiple methods exist in practice for the derivation of demand models, they commonly depend on historical data and mathematical models which both have limits of accuracy. Further, historical weather models have limited ability to predict future weather because weather patterns and events are becoming more extreme due to global warming. Nevertheless, fragility analysis and probability of failure analysis are the two available measures for synthesizing and reporting structural

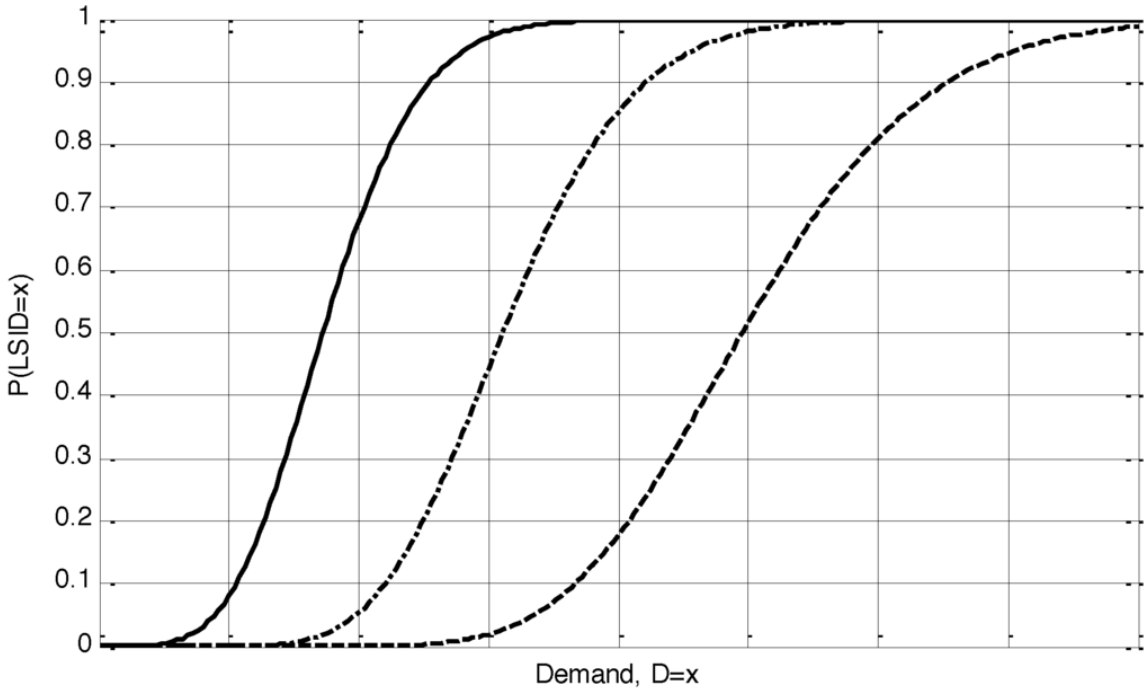

Figure 5: illustration of multiple fragility curves [75]

risk management analysis. Each of these measures play a critical and complementary role in this thesis.

1.2 Objective scope and limitations

The research objective of this thesis is to support the design of distributed PV systems by providing decision makers with explicit performance measures for PV system structural reliability.

The thesis is structured to motivate application of reliability measures, provide a theoretical and methodological basis, and a description and demonstration of the approach. The demonstration is completed through a sequence of case studies performed on three system types applied to three roof angles in multiple configurations for a total of 30 design cases. The design cases have been selected to support the motivation and evaluation of hypotheses presented in each chapter. The theoretical and methodological basis is structured to illustrate critical points needed to sustain the argument that reliability measures should and can be applied to residential PV

systems. The methodological sections are not a replacement for the foundational literature found in the bibliography. Systems types used in this thesis may appear similar to referenced commercially available system types but have been intentionally altered. This thesis in no way attempts to make claims regarding actual commercial systems and the specific results presented in this thesis should not be used for assessment of any commercially available systems.

1.3 Methodological road map

The proposed methodology to measure PV system structural performance through fragility and probability of failure risk measures is predicated on the following four assumptions:

1) Typically engineers utilize simplified reliability methods provided in the building code to establish design loads and resistance.

2) The structural building code's intent is to ensure acceptable structural reliability through the application of safety factors that shift the design load from an unknown value to one that has adequately low probability of exceedance.

3) Both the design load and resistance are unknown and best modeled as random variables because the variables that affect each are uncertain and best treated as random variables. In the absence of uncertainty, a safe system would constitute one in which the load is just less than resistance for the most demanding scenario of use; no safety factors would be required.

4) The building code accomplishes multiple objectives which include but are not limited to imposing a level of safety accepted by society and simplifying the structural reliability method for the community of practice.

Table 1 [15] contextualizes ASD and LRFD code methods in a hierarchy of structural reliability methods. ASCE code methods are considered a simplified "level 1"

reliability method because they eliminate probabilistic methods from practice by applying safety factors to nominal or characteristic [4] values as described in assumption 4. To support the establishment of safety factors a community of experts makes a statistical model for each random variable based on their collective understanding and believes [33]. The foundation for our current statistical modeling of the random variables that influence wind loads was made by at least 20 experts from industry, academia, and practice who individually demonstrated expertise in the 1980's and 1990's, then came together with facilitation by Bruce Ellingwood to codify their collective understanding through the statistical process of a Delphi. Through two rounds of questions and controlled feedback the group reached consensus on each variables uncertainty [33]. Knowledge of the uncertainty in each random variable allows for a factor to be derived which in combination with the mean value produces a design value with acceptably low probability of exceedance. The threshold for acceptably low probability of exceedance is based on the level of reliability found in historical practice. This practice is premised on the assumption that if the risk was not accepted by society then change would have been instigated by stakeholders. Further, the simplified level 1 approach implies a belief that stakeholders do not require an explicit quantification of reliability.

For the numerous scenarios in which a quantified reliability measure enables improved decision making a series of options exist with increasing accuracy. Common to each of the quantified methods is the direct use of random variable distributions. One option, second order moment methods utilizes the mean and coefficient of variation of each random variable in a limit state function to estimate β, the reliability index and probability of failure [15].

[4] A nominal value is differentiated by a lack of statistical implication such as mean value and does not imply a probabilistic distribution

Table 1: Hierarchy of structural reliability methods [15]

Level	**Calculation Method**	**Probability Distributions**	**Limit State Functions**	**Results**
1 Code methods	Safety factor with nominal values	Not used	Linear usually	Partial factors
2 Second Moment methods	Second moment algebra	Normal distributions implied	Linear	β factor and nominal failure probability
3 "Exact" methods	Random Variable Transformation[5]	normal distributions	Approximated as linear	Failure probability
	Monte Carlo	Any	Any form	Failure probability

$$\beta = \frac{\mu_M}{\sigma_M} \tag{9}$$

Where, μ_M is the mean value and standard deviation of the safety margin defined by Equations 10 and 11 [35].

$$\mu_M = R_M - S_M \tag{10}$$

$$\sigma_M = \sqrt{\sigma_R^2 + \sigma_S^2} \tag{11}$$

In both second moment methods and exact methods, the direct use of random variable parameters enables incorporation of design specific distributions and prevents factors from falling out of calibration. Further, the calculated reliability measures support explicit quantification for improved decision making. Second order methods are codified in Eurocode EN 1990 through the provision of target β values. In this thesis, second order methods will not be used directly but rather used for benchmarking via the EU codified target values [3].

Another more "exact" method is the use of Monte Carlo simulation which incorporates probability distributions for the set of random variables, X that influence the limit state equation under consideration. When defining the probability distributions the same uncertainties found by expert Delphi [33] are commonly used in conjunction with any project specific random variables defined through testing. Each distribution is sampled a large number of times, N, to instantiate the random variables X as $\hat{x_j}, j = 1, 2, ...N$. Taken together, the vector x "are realizations of the so-called basic random variables X representing all the relevant uncertainties influencing the probability of failure" [35]. For each x_j a virtual experiment is conducted and analyzed through the limit state equation with a failure event F given by a functional relationship based on the limit state as shown in Equation 12 [29].

$$F = \{g(x) \leq 0\} \tag{12}$$

Using the failure definition, the probability of failure may be calculated exactly through equation 13

$$P_f = \int_{g(x)\leq 0} f_x(x)dx \tag{13}$$

Where $f_x(x)$ is the joint probability distribution of X, the set of random variables [35].

Due to the challenges of solving Equation 13 in closed form, Monte Carlo simulation methods are commonly used to provide an estimate of P_f. The method commonly employed in the literature and adopted in this thesis is based on incorporation of an indicator function $I[g(x) \leq 0]$ which is set to equal 1 if $g(x) \leq 0$ and 0 if $g(x) > 0$. The indicator is used to enable integration over all $g(x)$ by:

$$P_f = \int_{g(x)\leq 0} f_x(x)dx = \int I[g(x) \leq 0] f_X(x)dx \tag{14}$$

Further, simulation of N realizations of the random variables composing X provides a statistical estimate for P_f given by Equation 15

$$P_f = \frac{1}{N} \sum I[g(x) \leq 0] \tag{15}$$

Combination of Equations 12 and 15 shows the P_f estimated through Monte Carlo simulation is literally the percent of failures from a large number of experiments which incorporate all of the basic random variables as shown in Equation 16 [35].

$$P_f = \frac{n_f}{N} \tag{16}$$

Monte Carlo is considered an "exact" method because neither parameter distributions nor limit state functions are simplified. They are however not exact because of uncertainty in the parameter distributions, limit state functions, and model form. These sources of uncertainty will be identified throughout the thesis and are generally categorized as random uncertainty intrinsic to the problem domain referred to as aleatory uncertainty or systemic uncertainty of measurements or models referred to as epistemic uncertainty [21].

To address the objective of this thesis, PV structural systems designed according to code for a 90 mph wind zone, will be evaluated through Monte Carlo simulation to provide a quantitative measure of structural performance. By incrementally expanding the scope of the Monte Carlo simulation, two sequential performance measures will be produced to characterize PV system reliability. First a wind speed array will be combined with the set of random variables that influence wind loads along with the random variables that influence strength. Together, this provides a probabilistic model for assessing the structural state of failure or non failure (survival) in response to a given wind speed. The results of this analysis will be synthesized as a set of fragility curves. Second, the Monte Carlo scope will be expanded by modeling the extreme annual wind speed as a random variable to assess reliability over time with

P_f and β based on historical wind speeds distributions. The fragility model and the reliability model both provide measures useful for quantifying structural performance. However a critical difference exists that will be explored in greater depth through the thesis, the fragility model provides a probability of failure conditioned on a wind speed while reliability model treats wind speed as a random variable and is dependent on time.

At the core of the Monte Carlo method is the use of statistical distributions for random variables. Evidence reported in the literature review suggests that the statistical distribution used to develop pressure coefficients for building roofs is erroneously utilized in the design of building applied PV systems. Consequently, wind tunnel testing for the development of refined pressure coefficient statistics has been included in this thesis to reduce model error and to illustrate how the simplified code method fails to provide uniform performance across actual systems types when engineered according to current code application guidance. In contrast, steel design and structural component design are well established fields with proven methods for translating member loads into member sections and properties [7]. Furthermore, once the loads are established, there is little novelty in a PV structural system compared to structural systems with similar scale members as seen in light weight roof and wall frames and warehouse storage racking. Because the wind load determination is the primary source of risk, this thesis is focused primarily on these loads and will use a simple example failure mode for resistance so that a complete limit state may be analyzed.

Based on the thesis goals and assumptions, the following tasks are structured to systematically evaluate the performance of systems engineered with the simplified code method through a baseline Monte Carlo simulations that is first refined to eliminate error, than expanded to incorporate an extreme wind speed model.

1.3.1 Development of a general probabilistic model for assessing structural response

The proposed risk measure will be based on fragility analysis to establish a methodology for performance based engineering risk assessment of code designed residential PV systems. The code designed systems for evaluation will follow the American Society of Structural Engineering (ASCE) method for wind load determination and the American Iron and Steel Institute (AISI) method for structural member sizing. Fragility analysis of a code designed system entails a conditional assessment of structural response to a set of wind speeds that result in wind loads. The outcome of fragility analysis is a set of explicit probability of failure statements for a residential PV system engineered according to the structural building code and prescribed wind speed map. The probability of failure quantifies the likelihood of failure, when exposed to a specific wind speed from the set of wind speeds. The wind speed set includes the design wind speed (e.g. 90 MPH) along with lower and higher wind speeds to provide a near zero and near certain chance of failure.

The methodology will utilize Monte Carlo methods to incorporate uncertainty found in the wind load structural demand and the PV system's structural supply. While the focus of this thesis is on the structural demand incorporation of a simple structural supply, an example is required to assess the effect of uncertain structural demand on reliability. Therefore, each Monte Carlo sample will combine the supply and demand associated with a simple limit state example to determine a sample outcome of either survival or failure. A large set of samples are then aggregated for each wind speed to develop a probability of failure or its inverse, the probability of survival.

The conditional probability of failure developed in this task is most useful in cases when a decision maker benefits from maintaining separate structural and climate models. This is common, when a project developer has conducted technical due

diligence on a site and developed a more accurate wind model than available in the code. Alternatively custom wind models may be developed to account for uncertain global warming effects [64].

1.3.2 Wind tunnel testing to address existing model error in pressure coefficients

As discussed the Monte Carlo method requires statistical models for uncertain parameters. Most of the nominal values and the expert derived uncertainty statistics accepted for use in reliability analysis of ASCE and AISI are also accepted for analysis of residential roof mounted PV systems. However, the ASCE wind pressure coefficients are reported to be erroneous when modeling wind loads on roof mounted PV systems [17]. Wind tunnel testing has been conducted to reduce error by updating the wind pressure coefficients for residential rooftop mounted PV systems. The wind tunnel experiment was designed to address the relevant set of parameters identified through a literature review of prior PV system wind tunnel studies and by following the ASCE wind tunnel test requirements.

1.3.3 Development of a general reliability model

The fragility model developed in Task 1 provides a conditional probability of failure useful for decision makers who maintain independent structural and climate models. For some decision makers, combination of these models into a general reliability risk measure is preferable because it provides a single measure of reliability.

In this task, a reliability risk measure is developed to characterize the likelihood of failure. This is accomplished by coupling the fragility model with the wind hazard model in a single Monte Carlo simulation environment. Epistemic uncertainty in the wind load model will be quantified and reported. The reliability risk measure will be used to compare the reliability of alternative system types engineered to code, and also used to benchmark against system types and also against codified target values.

1.4 Organization

Chapter 2 will introduce typical residential PV system structural configurations. Chapter 2 will then review the prevalent aerodynamic effects that govern wind loads on the configurations under consideration. A review of reported and potential losses from PV system failure under wind loads will be presented. Finally, engineering design methods used for residential PV system structures are presented and demonstrated in a case study of the system types.

Chapter 3 will present established methodology for fragility analysis. Aleatoric and epistemic sources of uncertainty in PV system reliability analysis will be identified from the literature. A general fragility model for PV system structural failure will be developed. Finally Chapter 3 will demonstrate the fragility model on the three system types under consideration using a single limit state example, that is representative of typical structural failure modes.

Chapter 4 will present the experimental effort to reduce model error in the wind pressure coefficients applied to residential roof mounted PV systems. A comprehensive literature review will be presented on the current state-of-the-art approaches and understanding of experimentally determined PV system wind pressure coefficients. Next, the wind tunnel experimental approach will be described and related to the literature review and ASCE code requirements. Finally, the measured wind load statistics will be reported and used to update Chapter 3 fragility models.

Chapter 5 will present the development of a reliability based assessment of residential PV system structural response to wind effects by incorporating probabilistic wind models. The reliability model will be demonstrated via case study on each system type with the consistent limit state example. The results will be used to assess whether code engineered systems have a consistent reliability across system types and meet existing codified reliability targets.

Chapter 6 will summarizes the main points, reviews key findings and conclusions.

Chapter 6 also identifies areas of investigation for future works.

CHAPTER II

WIND LOADS DETERMINATION

Despite the significant material and labor devoted to a residential PV systems structural response to wind loads, relatively little scientific attention has been given to the determination of wind loads on residential PV systems [17]. This Chapter will present common residential PV system structural types, examine relevant aerodynamics effects on residential PV systems and wind related losses. Finally, a case study will review and demonstrate current design practices on ten design cases applied to three roof configurations.

2.1 Balance of system types

Among the current commercially available PV systems, silicon solar modules applied over the residential roof surface dominate the market with over 90% market share [9]. Thin film technologies, including CIGS, CdTe and amorphous Silicon make up the rest of the residential market, most of which are also applied in modules over the roof top with a small percentage applied as building integrated Photovoltaic (BIPV) roof shingles or integrated panels replacing roof components. Within the silicon solar module market, equipment providers have responded to unique costumer requirements by developing divergent racking system types and have gained significant market share. In comparison to the residential market at the time of the Solar ABC's structural guidance publication, the market has experienced significant diversification in structural racking systems. Currently, there is risk that our ad-hoc approaches do not provide for measured or uniform risk.

Racking system types are categorized in this thesis according to the number of dimensions in which a structural member spans. Current types include 0-Dimensional

(a) 0D Racking System
(Zepsolar, 2013)

(b) 1D Racking System
(Landpower Solar Technology Co., 2013)

(c) 2D Racking System
(Energy Solutions, n.d.)

Figure 6: The 0-D, 1-D, and 2-D Racking System types

(0-D), 1-Dimensional (1-D), and 2-Dimensional (2-D) configurations. Figure 6 shows examples of a 0-D system with isolated connection, a 1-D system with linear rail member spanning multiple modules, and a 2-D PV racking system with members spanning in both directions. Theoretically, a 3-D system might incorporate compression and tension members in the Z plane but this has not yet been introduced to the market. The number of spanning dimensions is treated as a governing characteristic because the structural spanning member is the primary mode used for aggregating modules in a shared structural system. The length and area of module surface supported by a single structural member impacts the area averaged peak wind load experienced by the member [11].

Common to each racking systems type are modules mounted parallel to the roof top with a gap of 2-6" between the roof surface and module back. Modules are configured on the roof with unique layouts defined by solar access, fire code set backs, wind zones, and power capacity requirements. All configurations utilize a gap between adjacent module edges to accommodate thermal expansion and attachment hardware; typical gaps range from 1/8 to 1/2". Configuration parameters are believed to impact the aerodynamic effects that create wind loads on the array [17] [60] [71].

More holistically, the structural system impacts a broad set of cost including material costs, roof penetration hardware and flashing, labor requirements and even module reliability. Due to these broad implications, it is not suggested that one system type should be preferred over the other based on the wind loads, but rather that tools for evaluating performance must accommodate differences in structural system types. Recently, the introduction of a safety standard specific to mounting systems and devices for PV modules has reinforced the importance of wind loads and, designated a static load test designed to simulate wind loads. Additionally, the standard specifies a snow design load and test procedure as well as electrical bonding test procedure [1].

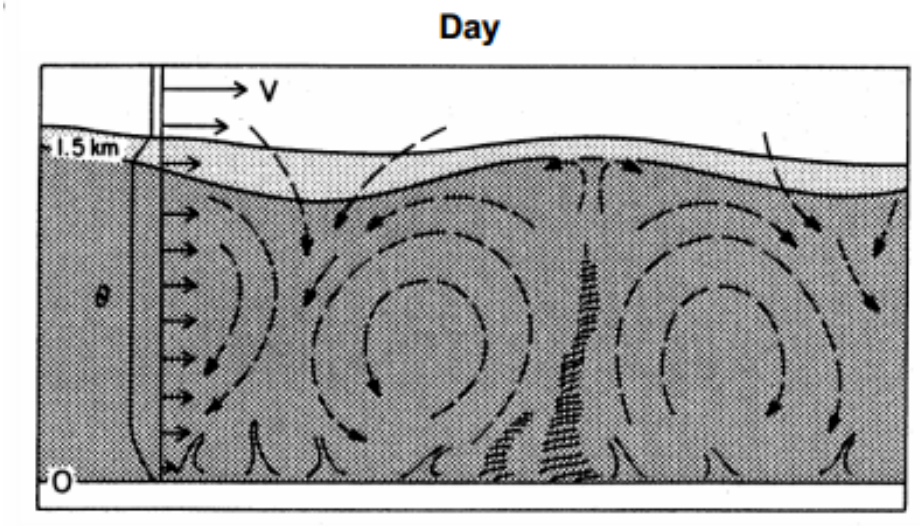

Figure 7: Schematic of daytime atmospheric boundary layer[48]

2.2 Aerodynamic Behavior

The proliferation of system types, in conjunction with the adoption of prescriptive safety standards formulated on limited scientific understanding of the actual wind loads, motivates investigation of wind loads and development of performance measures to quantify the corresponding risk.

When applied to residential rooftops, solar PV systems experience wind loads governed by multiple aerodynamic flow phenomena. An introduction to relevant terms and phenomena will be provided. Early work to characterize wind and wind effects on structures was conducted by the American Society of Civil Engineers. Wind can be simply described as air with a non-zero velocity relative to a frame of reference. The velocity field may be along a single axis or circulate with a spectrum of eddy lengths in multiple axis as depicted in Figure 7. From the frame or reference of a building, the velocity field of wind may include components along the building length, transverse to the building, and orthogonal to the building plan [43] [11].

Uniform wind, also referred to as free stream flow, typically only occurs in the absence of flow obstructions or a boundary layer. In the presence of a stationary surface

such as the ground plane a boundary layer forms with zero velocity at the boundary. Farther away from a boundary is a transition zone, known as the atmospheric boundary layer (ABL) which exists up until wind flow is no longer effected by the boundary and free stream flow conditions exist. Within the ABL large scale eddies form that break up into small eddies and eventually convert to heat or aggregate back into longer wave lengths.

Obstructions such as trees, buildings and solar PV systems alter flow conditions by forcing a change in the velocity field's speed and direction. Bernoulli's theorem establishes a relationship between free stream flow and flow around an obstruction by relating the dynamic pressure, q_o (Equation 17) and static pressure, p_o with the dynamic pressure q and static pressure p at any point on an object as shown in Equation 18.

$$q = 1/2\rho(V)^2 \tag{17}$$

and

$$1/2\rho(V_o)^2 + p_o = 1/2\rho(V)^2 + p \tag{18}$$

A relevant phenomena occurs when the local velocity around an obstruction becomes greater than the free stream and a negative pressure is developed contributing to a normal force vector away from the surface. Alternatively, the local velocity may decrease and pressure increase resulting in an increased local pressure and normal force vector towards the surface. When an obstruction such as a solar module has both top surface and bottom surface, both surfaces see a local pressure and the corresponding net force vector is the resultant of top and bottom vectors. For the purpose of predicting structural responses, it is convenient to resolve the net force into a component parallel to wind at the roof surface, drag, and normal to wind at the roof surface, lift as described in Equations 19 and 20.

$$Drag_(forceparalleltowind) = C_D qA \tag{19}$$

$$Lift_(forcenormaltowind) = C_L qA \tag{20}$$

Where A is the surface area and C_D and C_L are experimentally determined wind pressure coefficients for drag and lift with sign convention shown in Figure 8.

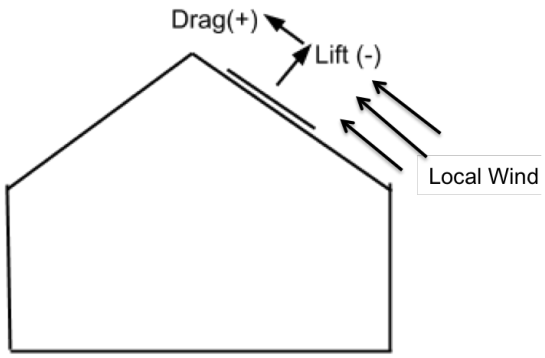

Figure 8: Sign convention for aerodynamic lift applied to residential solar PV systems

Early wind tunnel work to determine wind pressure coefficients was conducted on flat plates. Figure 9 illustrates that drag was observed to monotonically increase between angles of 0° and 90° while lift was observed to increase up to a maximum lift coefficient of 0.7 to 0.9 occurring between 35° and 50°. At 0°, parallel to the free stream, lift coefficients of 0 to 0.25 were measured [43].

Generally, the trends from flat plate research apply to buildings, a low pitch roof top experiences less drag and more lift than a steep pitch roof top [11]. However, PV systems on building roof tops experience a combination of flow separation effects and Bernoulli effect lift and drag. Furthermore, wind that approaches a building corner is subject to being turned along the building face then flows over the roof edge in a vortex [16]. State of the art emperical models lack the capability to predict behavior associated with the complex flow behaviors around a building with adequate accuracy for engineering design [39]. Current practices rely on experimentally derived

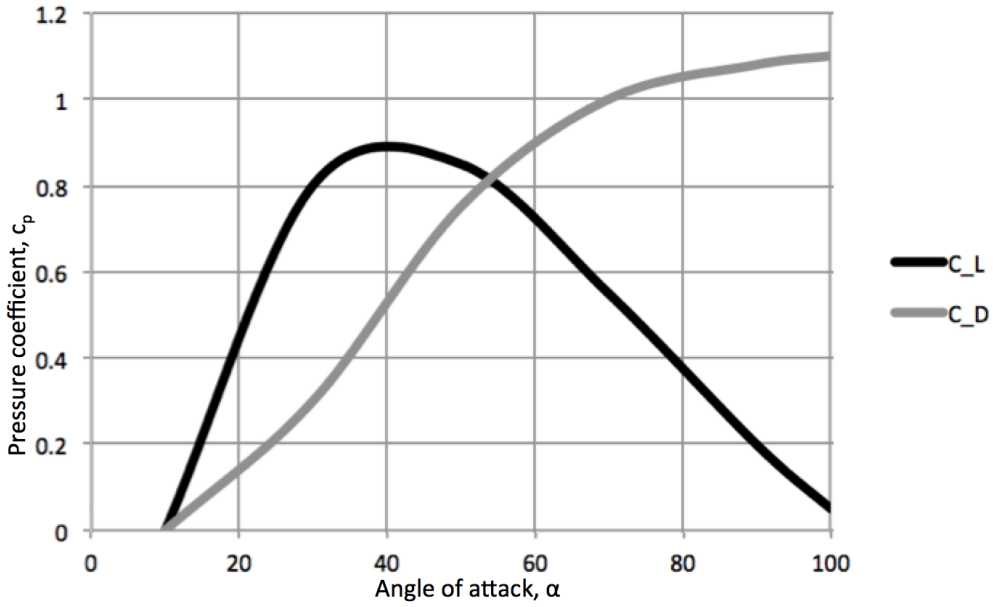

Figure 9: Experimentally derived pressure coefficients for flat plates with aspect ratio $\gamma = 1$ adapted from Hoerner [43]

analytical models to predict aerodynamic effects on building structures and attached systems.

2.3 Residential PV system wind caused failure modes and effects

Despite the challenges in characterizing aerodynamic phenomena, the effects are often but not always readily apparent. Wind is known to be a contributing cause to module failure modes including broken interconnects, solder bond failure, broken glass, mechanical connection failures, and module frame structural failure [54] [74]. As shown in Table 2 failure modes may be caused by multiple interacting causes. Moreover, multiple failure modes share common effects making failure forensics a challenging and growing field. For example causes of solder bond failure include wind deflection, thermal cycling, vibration during shipping, poor manufacturing quality, and poor module design. The effects of module failure can include, power loss, ground fault, electrocution and fire.

Table 2: Failure Mode Effects Analysis for Structural failure

Failure Mode	Structural Failure
Failure Cause	Wind Load, Snow Load, Installation quality, Design
Failure Effect	Module Breakage, Frame deformation, Module liberation
Failure Mechanism	Mechanical Fatigue, structural stress

Limited cases of residential PV system structural failures caused by wind have been reported in the literature or through the National Renewable Energy Laboratories PV reliability program. Specifically, no failures were reported in the literature from residential PV system installations in New York, New Jersey and Louisiana after Hurricane Katrina and Hurricane Sandy. It is possible that the critical wind speed did not occur at any specific residential PV systems or that critical wind speeds approached the system from a direction that did not cause peak structural effects. Over time, as the total installed fleet of residential PV systems grows and accumulates more wind exposure, failures should be expected to occur at a rate consistent with predictive reliability models if the sources of uncertainty are characterized and accounted for.

In the event of a wind caused structural failure the nature and severity of the effects will be influenced by the configuration and size of system components. Figure 1 (See Chapter 1) illustrates a typical residential PV system with 1-D structural rails attached to a residential roof composed of rafters, decking and water proofing layer. A L-foot is attached to the rafters with lag bolt and provides a pin connection to support a rail, which is the primary structural member. Flashing around the L-foot prevents water intrusion at the penetration. The rail is visible on the left side of the roof with no modules attached and in section. Modules mounted parallel to the roof are attached to the rail with a module clamp that transfers wind pressure to the rail as a point load. Modules are certified with a test load of 45 pounds per square foot (PSF) [4]. Under wind pressure, multiple failure effects are possible including plastic rail deflection. Depending on the direction of wind pressure a rail experiencing a plastic

hinge will either deflect away from the roof or into the roof. In either case a change in the gap between modules will occur and change the aerodynamic performance of the system in an unpredictable manner due to the limitations in the current body of knowledge. Furthermore, a plastic hinge may also change the modules angle of attack with respect to the wind and also result in an unpredictable change in wind loads. With the propensity for a sudden change in wind loads it is possible that loads will exceed the design loads for other system components, such as lag bolts, and the system will experience progressive collapse. In an alternative scenario, a rail with plastic hinge may damage the attached module and be electrified. If a rail is electrified and equipment grounding is operational, a ground fault should ensue and result in a system shut down. Alternatively, if the grounding is not operational due to improper installation or other failure, the rail may remain electrified at high voltage and present an electrocution risk to service personal. To summarize, if a PV mounting rail experiences a plastic hinge, multiple scenarios are possible ranging from no additional damage to catastrophic structural failure or even risk of electrocution. Other wind related structural failures may occur in the module clamps, lag screws, rail attachment bolt (T-bolt) pull out or even failure of the module frame or laminate. Non structural failure modes may also occur due to wind, these include electrical wire movement and chafing that results in an electrical fault, deflection of roof penetrations that results in water intrusion. Due to the focus on uncertainty in wind loads, this thesis will use rail plastic hinge formation as an example failure mode to demonstrate the proposed risk assessment methodology in the following case studies.

2.4 Engineering Design Methods and Case Studies

The PV system structural design process consists of wind load determination, stress analysis, then member and connection strength check. The methodology for each step will be presented and demonstrated in a case study on multiple configurations

of each system types under consideration.

2.4.1 Wind load determination

In the design of PV racking systems, load combinations with wind as the principal action govern member sizing unless designing for high earthquake prone or high snow regions. A consequence of wind loads governing is that the wind loads used in design significantly affect hardware and labor cost [18]. Currently, an engineer is required by code to use American Society of Civil Engineers (ASCE) Chapter 7 2005 or 2010 dealing with residential roof wind load calculations to determine the structural loads for the design of racking systems that maintain a gap between modules and the roof plane. Wind loads are determined through calculation of a dynamic pressure q, identification of pressure coefficients C_P followed by analysis of applied pressure P [11] [18].

Dynamic pressure The first step in determining wind loads is estimation of the dynamic pressure, q, through the emperical Equation 21.

$$q = 0.00256 k_z k_{zt} k_d V^2 I \tag{21}$$

where

k_z = Exposure dynamic pressure accounts for acceleration due to height and terrain roughness

k_{zt} = Topographic factor accounts for topographic acceleration

k_d = Directionality factor accounts for the likelihood of peak structural action occurring from the same direction as peak wind speeds

V = Basic wind speed representing the 50 year mean recurrence interval (MRI) 3-second gust 33ft above ground with exposure C topography [11].

I = Importance factor to calibrate velocity for building classification.

This approach for evaluating dynamic pressure combines risk management factor, I, with physics based factors k_z, k_{zt}, k_d and V. The importance factor, is established based on human life and property hazard commensurate with a the ASCE building classification. An importance factor, I of 0.87 may be used to calibrate velocity for a 25 year mean recurrence interval (MRI) for structures with low hazard while, $I = 1.15$ calibrates velocity to a 100 yr MRI for high hazard structures [11]. A consequence of this risk management structure is that when the physics based factors in the dynamic pressure calculation are inconsistent with the actual scenario of use, the structural risk of the as-built system is also inconsistent with code intentions for risk management [49]. In recognition of this opportunity for error, ASCE provides a path to update physical parameters. For example, the directionality factor, k_d, may be updated through analysis of local wind patterns and the gust effect pressure coefficient, generally referred to as pressure coefficient, GC_p may be updated through wind tunnel testing.

Design Pressure

Once a dynamic pressure is determined, member specific design pressures may be calculated using equation 22 and one of the alternative ASCE methods to evaluate GC_p and GC_{pi} where, GC_p is the pressure coefficient applied to the external surface oriented away from the building in the negative lift direction and GC_{pi} is the pressure coefficient applied to the internal surface oriented towards the building in the positive lift direction. For a PV module applied above a residential roof, the concept of external and internal are loosely applied since both surfaces are external of the building in which case the orientation governs.

$$p = qGC_p - qGC_{pi} \tag{22}$$

The main wind force resisting system (MWFRS) method is intended for the design of structural systems experiencing wind pressure loading from a large surface area

and the components and cladding (C&C) method is used for the design of structural members which are in direct contact with the applied wind load and have a small surface area in contact with the wind. Components or cladding structural elements "transfer" the applied loading to the the MWFRS [11]. ASCE application guidance, published by the Solar American Board for Codes and Standards advises use of the MWFRS method for Low Rise Buildings for the design of PV racking systems and advises the use of C&C for Low Rise Buildings for module mounting hardware [17]. The MWFRS method for low rise buildings provides a zoning figure and corresponding table of pressure coefficients shown in Figure 11 that provides load cases to account for orientation relative to the wind, leading edge or trailing edge, and proximity to the eaves. The MWFRS method simplifies the physics and assumes a discrete change in GC_p occurs across an infinitely thin boundary between the interior and edge. The components and cladding method takes a similar approach but zoning accounts for proximity to the roof eaves, edge, and ridge. Also, each zone's pressure coefficient accounts for the area "supported by a single structural member [55]" this area is referred to as the tributary area [11]. In the case of a PV module with a structural rail along (or offset from) each edge (Figure 10), half the area between each rail constitutes the tributary area. In contrast, the full area between rails may affect the rail's structural load, it is refereed to as the influence area and is used later in this chapter. Figure 10 illustrates the difference in tributary area and influence area for a 1-D structural system with interior rails BH and CD adjacent to an empty column defined by BCIH.

ASCE prescribes GC_{pi} values for use with both MWFRS and C&C methods. Table 3 shows the prescribed value is dependent on the degree to which the structure is open to airflow, an indicator of the likelihood for pressurization.

Typical obstructions to airflow under a PV array include, structural members, roof flashing, wires, wire management devices and in some locations pest management

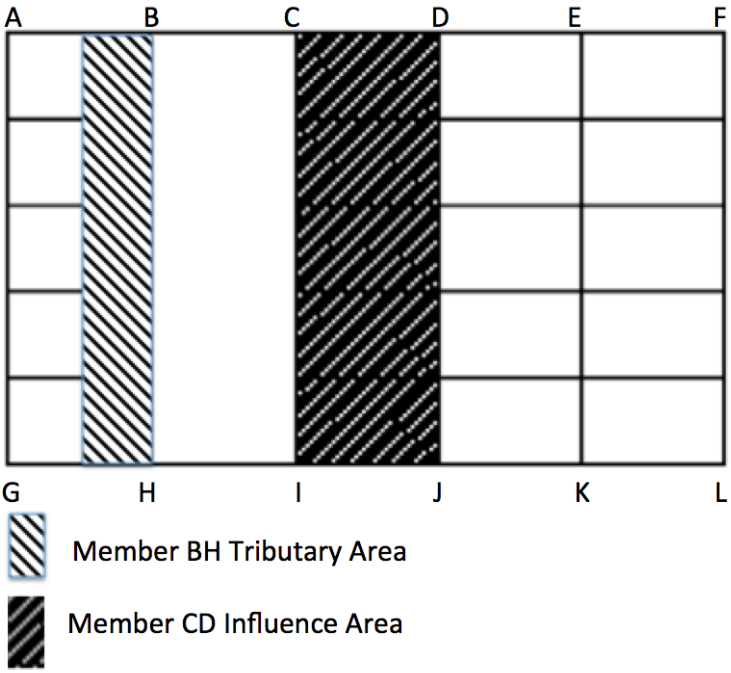

Figure 10: Diagram of tributary area and influence area for interior edge rails

Table 3: Table of ASCE 2005 GC_{pi} values

Open	Partially Open	Closed
+/-0.18	+/-0.55	0.0

devices. Classification of this cavity as open, partially open, or closed has received attention by industry experts as summarized by O'brien.

> "Based on discussions with experts in the field of wind tunnel testing and the ASCE Standard, [the authors of the Solar ABC's guidance publication] believe that a value of +/- 0.1 to +/-0.3 is a reasonable choice for systems with limited restrictions to airflow below the module [17]".

2.4.2 Case Study: Wind load determination

A case study of the three residential PV systems types is presented to demonstrate the wind load determination approach and to generate results for discussion. For the purpose of the case study, a two story residential home in Atlanta Georgia will

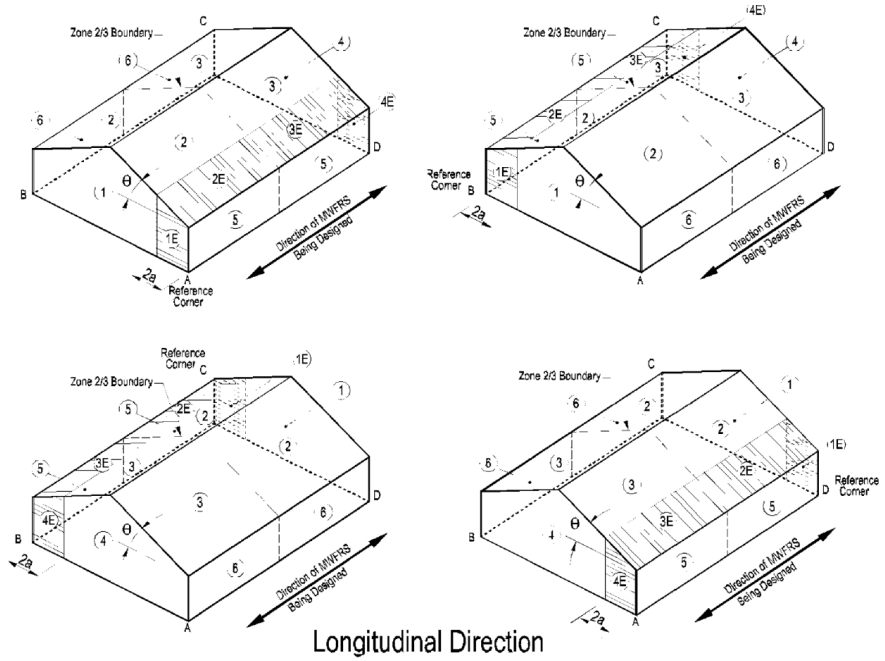

Roof Angle θ (degrees)	Building Surface									
	1	2	3	4	5	6	1E	2E	3E	4E
0-5	0.40	-0.69	-0.37	-0.29	-0.45	-0.45	0.61	-1.07	-0.53	-0.43
20	0.53	-0.69	-0.48	-0.43	-0.45	-0.45	0.80	-1.07	-0.69	-0.64
30-45	0.56	0.21	-0.43	-0.37	-0.45	-0.45	0.69	0.27	-0.53	-0.48
90	0.56	0.56	-0.37	-0.37	-0.45	-0.45	0.69	0.69	-0.48	-0.48

Figure 11: ASCE 7-05 Fig 6-10 MWFRS External Pressure Coefficients

be assumed with limited topographic variation in the vicinity. Each system type is superimposed onto a standard array of 20 modules. As shown in Figure 14 the 0-D system results in 20 discrete structural influence areas, the 1-D system results in 4 discrete structural influence areas, and the 2-D system results in 5 possible structural influence areas. From all possible 2-D influence areas, only the 3 influence areas composed of full columns are selected for the case study. As will be shown, a design case is not only defined by the influence area but also by the placement on the roof, relative to the zoning. Each influence area is assigned two locations, one in which the roof edge is along the right side of the array and the other in which the roof edge is along the left side of the array. In Figure 14 the possible influence area design cases are represented by 18-1 through 18-20 when the roof edge is along the right side and

18-21 through 18-40 when the roof edge is along the left side. From the 68 possible design cases, 10 design cases shown in Table 4 are selected for analysis by eliminating cases with redundant tributary area and zoning combinations.

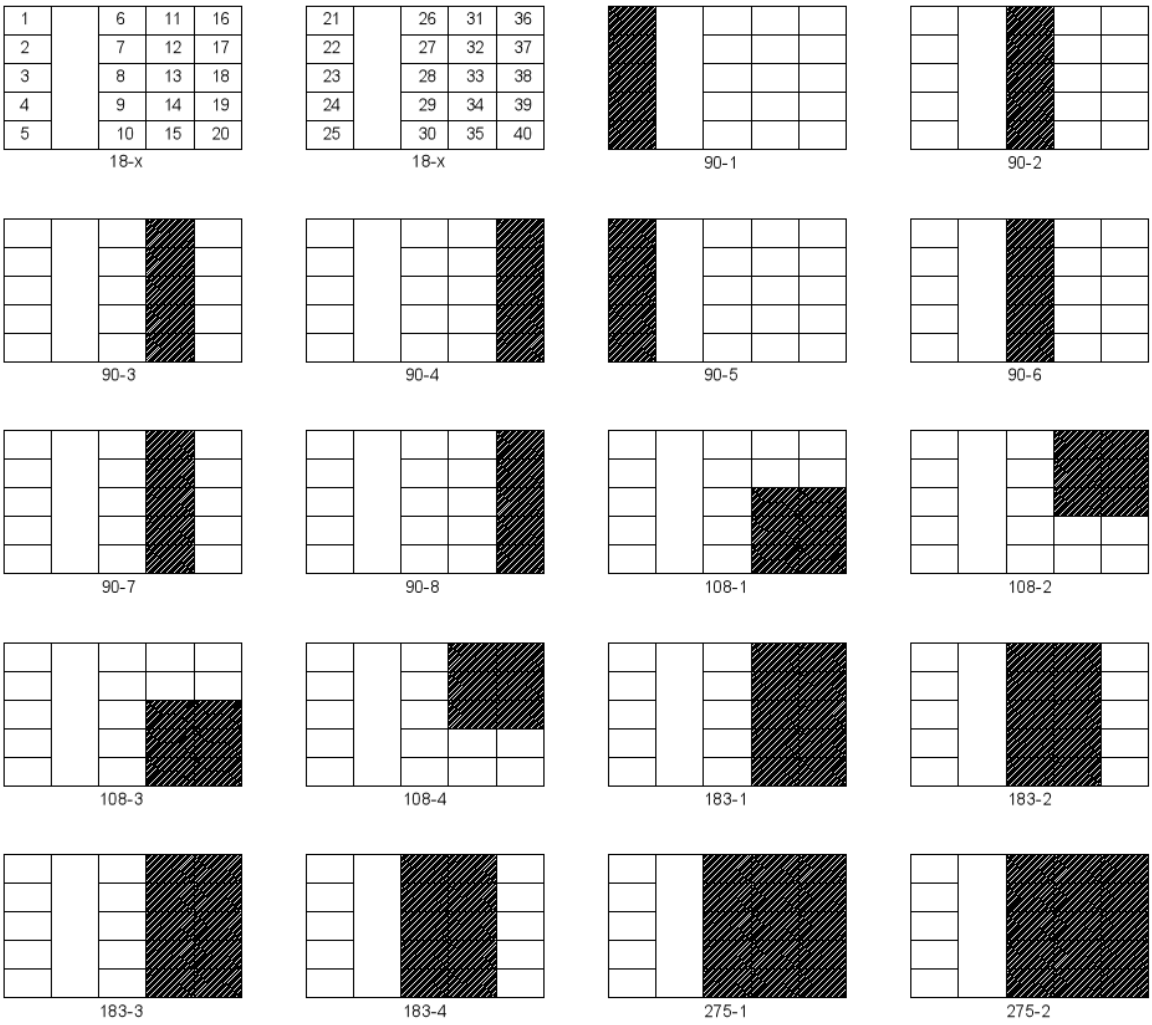

Figure 12: Influence Areas for OD, 1D, and 2D PV systems configurations

To proceed with the case study, the dynamic pressure is calculated through determination of the following parameters for use in equation 21, resulting in $q = 10.9psf$

$\mathbf{h}$ = 20 ft

k_z = 0.7 for exposure B

k_{zt} = 1.0 for flat suburban terrain

Table 4: Design case parameters

System Type	Influence Area	Roof Location	Design Case #
0-D	18.3	top corner	18-101
0-D	18.3	edge	18-102
0-D	18.3	top interior	18-103
0-D	18.3	interior	18-104
1-D	90	Edge	90-101
1-D	90	Interior	90-102
2-D	180	Edge	180-101
2-D	180	Interior	180-102
2-D	270	edge	270-101
2-D	270	Interior	270-102

k_d = 0.85 is a nominal value accounting for the likelihood of peak wind pressure occurring from the same direction as peak structural in asymmetrical structures

V = 90 mph for central U.S. including Atlanta GA.

I = 1.0 for residential areas

Zoning according to ASCE Figure 6-10 (Figure 11) is the next step in defining the wind pressures for each design case [11]. Sample zoning diagrams are illustrated in Figure 13. Four load combinations are considered to determine the maximum positive pressure and minimum negative pressure. For structural systems that span multiple zones, an area averaging approach is taken to determine the pressure coefficient. Zone percentages and corresponding GC_p- and GC_p+ valued are reported for roof angles of 15°, 30° and 45° (Table 5). Combination of the pressure coefficients with the 90 mph dynamic pressure from Equation 21 and a nominal internal pressure coefficient of 0.18 into Equation 22 yields design pressures for each design case shown in Table 6.

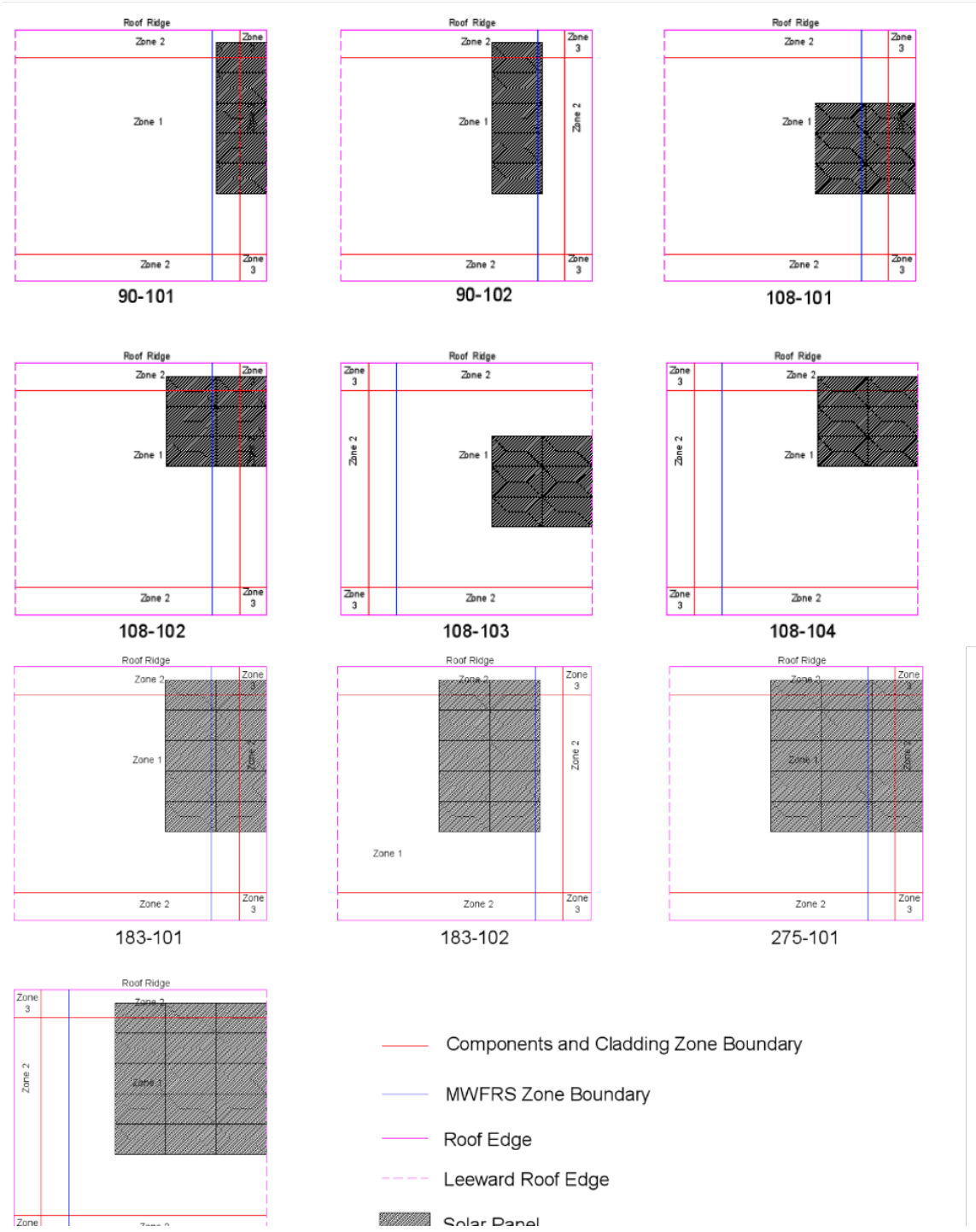

Figure 13: Sample zoning of 1D, and 2D systems

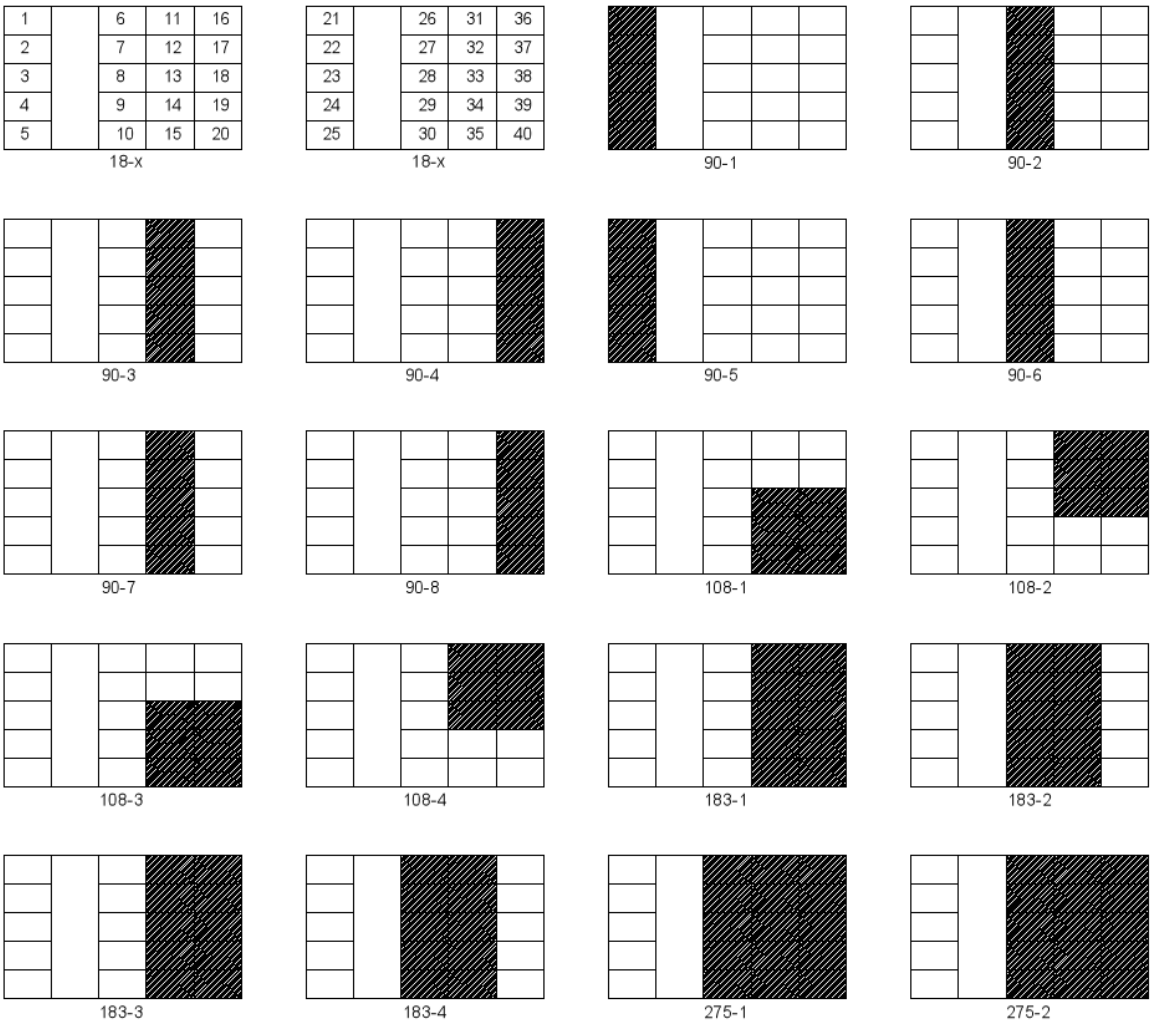

Figure 14: Influence Areas for OD, 1D,m and 2D PV systems configurations

Table 5: Calculated design case GCp values

Design Case	**Zone 2/3 (%)**	**Zone 2E/3E (%)**	**GC_p+ 15°**	**GC_p- 15°**	**GC_p+ 30°**	**GC_p- 30°**	**GC_p+ 45°**	**GC_p- 45°**
18-101	0	100	-0.64	-1.07	0.27	-0.53	0.27	-0.53
18-102	0	100	-0.64	-1.07	0.27	-0.53	0.27	-0.53
18-103	100	0	-0.44	-0.69	0.21	-0.43	0.21	-0.43
18-104	100	0	-0.44	-0.69	0.21	-0.43	0.21	-0.43
90-101	0	100	-0.64	-1.07	0.27	-0.53	0.27	-0.53
90-102	100	0	-0.44	-0.69	0.21	-0.43	0.21	-0.43
180-101	50	50	-0.54	-0.88	0.24	-0.48	0.24	-0.48
180-102	100	0	-0.44	-0.69	0.21	-0.43	0.21	-0.43
270-101	66	33	-0.51	-0.82	0.23	-0.46	0.23	-0.46
270-102	100	0	-0.44	-0.69	0.21	-0.43	0.21	-0.43

Table 6: Calculated design case design pressures

Design Case	P+ 15°	P- 15°	P+ 30°	P- 30°	P+ 45°	P- 45°
18-101	-10.36	-15.67	5.80	-9.01	5.80	-9.01
18-102	-10.36	-15.67	5.80	-9.01	5.80	-9.01
18-103	-7.90	-10.98	5.06	-7.77	5.06	-7.77
18-104	-7.90	-10.98	5.06	-7.77	5.06	-7.77
90-101	-10.36	-15.67	5.80	-9.01	5.80	-9.01
90-102	-7.90	-10.98	5.06	-7.77	5.06	-7.77
180-101	-9.13	-13.32	5.43	-8.39	5.43	-8.39
180-102	-7.90	-10.98	5.06	-7.77	5.06	-7.77
270-101	-8.76	-12.58	5.31	-8.14	5.31	-8.14
270-102	-7.90	-10.98	5.06	-7.77	5.06	-7.77

Wind pressure determination conclusions This section discusses relevant observations from the calculated pressure coefficients and corresponding design pressures. For a roof angle of 15° the positive design pressure is negative. Flow separation is principally caused by the building wall area. A positive pressure occurs when flow streamlines impinge on the array surface, yet because of the low 15° roof slope, the streamlines and array do not come into close proximity resulting in a negative pressure for all approach angles. Higher pitch roofs do have a positive pressure because the roof slopes up into the separated flow resulting in an impinged flow and positive pressure.

The tributary area of a design case does not affect the pressure coefficients within a zone. This is an effect of using the MWFRS method and is inconsistent with the C&C method which would apply a tributary area factor to scale the design pressure with tributary area.

Finally, design pressures for the 30° and 45° roofs are the same for each design case. ASCE attempts to balance accuracy with usability resulting in the need to envelope cases that are believed to have similar load effects. However, if a PV system configured in one portion of the roof such as the top half, it may experience significantly different load effects on 30° roof compared to a 45° roof.

CHAPTER III

FRAGILITY ANALYSIS

State of the art practice for residential PV system design utilizes prescriptive methods demonstrated in Chapter 2. Performance based engineering (PBE) methods developed for nuclear power structures, and applied to light frame wood structures, damns and other structures have not been applied to solar structures. Barriers to the application of PBE tools include a large number of complex failure modes, proprietary components with limited published actual performance statistics, and hard to determine wind load statistics. Nevertheless, the shift to PBE is motivated by the perspective that adoption of residential PV systems does not present a new isolated risk but is actually a revenue generating asset that displaces existing risk from current power generation infrastructure. In light of this perspective, a potentially high cost to society may be realized by assuming historically accepted structural risk is accurately and appropriately applied to distributed power generating assets capable of providing a net benefit to society measured in lives lost per trillion kWh. Reliability quantification provides a foundation for decision makers who are designing PV systems, providing financing, allocating public resources towards their development, and setting reliability targets in future code revisions.

A comprehensive reliability assessment for wind loads may be viewed in two parts, fragility analysis and coupling with extreme wind load models. Fragility analysis entails a conditional assessment of structural response to a set of wind loads. The results of a fragility analysis provide a probability of failure for each wind speed in the set of wind speeds. Typically, the set of wind speeds is selected to span from near zero probability to near certain probability of failure. Extreme wind load modeling entails

statistical analysis of a site or regional historic wind speeds. The result is an extreme annual wind speed model and error quantification. Coupling a site specific wind speed model with a fragility model collapses an array of conditional failure probabilities to a single scalar probability of failure or β value.

This chapter will present background on reliability and structural engineering topics common to both steps in reliability assessment. Subsequently, the fragility analysis method will be presented and demonstrated through continuation of the Chapter 2 case study. The methodology for fragility analysis incorporates Monte Carlo analysis to evaluate the probability of failure at a wind speed given uncertainties in the structural resistance, R and load effects, E for a given wind speed. The Monte Carlo method is considered a high fidelity method compared to low fidelity code method because parameter distributions are utilized for uncertain variables in lieu of nominal values and global or partial safety factors. This chapter will also present a brief background on Monte Carlo, along with an investigation of the specific probabilistic distributions applicable to both resistance and load effects required for Monte Carlo analysis.

3.1 Background

To support the development of fragility based risk performance measure for residential PV systems, background on uncertainties in structural engineering, limit state design and performance based engineering will be provided.

3.1.1 Uncertainties in Structural Systems

Chapter 1 provided an introduction to uncertainties in structural systems, definitions to characterize types of uncertainty, and established the importance of treating uncertainty. This section will provide a foundation for specific sources of uncertainty identified and treated through out remaining sections.

Each of the structural engineering methods presented in Table 1 including the

ASCE code and Monte Carlo methods recognize uncertainties do exist throughout design, construction, and use. In a description of the general principals of structural reliability codified in EN1990, specific sources of uncertainty are identified to include:

> natural randomness of actions, material properties and geometric data; statistical uncertainties due to a limited size of available data; uncertainties of the resistance and load effect models due to simplifications of actual conditions; vagueness due to inaccurate definitions of performance requirements; gross errors in design, during execution and use; lack of knowledge concerning behavior of new materials and actions in actual conditions [5]

Natural randomness occurs in wind loads incident on residential solar PV systems. Sources of randomness include variation in the topography, extreme wind speed, and extreme wind direction [33]. Randomness in material properties and geometries occurs in PV modules, PV racking structural members, and fasteners [67]. Statistical uncertainties occur due to limited records of historical extreme load including extreme wind speed and direction [8]. Additional statistical uncertainty stems from limited records of load combinations. Uncertainty of the resistance and load effect models occur due to simplified loading patterns, treatment of dynamic wind loads with quasi static state assumptions and idealized boundary conditions. Vagueness due to inaccurate performance requirements is especially prevalent between subsystems. For example the performance requirements necessary to maintain PV electrical performance such as low deflection and low vibration are treated with simplified prescriptive requirements such as prescribed attachment location. Further, limited wind tunnel studies of residential PV systems suggest that gross errors in design may occur due to application of erroneous wind pressure coefficients in wind load calculations [40]. Errors in execution are also believed to occur due to multiple causes, but most notably due to the challenge of attaching a fastener to structural rafters with no

visible indication of rafter location. Finally, lack of knowledge concerning material behavior and actions in actual conditions is a challenge in the PV industry where rapid advancement of proprietary module components are common. Performance degradation has been reported due to combined operating and contextual variables. For example the combination of low temperature and structural load effects have resulted in un-anticipated PV cell micro-cracking and conductor strain [54].

While each of the sources of uncertainty can not be explicitly accounted for within the scope of this thesis, the general objective relates to them in two ways. First, the importance of explicit treatment of uncertainty should be demonstrated and established. while this may be generally true across structural and building engineering, it is particularly true in the PV industry which is simultaneously characterized by rapidly evolving materials and methods and also dependent on long term performance. Second, the objective to demonstrate application of reliability measures to PV systems will hopefully enable experts throughout the PV supply chain to understand the importance of statistically characterizing the resistance of materials and structures for use in reliability analysis of critical limit states.

3.1.2 Exact Methods for Limit State Design

Chapter 1 provided an introduction to limit states with a focus on simplified linear limit states as the basis for prescriptive safety factor based code methods. This section will review key points and present an expanded view of limit sates for use with Monte Carlo analysis.

A structure's state at any point in time may be described by geometric, material, boundary condition and load variables. Each variable is free to have a value from the subset of all possible values existing in the n-dimensional space $\mathbb{R}^n$ [29]. Each combination of variables constitutes a unique structural state. A subset of states is characterized by loads effects e which exceed the resistance, r, these states compose a

failure set. In the context of a structural requirement, the failure set indicates an unsatisfied requirement. In the simplified linear approximation method the tangent line through the closest point of intersection between limit state surface and probability density function is used to represent the limit state. Alternatively the $\mathbb{R}^n$ dimensional boundary of the limit state characterizes a failure surface where each point on the surface is a structural state at the limit of failure, for this reason the surface is also known as the limit state surface. Further, the limit state surface separates a safe set from the failure set. Mathematically, the limit state surface is defined by "the set of zero points for a piecewise differentiable function $g(x1, ..., xn)$ (Equation 23) which is differentiable everywhere in the domain and takes positive values in the internal of the safe set and negative values in the internal of the failure set" [29].

$$G(X) = 0 \tag{23}$$

Where X is the vector of random variables $(x1, ..., xn)$.

Exact Solutions

Given the random variables E and R are function of X, an exact solution for the probability of failure is given by representation of the resistance as Equation 23 which teaches probability of failure, $P_f = P(E > R)$. An approach to solving Equation 23 requires definition of an event A to represent the effect, e occurring in the internal $< x, x + dx >$ as illustrated in Figure 15. P(A) is then given by

$$P(A) = P(x < E < x + dx) = \varphi_E(x)dx \tag{24}$$

Similarly an event B must be defined as the event that occurs when $R < X$, making the probability of B defined as

$$P(B) = P(R < x) = \Phi_R(x)dx \tag{25}$$

Given P(A) and P(B) and using Equation 13 a differential probability of failure dP_f is given by the joint probability of A and B expressed as

$$dP_f = \Phi_R(x)\varphi_E(x)dx \tag{26}$$

Finally, an exact solution for P_f is given by integrating Equation 26 as follows

$$P_f = \int_{-\infty}^{\infty} \Phi_R(x)\varphi_E(x)dx \tag{27}$$

Integration of Equation 27 is typically conducted numerically using Monte Carlo Methods [51], [5], [29].

Use of Monte Carlo simulation as an exact method for limit state design is one of the established options for meeting explicit design requirements established through performance based design. A benefit of this method is the ability to examine the sensitivity of the outcome to specific variable distributions. This is useful because it provides the designer with an option to pursue reductions in uncertainty or to modify nominal values as needed to meet specified performance targets. The process of setting performance targets will be discussed further in the following section.

3.1.3 Performance Based Design

Traditional engineering practice has focused on ensuring life safety through the application of safety factors, first through ASD and more recently through LRFD. These approaches have been criticized for three limitations (1) failure to provide explicit quantification of a building system's likelihood of achieving the desired goal of life safety and (2) exclusion of other "desirable attributes" including serviceability and (3) lack of documented intent which encumbers development of novel designs [65].

Performance based design addresses the criticism of traditional engineering practice through engagement of stakeholders to define explicit performance measures.

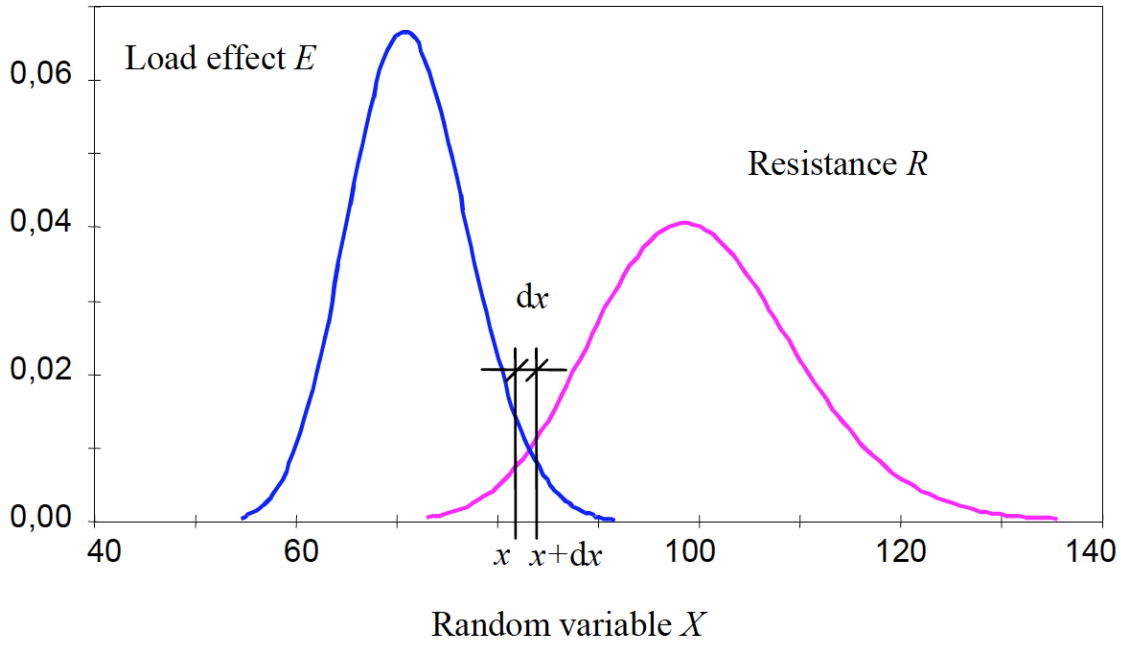

Figure 15: Probability density function of load effect, E and Resistance R illustrating failure region [5]

Commonly, performance measures are defined to communicate the desired performance under a specific hazard severity such as continued use during an annual extreme event. Translation from the qualitative performance statement to an engineering analysis requires definition of a limit state that relates a specific structural action such as formation of plastic hinge to the desired performance. Once a structural action is defined, testing or analysis based on the principals of structural mechanics may be used to relate occurrence of the limit state to a hazard's demand. Given the uncertainty in both demand and structural response, performance based design commonly expresses the probability of a limit state through the conditional likelihood of a structural action given a hazards demand, D reaching state x joint with the probability of $D = x$ as shown in Equation 28

$$P(LS) = \sum P(LS|D = x)P(D = x) \tag{28}$$

The conditional limit state probability represented by $P(LS|D = x)$ is the structural fragility for a given hazard occurrence with severity x.

3.2 Structural Fragility

Fragility models were originally developed to relate probabilistic structural outcomes to a spectrum of possible earthquake load events. A majority of early development focused on nuclear facilities due to the high hazard levels [76]. In the early use of fragility models, structural outcomes have been expressed in terms of both limit states [33] and damage states [26]. While a limit state expresses the notion of a structural demand exceeding the structural capacity for a specific failure mode; a damage state extends this concept to include the physical and/or monetary impact of the failure mode.

Fragility models may be represented with fragility curves or with the lognormal fragility function in Equation 29.

$$F_i(D) = \phi(\frac{ln\frac{D}{\theta_i}}{\beta_i}) \tag{29}$$

Where $F_i(D)$ is the conditional probability of damage state or limit state i as a function of Demand, D; ϕ is the Gaussian cumulative distribution function; θ_i is the the median value of the probability distribution and β_i is the logarithmic standard deviation .

Graphically, the fragility function is represented with the fragility curve in Figure 16 with structural demand on the X axis and failure probability on the Y axis. The fragility curve may be interpreted by the statement "at demand θ there is a 50% probability of failure". Multiple fragility curves may be plotted together to illustrate how a sequence of limit states from, unoccupiable, to loss of immediate use, to structural collapse, becomes increasingly likely as the demand increases.

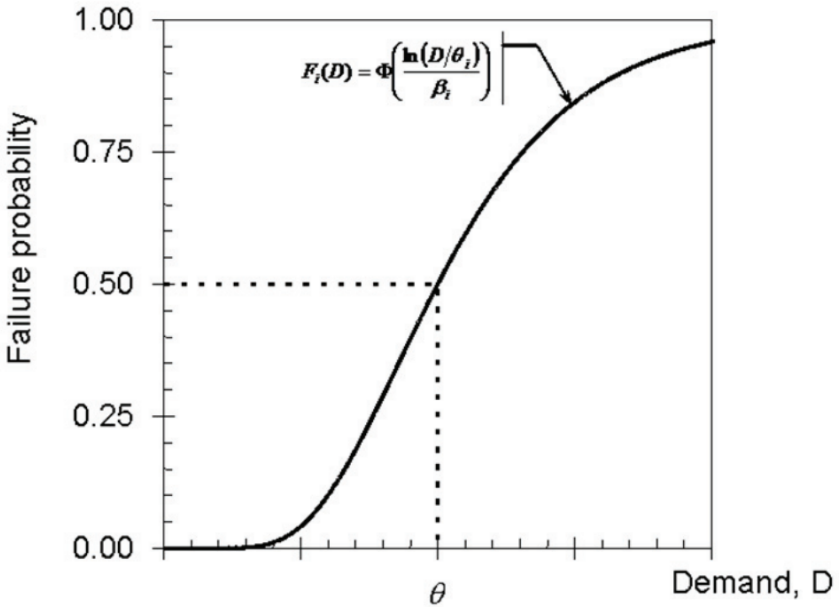

Figure 16: Illustration of lognormal fragility function [26]

3.2.1 Fragility model derivation methodology

Alternative methods for the development of fragility models are recognized by the Federal Emergency Management Agency (FEMA) with the preferred methods including test data or field data documenting system reliability under a range of structural demands. When no field data is available, fragility curves may be derived through analytical models of the behavior expected to occur in response to a range of demands [26].

In order to account for the random variables that affect structural response, fragility model derivation utilizes Monte Carlo simulation "to explore the effect of variation in material strength, construction quality, and other random variables on the resulting capacity" [26]. After sufficient iterations are completed to sample from the full distributions of each random variable, a median value and calculated standard deviation β_r can be determined. American Technology Council (ATC) recommends the model standard deviation β be corrected for epistemic model uncertainty $\beta_u = 0.25$. Determination of the quantity of runs required for "sufficient iterations" is

based on the standard error required for the intended analysis. A discussion of error will be provided in the following section.

Alternatively, a single calculation method allows for the structural capacity Q to be calculated with nominal material properties, dimensions and workmanship and used in Equation 30 to calculate the median capacity, θ and a value of $\beta = 0.4$ is assumed [26]

$$\theta = 0.92Q \tag{30}$$

The single calculation method is based on expert judgment for typical model dispersion and uncertainty. While this is not a preferred method it does offer a viable validation approach when actual failure data or a reliable model with known parameter uncertainty is not available.

3.2.2 Model estimation error

The Monte Carlo method is useful for estimating the distribution for a random variables which itself is a function of multiple random variable. The distribution estimate is based on a sample size n composed of a numerically derived random variables. According to the central limit theorem, the sum of n random variables will be normally distributed. Hammersley and Handscomb state "$n = 10$ is a reasonably large number while $n = 25$ is effectively infinite"[42]. However, as n approaches infinity the mean of the distribution converges faster than the tails. This is particularly relevant for reliability analysis which is predicated on the occurrence of low frequency events. The error with with which a sample distribution estimates a parent distribution is given by Equation 31 where σ_n the standard deviation of the sample quantifies the standard error of the estimation. Accordingly, for a k reduction in error desired, n must be increased by k^2.

$$\sigma_n = \sigma/\sqrt{n} \tag{31}$$

3.2.3 Applications to wind hazards

Fragility practice was extended to treat wind hazards in the 1990's in response to the occurrence of natural disasters and also in response to the adoption of light-frame residential construction [65]. Observed failure rates due to wind hazards were not consistent with the reliability predicted from LRFD. This inconsistency challenged insurance premium underwriters to set premium rates and policy makers to establish hazard management policy. This motivation led to the application of fragility analysis to wind hazards [65]. In the application of fragility analysis to wind hazards (Equation 29), the demand has been treated as both the 3-second wind speed and the wind pressure. Use of the 3-second gust necessitates that the random variables and associated uncertainty necessary to convert from a 3-second gust to a wind pressure must be embedded into the fragility curve. This incorporates the physics required to estimate an applied pressure based on a 3-second gust wind speed. Alternatively, use of a wind pressure eliminates aerodynamics from the fragility analysis, assuming no aero-elastic behavior is present, and focuses on the structural behavior in response to an applied pressure.

As discussed, an analytical approach to fragility analysis, requires a mathematical model for the load and resistance. Wind load models combine a basic wind speed, along with empirically derived site factors to determine the velocity pressure on a structure per Equation 21. For example, an ASCE 7 compliant calculation calls for the selection of an exposure coefficient k_z based on surface roughness and mean height. However, uncertainties in site specific surface characteristics, may lead to an actual exposure coefficient that varies from the calculated model value. Similarly, the actual structural response may vary due to uncertainties in the structural analysis.

Uncertainty, in both the load and resistance, must be accounted for in the application of fragility analysis to wind loads.

3.2.4 Sources of Uncertainty and Error

The accuracy with which a wind load and structural response may be predicted is limited by uncertainties and error in the analysis. Random variation in environmental characteristics such as variability in surface roughness or wind speed that is intrinsic to the problem is characterized as aleatory uncertainty. Uncertainty due to the model structure used to represent measured data and predict future occurrences is characterized as epistemic uncertainty. The mathematical models used in fragility analysis for hazards of all types including wind must account for both aleatory and epistemic sources of uncertainty [21].

The mathematical model (Equation 17) for velocity pressure attempts to account for physical parameters which affect the velocity pressure. The approach embeds statistically derived relationships in a surrogate model in lieu of physics based modeling. As a result of the model form, model form uncertainty is introduced which has been shown to contribute significantly to the total uncertainty [72]. Limited efforts have been reported on the quantification of velocity pressure model form uncertainty. Nevertheless, validation efforts have been completed which suggest that model input uncertainty is the dominant cause of total uncertainty [50], [33]. Model validation should not be interpreted as uncertainty quantification because validation deals with a sample measured in limited experimental conditions where uncertainty quantification measures the capability to predict samples that have not yet been measured [72]. The scope of this thesis is limited to the treatment of model input uncertainty found in wind load statistics and member strength statistics.

Wind Load statistics The ASCE approach to wind load determination incorporates both aleatory and epistemic uncertainty. Aleatory uncertainty stems from

natural variation in the basic wind speed, surface characteristics and wind direction. Epistemic uncertainty in wind load determination stems from zoning approximate wind speed maps, model error in the velocity exposure coefficient, and uncertainty in the site specific directionality. As a result of these sources of uncertainty, V, k_z, k_d and G_{cp} are random variables, and necessitate statistical modeling [31]. Starting in the 1970's effort was made and reported on characterizing statistical distributions for use in probabilistic reliability assessment [14]. Through a delphi, Ellingwood solicited beliefs of 20 experts from industry and academia to characterize the wind load statistics for use in PBD as shown in Table 7 [33]. The characterized wind load statistics are for certain scenarios such as Exposure B with mean height $z = 20ft$. There is limited evidence in the literature to suggest how these statistics vary across scenarios but wind tunnel testing provides a practical approach for quantifying statistics for specific scenarios of interest. The case studies developed in this thesis are developed to match the cases for which statistical models have been published.

Table 7: Statistical model for Wind Load variables [33]

Parameter	Nominal	P_m	COV
k_z (Exposure B z=20ft)	0.62	0.98	0.12
GC_{pf} (Zone 2) [1]	-.69	0.85	0.10
GC_{pf} (Zone 2E)	-1.07	0.80	0.15
GC_{pi} (uniformly distributed openings)	.18	0.83	0.05
k_d	0.85	1.01	NR

P_m is the ratio of mean to nominal value and COV is the coefficient of variation. $P_m = 1$ indicates the mean strength and nominal value are equal, while $P_m < 1$ indicates the nominal value is greater than the mean value.

3.3 Extension to residential PV systems

While the broad notion of wind hazards including air-born debris is generally applicable to residential PV systems, the hazard of principal concern in PV systems is the

structural loads that may contribute to excessive stress or deflection. Currently, in most U.S. jurisdictions, the structural wind loads used in the design of PV systems are determined through ASCE 7-2005 or 7-2010 ASD or LRFD. In both cases, a stakeholder does not have publicly available information to discern the statistical likelihood of a wind load induced structural failure during the 25 year expected performance period. The information regarding structural performance and location specific wind speeds are not coupled. In fact, it is not uncommon for a project developer to measure site specific wind speeds or select a sub-set of super-station historical data sets to develop a more accurate assessment of local wind speeds than is available through ASCE national wind speed maps. In this case, a structural analysis should not embed wind speed distributions but rather quantify structural performance as a function of wind speed such that local wind speed knowledge may be coupled on demand with structural performance quantification. In light of this we need an improved risk assessment method that is compatible with independent wind models. Consequently, the following hypothesis has been developed and tested.

Hypothesis: A fragility based performance measure provides a platform for comparing performance risks of code designed residential PV systems.

Sub-Hypothesis 1: A fragility based performance measure provides a platform for comparing performance risks of alternative code designed system types at a particular wind speed.

Sub-Hypothesis 2: A fragility based performance measure provides a platform for comparing performance risks of alternative code designed system configurations at a particular wind speed.

Testing of this hypothesis requires development of a structural limit state, development of a structural model, and identification of random variables and associated statistics. Each of these steps will be presented in the following sections and demonstrated in a case study.

Table 8: Sample limit states for PV systems

LS#	LS class	Limit State
1.	serviceability	bending stress in single rail equals yield stress
2.	serviceability	tensile pullout in single fastener equals rated fasteners capacity
3.	life safety	bending stress in system (two or more rails) equals yield stress
4.	life safety	bending moment in module clamp equals yield stress

3.3.1 PV system wind load limit states

A PV system attached to a residential roof exposed to wind loads is subject to a range of limit states. At low wind speeds one may judge the probability of occurrence for any wind related limit state to be near zero. While at extreme high wind speeds, one may judge the probability to be significant. However, there is no established methodology or supporting data for quantifying the probability of structural failure of a residential PV system at a specific wind speed. Further, structural limit states in the current code only incorporate failure modes that may result in significant damage or collapse rather than serviceability related failures. So, while a code engineered PV system may ensure reasonable yet un-quantified catastrophic failure risk, no such assumption may be made regarding production risk or other serviceability risk. Given the importance of continued energy production with limited degradation, a quantification method for serviceability failure modes is needed for PV systems. The established approach to quantify both serviceability and life safety risk is through limit state based performance measure [29], [5], [51]. Over time limit states and associated performance measures should be established for power production, system protection, building protection, and life safety. Table 8 provides a sample set of limit states for further refinement and development by industry stakeholders.

The concept of damage states also has a potential role in improved PV system

decision making by engineers, policy makers, financiers and insurance agents. However, the current body of knowledge may not yet support development of damage states because of the complex interaction and uncertain relationship between structural limit states and system damage [74], [54]. Alternatively, probabilistic treatment of potential damages may be utilized to provide an assessment of damage risk in future work.

3.3.2 Applicability of wind load Statistics

The wind load statistics generally accepted for Main Wind Force Resisting System and Component and Cladding systems are considered applicable to PV systems [17]. However, PV systems attached above a residential roof surface have been shown to experience unique fluid dynamics phenomena that substantially affect the net pressure coefficient [39]. These recent findings suggest that application of MWFRS pressure coefficients to PV system design and fragility analysis may be considered erroneous. This hypothesis will be tested in Chapter 4.

3.3.3 PV Structural Model

Translation from the proposed limit states to fragility models requires identification of the structural and mechanical behaviors for analysis or testing. For example, LS #1 related to local bending stress may utilize beam theory to relate the wind load into bending stress. Typical structural models for PV systems will include stress and strain and may require multi-physics coupling with thermal and electrical models. Dynamic models are required when the structures natural frequencies is less than 1 Hz or when an array of structures adequately disrupts the wind flow to create dynamic response below the 1Hz threshold [11]. Most frequently, wind loads applied to residential PV systems are treated as a quasi-steady state load [11]. Structural models developed for static wind load bending stress analysis will be demonstrated in the case study for each system type under consideration.

3.4 Case Study: Fragility Analysis

The case study introduced in Chapter 2 will be further developed to demonstrate an approach for fragility analysis on residential PV systems using sample LS#1, rail bending stress. The deterministic wind load determination in Chapter 2 is refined with a stochastic analysis that accounts for the random variables in Equations 21 and 22. Subsequently, structural analysis for each design case supports determination of the American Iron and Steel Institute (AISI) compliant member strengths. Finally, the random variables that influence resistance will be introduced into the structural analysis through Monte Carlo simulations to generate a CDF for $G(X)$, the fragility model.

3.4.1 Stochastic wind loads

Stochastic treatment of wind loads first requires a statistical model of the wind velocity pressure based on treating k_z, k_d and GCp as random variables defined by Table 7. Monte Carlo Simulation is used to sample values for each of the random variables 1000 times to produce the distribution shown in Fig 17.

Application of the wind load statistics in Table 7 to the case study building and site requires two assumptions to be made 1) P_m and COV values for zone 2 and zone 2E can be combined through a weighted average to generate P_m and COV values for systems that span multiple zones and 2) P_m and COV for a 0° roof are also applicable to 15° and 45° roofs.

Using the weighted averaged wind load statistics, a probability density function for q can be developed through Monte Carlo Simulation with 1000 runs. The frequency illustrated in Figure 17 suggests a normal distribution with a mean value for $q = 11.1psf$ and $COV = 0.22$. An additional 1000 runs results in less than 1% difference in the mean and no change in COV.

The nominal q value, (Calculated in Chapter 2 as 10.9 psf for the case study)

used for ASCE design has a 53% chance of exceedance. Introduction of the load and resistance factored design (LRFD) load factor of 1.6 for principal action results in a factored $q = 17.44$ which is 2.5 standard deviations from the mean and has a 1% chance of exceedance during a 90mph 3-second gust. Partial validation of this result is made by replacing the 50 year return period wind speed V(50) with the 700 year return period wind speed V(700) calculated with Equation 32 [63]. Use of V(700) in lieu of V(50) results is $q = 17.5$. This in only a partial validation because it confirms the calculation of q not the probability of exceedance which depends on the validity of wind load statistic used for sampling. For the purpose of this thesis, the statistics derived from 20 expert opinions are considered to be a valid starting point. If however, the methodology demonstrated in this thesis were to support a project specific decision of great consequence, and the decision has high sensitivity to the statistics used, a site specific wind tunnel study is recommended to update the statistics.

$$V(700)/\sqrt{1.6} = V(50) \tag{32}$$

3.4.2 Stochastic resistance statistics

Analysis of the required moment resistance is conducted for each O-D, 1-D, and 2-D design case. The wind pressures for each design case shown in Table 5 and the configuration influence area diagrams shown in Figure 14 are treated as inputs. structural analysis for each systems is then conducted through definition and analysis of the following steps 1) tributary area, 2) boundary conditions, 3) free body diagram, shear diagram and bending moment diagram 4) maximum and minimum bending moment as a function of wind pressure for each design case and 5) factored load and resistance.

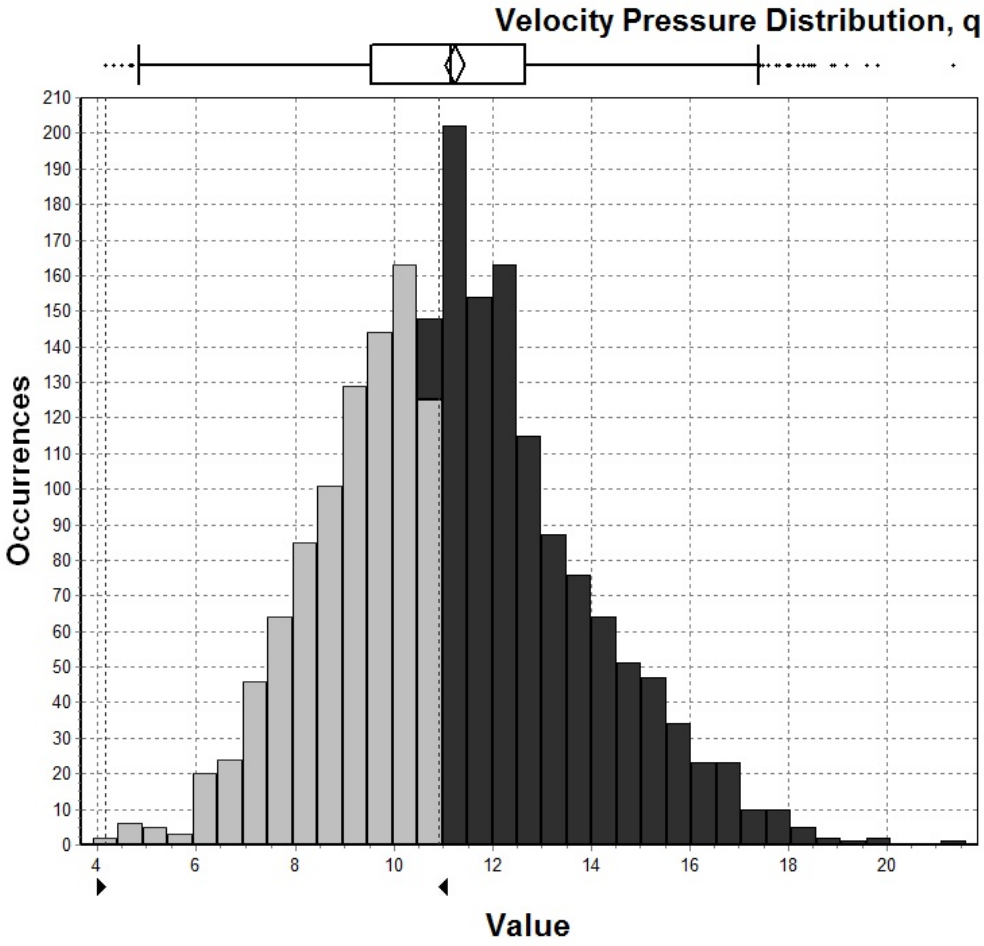

Figure 17: Likelihood of exceedance nominal pressure in 90mph wind pressure distribution

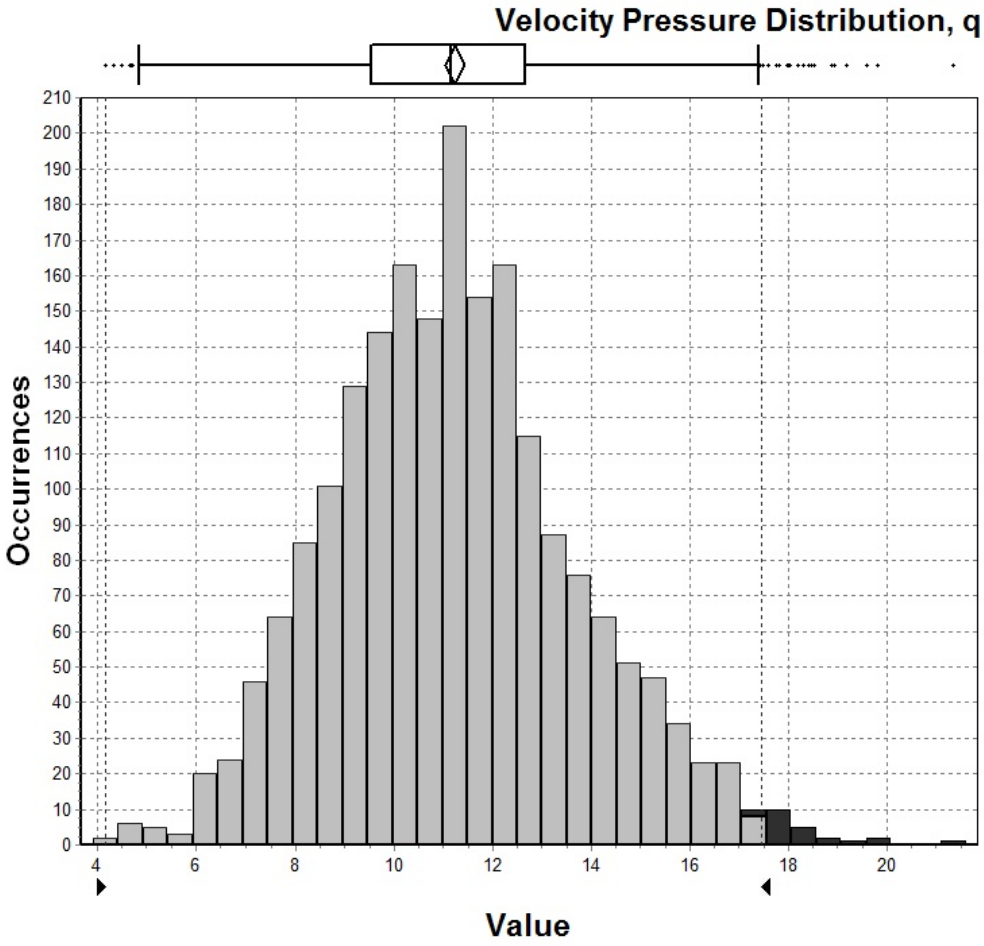

Figure 18: Likelihood of exceedance factored pressure in 90mph wind pressure distribution

Tributary Area Determination of the tributary area for each case requires identification of the structural load path and geometry. As discussed in Chapter 2, the tributary area differs from the influence area identified in Chapter 2 because the tributary area is the actual area over which the average pressure from the influence area is applied to calculate a load [23]. O-D systems transfer loads from a module attachment hole to a roof attachment bracket located at an adjacent roof rafter. Depending on the location in the array, a 0-D system may attach a single corner module, up to two edge modules and up to 4 interior modules with a bracket. Given a roof attachment bracket is located in the corner of each module, the tributary area for the aforementioned cases are 1/4, 1/2 and 1 module area as illustrated in Figure 19. For the purpose of this design case, the worst case tributary area of 1 module will be assumed. A typical 60 cell Si-crystalline module with area, $A = 18.3ft^2$ is used for analysis [24]. Currently, there are indications that the market could shift to either larger modules for component count reduction or smaller modules for improving layout flexibility and handling. Similar analysis is conducted for the 1-D and 2-D system types. Figures 20 shows inset parallel structural rails under a column of modules with shaded tributary area extending from the module edge (aligned with guide D) halfway across the module. The resulting tributary area is 1/2 module wide by 5 modules long for a total area of $2.5A$. Similarly, Figure 21 shows a structural rail located below the union of two module columns with half the area from each column contributing to the $5A$ tributary area. While the assumed layouts for tributary area calculations are representative of actual system layouts alternative layouts are also common. For the purpose of this case study tributary area is considered critical and a range of values are considered.

Boundary Conditions and Free Body Diagram The tributary area along with assumed module dimensions and typical residential rafter spacing allows for a free body diagram to be produced. The free body diagram concentrates wind load applied

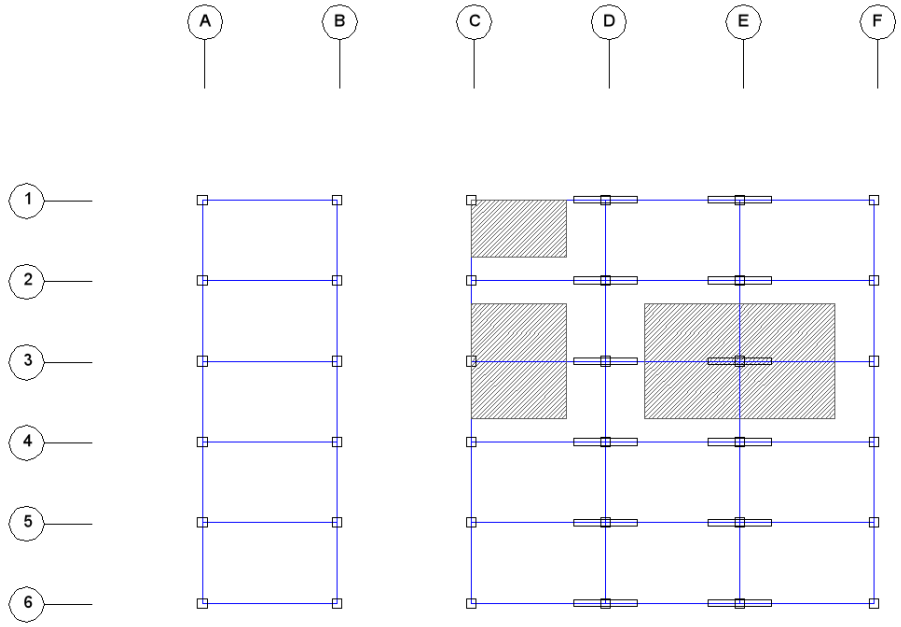

Figure 19: Example corner, edge, and interior tributary areas

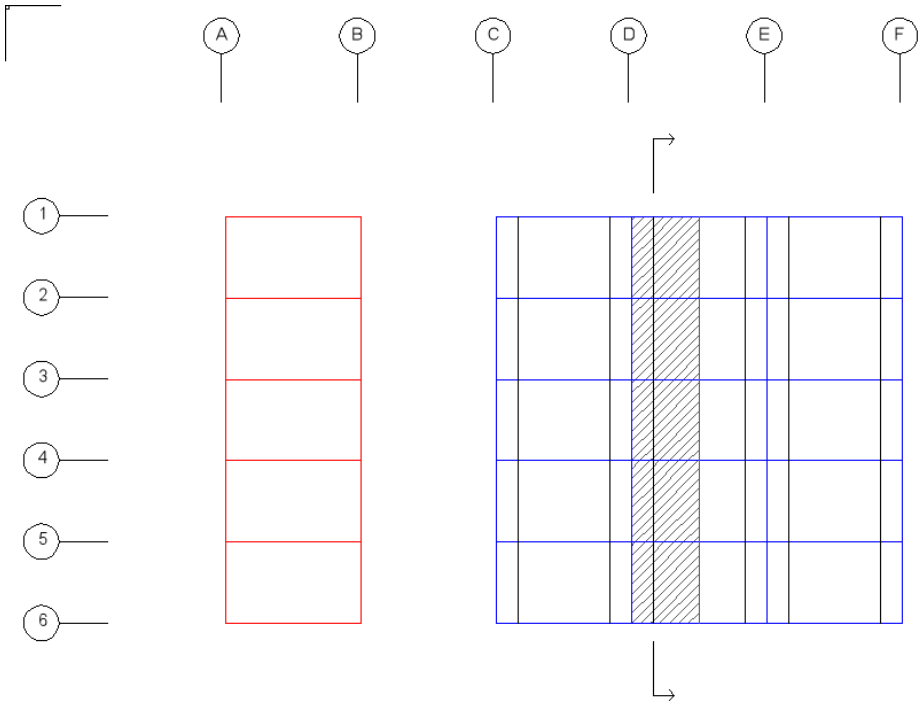

Figure 20: Example 1-D interior rail tributary area

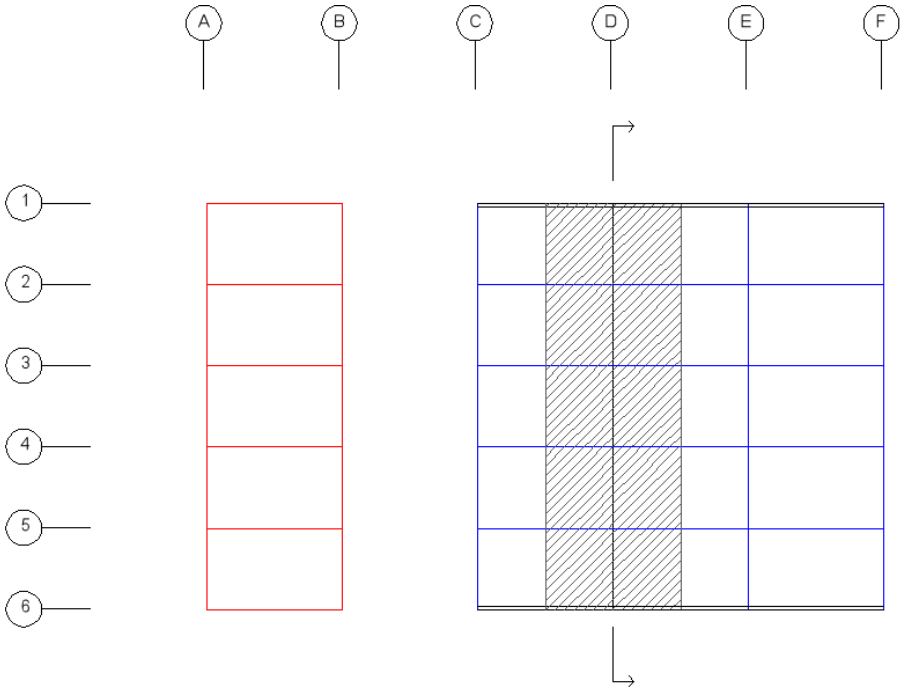

Figure 21: Example 2-D interior rail tributary area

to one quarter of module surface as a point load at each of four module attachment hole locations. The structural member transfers load from the module attachment location to the roof rafter, the length of the load path depends on the permitted PV system layout. For a 0-D system, a rafter may be centered between two modules or offset to one side, alternative 0-D strategies can be found in industry [79], [78], [44] however this case study is not representative of any specific commercially available systems. For the purpose of this case study the rafter attachment is constrained to the inner third of the member length, L as shown in the free body diagram and associated shear and moment diagrams as shown in **??**. Because the 0-D system type has a single point of connection, it is assumed to be a moment connection. For 1-D systems a column of modules is assembled on a structural rail. Currently, industry is moving towards factory assembled 1-D systems to achieve greater overall labor productivity. This approach utilizes two parallel structural for a column of modules, both located along the module attachment holes. Roof attachment strategies for 1-D members vary,

for this case study the members will be treated as simply supported, a conservative assumption compared to a member fixed at both ends or a member with additional midspan supports[25]. 2-D systems, utilize a traditional 1-way structural system [23] with a primary member located under two adjacent module edges and extending to the support of a secondary member. The secondary member typically supports multiple primary members and transfers loads into the roof structure. For this analysis both the primary and secondary members are treated as simply supported. Finally, for each design case, free body diagrams are used to derive shear and moment diagrams.

Maximum and Minimum Bending Moment Using the location of the maximum moment found in the moment diagrams, first order statics are applied to determine magnitude of the maximum moment according to Equation 33.

$$\sum M = 0 \tag{33}$$

For example, the maximum moment from wind on a 0-D system is given by equation 34.

$$M_w = P_w A(2L/3) \tag{34}$$

Factored Loads and Resistance

Determination of a code compliant design load requires consideration of loads which may occur simultaneously to be combined through load combinations. The ASCE load and resistance factor design (LRFD) approach provides a framework for combining probabilistic loads through load factors γ, along with a resistance factor ϕ in the general Equation 35 [29].

$$\phi R_n > \gamma_D D_n + \gamma_{max} Q_{max,i} + \Sigma \gamma_i Q_{ni} \tag{35}$$

.

LRFD recognizes that transient loads due to unique hazards such as wind and snow are unlikely to have peak values simultaneously and therefore assigns a load factor γ_{max} to the principle action $Q_{max,i}$ and separate companion load factor γ_i to each of the companion loads Q_{ni}. Permanent loads D_n are allocated load factor γ_D which may be greater or less than one based on uncertainty and whether the permanent load has positive or negative superposition with $Q_{max,i}$ [32].

Using this framework, ASCE provides a series of load combinations that are used to envelope the design. Each member or even member feature such as connection details and cross section are typically governed by specific load combinations. For the PV rail members under consideration, Equation 36 governs the required cross section positive bending moment by accounting for the combination of actual dead load D exceeding the nominal value by 20% , wind load W exceeding nominal by 2.5 standard deviations, and a companion snow load S of 50% nominal occurring concurrently. Based on solar panel installation and operating manuals, no live load L is permitted during the operating life resulting in $L = 0$ [24]. Alternatively, equation 37 is used for uplift based on the likelihood of the actual dead load being 10% less than nominal and no snow load counteracting the wind uplift [11]. Earthquake loads also require consideration in some jurisdictions but are not considered further in this case study.

$$1.2D + 1.6W + L + 0.5S \tag{36}$$

$$0.9D + 1.6W \tag{37}$$

Maximum moments for snow load, M_s and dead load, M_D on the 0-D system for use in Equations 36 and 37 are provided in Equations 38 and 39.

$$M_s = P_s A(2L/3) \tag{38}$$

$$M_D = 2.5(4/18)L^2 + 2 * W_{mod}L/3 \tag{39}$$

where W_{mod} is the module weight per foot.

The resistance factor ϕ intended to account for uncertain resistance is established by the American Iron and Steel Institute (AISI). Resistance factors for cold formed steel are based on the failure mode. For lateral torsional bucking resistance factor $\phi = 0.9$. The resistance factor, is used to calculate a factored strength ϕR_n.

Manipulation of Equation 35 allows design resistance, R_d to be solved in closed form as shown in Equation 40. Treatment of the principal action wind load, as a random variable can be accomplished by incorporating the Monte Carlo simulation for wind pressure in the determination of a stochastic design resistance or required moment capacity.

$$R_d = \frac{1}{\phi}(\gamma_D D_n + \gamma_{max} Q_{max,i} + \Sigma \gamma_i Q_{ni}) \tag{40}$$

.

Sources of resistance uncertainty include aleatory uncertainty in the material strength, precision in the member geometry and epistemic uncertainty in models used to predict member strength. For common steel, the material yield strength alone has a coefficient of variation of 0.09 [76]. However, additional uncertainty is introduced by member geometry. Through a review of structural test on cold formed steel sections similar to those commonly used in PV system rails, moment strength statistics (Table 9) have been experimentally measured and account for both the aleatory and epistemic uncertainty. $P_m = 1.09$ indicates that mean strength is 9% greater than nominal strength and 21% greater than the factored strength. Further, with a $COV = 0.12$ the factored strength has a 93% chance of exceedance.

An expression for actual moment strength, M_a can be developed through combination of the strength statistics with the required moment.

Table 9: Cold formed steel section strength statistical model adapted from Schafer 2008 [67]

Parameter	P_m	COV
M_cr	1.09	0.12

$$M_a = \frac{M_{cr}}{M_{nom}} M_d \tag{41}$$

Such that by combination of Equation 41 and 40 the actual moment strength is given by Equation 42.

$$M_a = \frac{M_{cr}}{M_{nom}} \frac{1}{\phi} (\gamma_D D_n + \gamma_{max} Q_{max,i} + \Sigma \gamma_i Q_{ni}) \tag{42}$$

.

3.4.3 Case Study Fragility Curves

Evaluation of the fragility curves is conducted using the criterion that a limit state is exceeded when $G(x) < 0$. As discussed in Chapter 1 the exact method based on Monte Carlo analysis is used to develop a multivariate distribution with random variables M_a and M_d for wind speeds V ranging from 70 to 170 mph as defined by Equation 43. Numerical integration of the area exceeding the limit state provides an estimate for the probability of failure at each value of V.

$$V = [70 : 20 : 170] \tag{43}$$

Moment demand can be calculated from the load combinations for each value in V using Equation 42. According to the ASCE commentary, the value of the companion load factor, γ_i is set to represent an "arbitrary point in time value" and the value of 0.5 was established to provide equivalent reliability to historical structures. Consequently, the choice of a γ_i value for use in the fragility curve is also arbitrary and up to the decision maker using the curve. In practice, multiple fragility curves should be

composed with varying γ_i values. Moreover, in the combined event of wind and snow on a residential PV system, the accumulation of snow affects the aerodynamics that govern wind loads such that the uncertainty in pressure coefficient statistics should be updated. For the purpose of this case study a value of $0psf$ will be used for γ_i because in the opinion of the author, it is erroneous to apply experimentally determined wind pressure coefficients measured without snow. Further investigation into the historical frequency of combined wind and snow events is recommended along with evaluation of snow affects on wind load. Iteration of the G(X) function 1000 times for each design case applied to 15°, 30° and 45° roofs yields the LS#1 fragility curves shown in Figures 22 through 24 for a compliant system designed for a 90mph wind zone. For the 15° and 30° roofs, the average θ is approximately 130 mph with less than 4 mph standard deviation. The 45° curve is shifted left with the average θ occurring at approximately 120 mph.

3.4.4 Fragility Curve Validation

The fragility curves shown assume that input uncertainty and model form uncertainty are adequate to support a decision. The American Technology Council single calculation method method for fragility curves (Equation 30) provides a benchmark for validation. The single calculation method is based on a nominal wind speed capacity Q which is determined by setting the load factors to unity and solving for V given M_d. On average for the design cases, the nominal wind speed capacity $Q = 110MPH$. Using Q and the ATC recommended value of $\beta = 0.4$ the dashed curve shown in Figure 25 is produced which has a theta less than 5% greater than the average θ and within 1.5 standard deviations.

While the single calculation method does provide limited validation that the Monte Carlo simulation accounts for a typical amount of uncertainty in the structural calculation, it can not validate the underlying physical models. As discussed, the literature

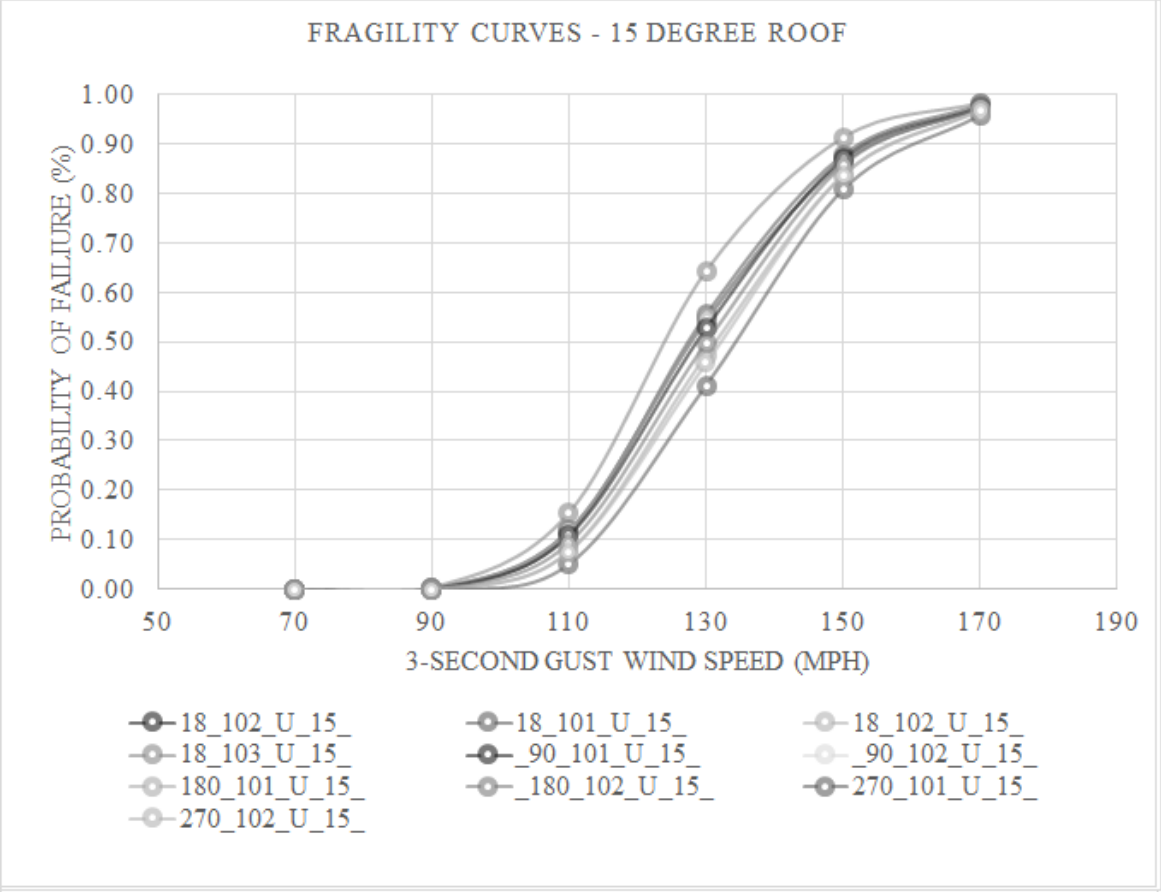

Figure 22: LS#1 fragility curves for code compliant system, 15 deg roof, 90mph wind zone

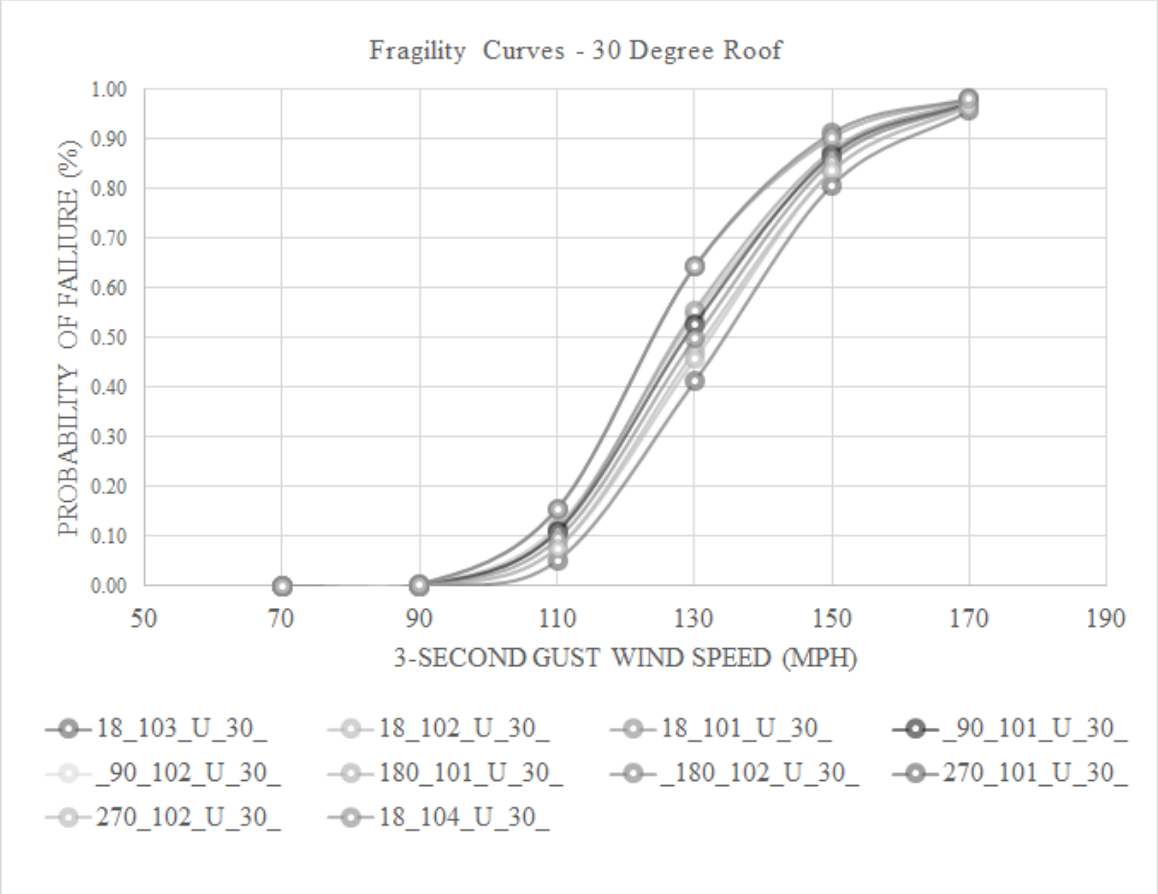

Figure 23: LS#1 fragility curves for code compliant system, 30 deg roof, 90mph wind zone

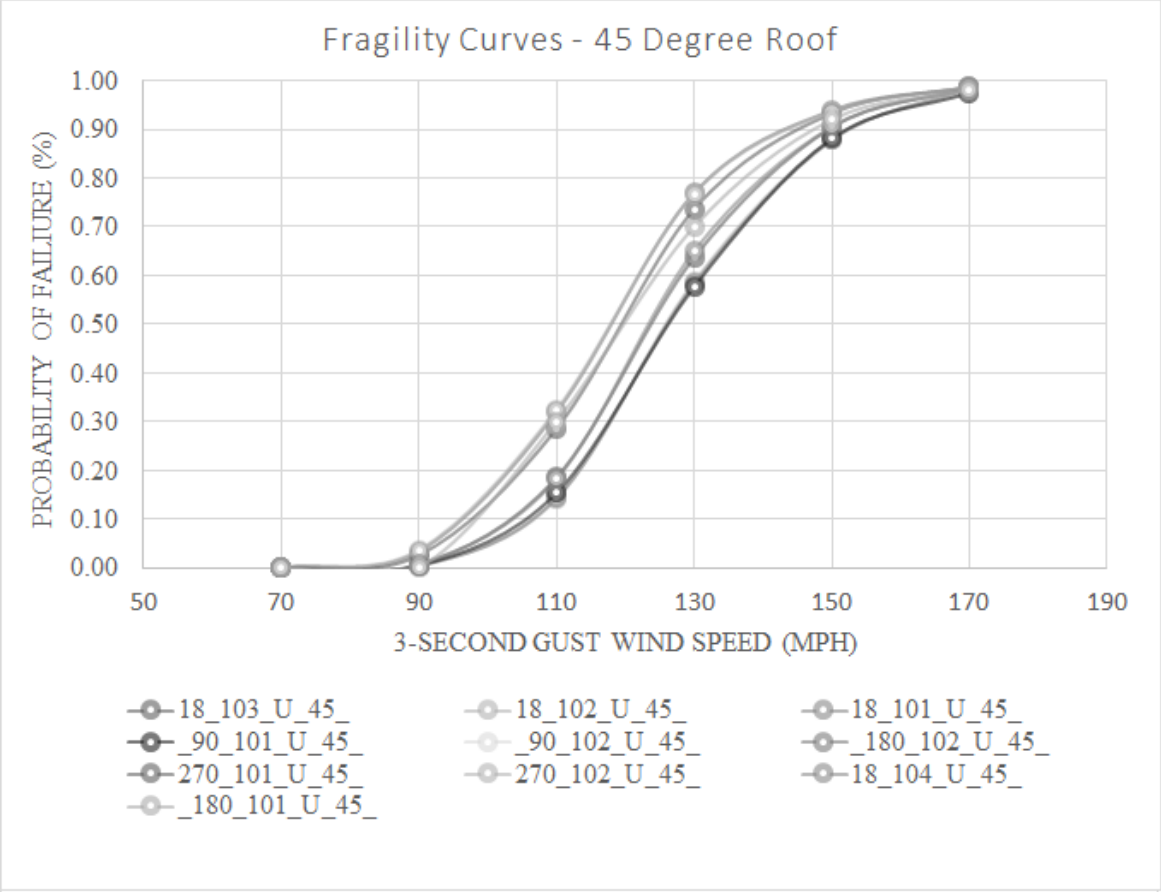

Figure 24: LS#1 fragility curves for code compliant system, 45 deg roof, 90mph wind zone

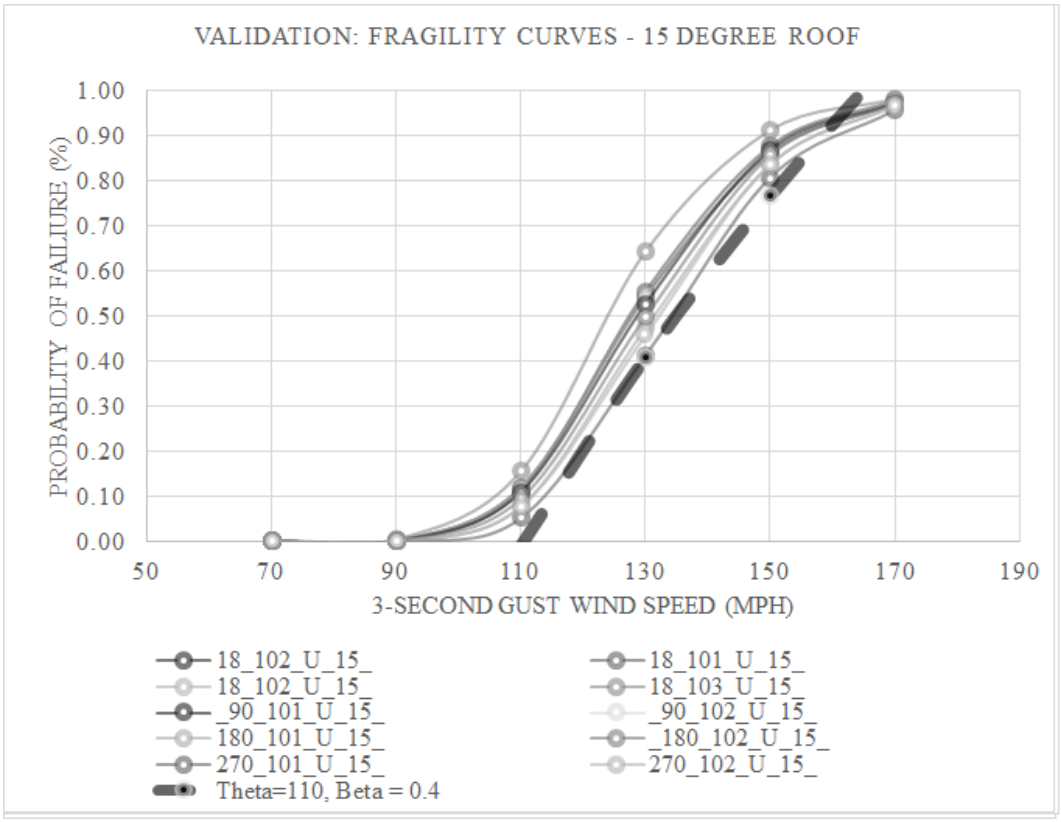

Figure 25: Validation curve for 15 deg roof

suggest the greatest risk to model validity is erroneous GCp values. Experimental investigation of GCp values will be presented in the following Chapter along with updated fragility curves.

3.4.5 Fragility Analysis Conclusions

From the fragility curves presented, a clear performance statement for LS#1 can be constructed to read, that design case 1 engineered to code for a 90mph wind zone and installed on a 15° degree roof has a 50% probability of failure in a 130 mph 3-second gust. Further, one can differentiate between system types noting that 270 sq.ft. 2-D systems types have a 44% average probability of failure at 130 mph wind speed on a 30° roof compared to 58% for the 1-D system types. In conjunction with upfront system cost, this is a valuable performance measure that can support the selection between system types.

Finally, system layouts can be evaluated based on the LS#1 performance measure by comparing the design cases of similar types. For 1-D systems installed on a 15° roof, the edge design case has a 54% probability of failure compared to 64% for the interior case when designed according to code. This illustrates that although the edge may be subject to higher loads, the wind load statistics for the edge introduce more conservatism than the interior because of the higher uncertainty, and corresponding lower ratio of mean to nominal pressure coefficient, P_m.

Clearly, the fragility curves are valuable for making a reliability comparison at a given wind speed. However, some project specific decisions benefit from incorporating a belief about predicted wind speeds. Most generally, one may believe that any wind speed is possible and formulate a preference accordingly. Alternatively one may believe that a wind speed greater than 90 mph has an acceptably low likelihood of occurrence during the service life. In that case the fragility curves do not support a preference between system types. Chapter 5 will explore and demonstrate methods

for incorporating wind speed statistics into the reliability assessment. First, Chapter 4 will examine the literature reporting on solar panel wind pressure coefficients and report on a wind tunnel experiment to measure pressure coefficients on each of the design cases considered.

CHAPTER IV

PRESSURE COEFFICIENT EXPERIMENT

Current state of the art PV system design either utilizes pressure coefficients, GC_P derived from the building code or from system specific wind tunnel experiments. Pressure coefficients prescribed by the building code are also derived from wind tunnel experiments however, the experiments utilized to inform code were conducted on residential buildings without PV systems [11], [12]. The current body of literature suggests that the application of pressure coefficients measured on roofs without a PV system to the design of PV systems may be erroneous. Further, application of erroneous pressure coefficients, propagates to erroneous understanding of structural reliability performance, scientific effort is needed to measure and analyze pressure coefficients specific to applied residential PV systems through wind tunnel studies [17].

In response to the call for residential PV system wind tunnel studies, a set of experiments has been conducted as part of this thesis. To support the design of experiment, a literature review has been conducted in three parts. This chapter will present findings from the literature review. Also presented is this chapter are the series of wind tunnel experiments conducted on the design cases under consideration. Finally, the experimentally measured pressure coefficients are used to generate independent wind load statistics for use in revised fragility curves and further reliability analysis in Chapter 5.

4.1 Wind Tunnel Experiments Literature Review

Underwriters laboratory (UL) and the American Society of Civil Engineers (ASCE 7) establishes structural loads for PV modules and racking system. UL loads are used

for general module and racking product design, while ASCE loads are used for specific PV systems installations in the built environment. UL 1703, the safety standard for PV modules and UL 2703 the standard for module racking systems both prescribe a design load of 30 psf for wind forces and requires the product to survive a test condition of 45 psf [4],[1]. A module or system is required to withstand the test load for a period of 30 minutes without evidence of structural or mechanical failure [4]. Installations of UL certified PV products in the built environment are governed by the building code ASCE, Chapter 7-05 or 7-10 and must be designed according to the minimum design loads set forth in the code [11].

Recently guidance has been issued for how best to navigate the multiple methods available in ASCE given that no one method accurately reflects the condition of solar modules mounted over roof surfaces [17]. Wind tunnel testing has also been conducted to determine design loads experimentally, with the intent of permitting a specific design or informing a code revision [40], [53], [52], [20].

The following literature review is structured in three parts. First a review of experimental conditions, influential flow phenomena and findings will be presented from a cross section of the commercial and ground mount PV systems tested. Next, the limited literature on residential PV system wind tunnel test will be reviewed both for methodology and findings. Finally, guidance on the application limitation of existing codes, along with potential changes in future code revisions will be reviewed.

4.1.1 Commercial and Ground Mount PV system experiments

The Solar Energy Research Institute analyzed wind loading on tracking and field mounted solar collectors. Flat plate solar collectors are noted to be constructed with over-built support structures which can lead to substantial costs. According to the authors, this motivates increased understanding of wind forces on solar collectors. A method for conducting scale wind tunnel experimentation using dynamic similarity

is identified such that force coefficients can be experimentally determined and then applied to calculate lift forces for scenarios of constant Reynolds number Re. Tests were conducted to identify effects of varying conditions on lift coefficients GC_{p-} for flat plate collectors. GC_{p-} for at solar panel mounted at 35° angle of attack was found to be -0.9. Fences and wind shields with porosity of 0.3 to 0.4 were found to have significant effect on wind loads [60].

Wind tunnel testing to determine wind pressure on solar energy systems was conducted by Bronkhorst at the TNO atmospheric boundary layer (abl) wind tunnel [19]. A boundary layer roughness length of 2.4mm was applied in 1:50 scale testing for full scale roughness length Z° of 0.12 m. The wind speed in the tunnel was 10.7 m/s with turbulence intensities of 15% longitudinal and 12% vertical. The building full scale dimensions were 10 m heigh, 30m wide and 40m depth. Use of symmetry allowed the researches to examine unique configurations in each corner. The solar energy system was modeled with an inclination angle of 35° and a solid base as shown in Figure 26. The configuration shown does not allow for any pressure equalization to occur and would essentially result in a GCpi = 0. These results were compared against CFD analysis that solved the Reynolds Averaged Navier-stokes (RANS) equations with either a renormalization group (RNG k-Epison turbulence model or differential reyonlds stress turbulence model (DSM). Both turbulence models were found to produce well matching results with the greatest deviations when large gaps between modules were present [19].

Wind tunnel tests for commercial flat roof PV systems was compared to CFD analysis that employed alternative turbulent models. For the wind tunnel test, a one-half scale module of a 10° sloped PV tile was constructed and connected to a five component load balance. An additional 8 modules were placed around the connected module to form a 3x3 array. Varying aerodynamic treatments were installed in a series of 92 tests. Pressure coefficients for all cases reported ranged between +/-0.2

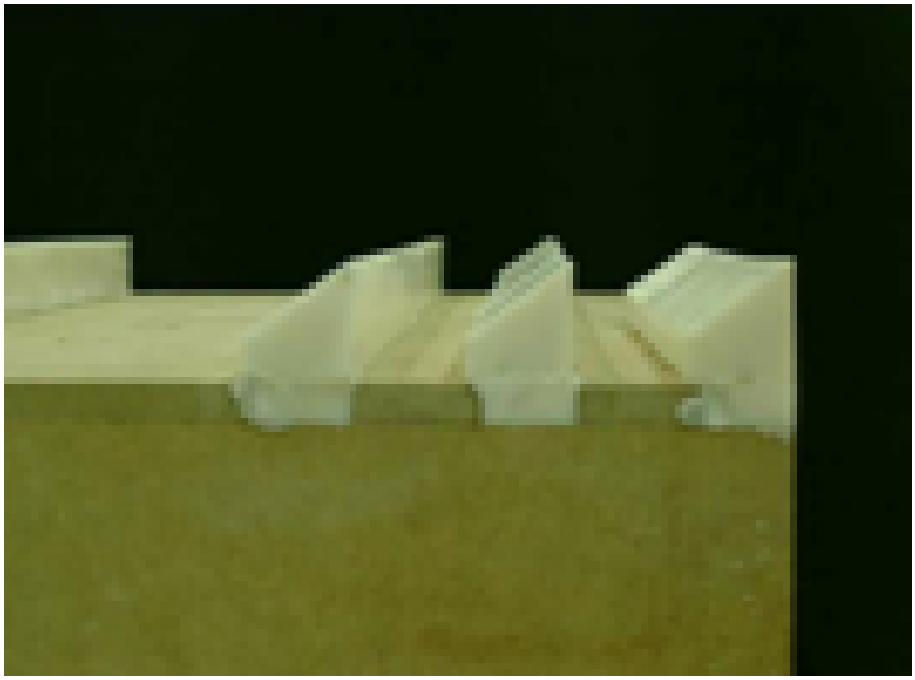

Figure 26: Bronkhorst wind tunnel test reference [19]

[57]. No building was included in the wind tunnel testing.

Boundary layer wind tunnel testing was conducted by Kopp [53] to investigate the effect of building size, and effective wind area on the pressure coefficients of low tilt PV modules mounted on flat roofs. The experimental setup utilized 1:30 scale building and array composed of 12 rows of 12 modules. Tilt angles of 2°, 5°, 10°, 20° and 30° were tested with inter-row spacing sized to prevent self-shading and 1.2 m building edge set back (Figure 28. Modules were fabricated in 3 module panels with 12 top and 4 bottom pressure taps per module. The array was tested on three building roof heights with the intent of varying the intensity of cornering vortices. Reynolds number based on roof height was reported to be 1.9E5 about half the full scale value but still greater than required by ASCE 67 [46]. Results showed that increasing the building size and in particular the North South wall area, HL, increased the wind loads. Further Kopp found that if one scales the effective wind (or tributary) area by the wall size, HL, then the area-averaged pressure coefficients, GC_p, will

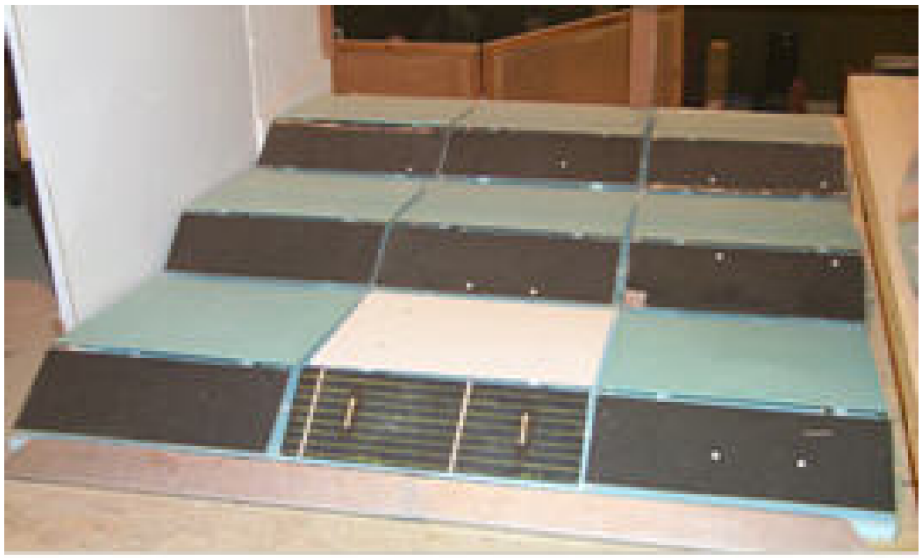

Figure 27: Meroney and Neff wind tunnel test reference [57]

collapse onto a single curve for a particular array geometry [53]. This phenomena is attributed to the conical vortices which form during cornering winds and strengthen due to continual flow separation along building edge.

Banks reported on the effect of cornering vortices on flat roof PV systems through a review of 20 proprietary studies conducted at CPP [16]. Typical experimental setups utilized exposure C with some exposure B, and typical wind tunnel blockage was below 7%. Building dimensions of $B = L = 6H$ were typical, although larger buildings with 20Hx10H were also tested for large PV arrays. As shown in Figure 29 9 blocks compose a full 6H building. PV systems were tested on each block with 10 deg rotation with six taps on top surface, and two on lower surfaces. Over 80% of test were conducted between 1:40 and 1:50 scale. Pressure was sampled at 250 or 500 Hz for 30-120 sec per rotation angle. Geometric distortion from module thickness occurred but it was considered less important than the gap between modules. The analysis included use of transfer functions to correct for the frequency response of tubing. Area averaging measurements from multiple taps was conducted to determine pressures for each module. Due to model scaling, investigators utilized high frequency spectrum

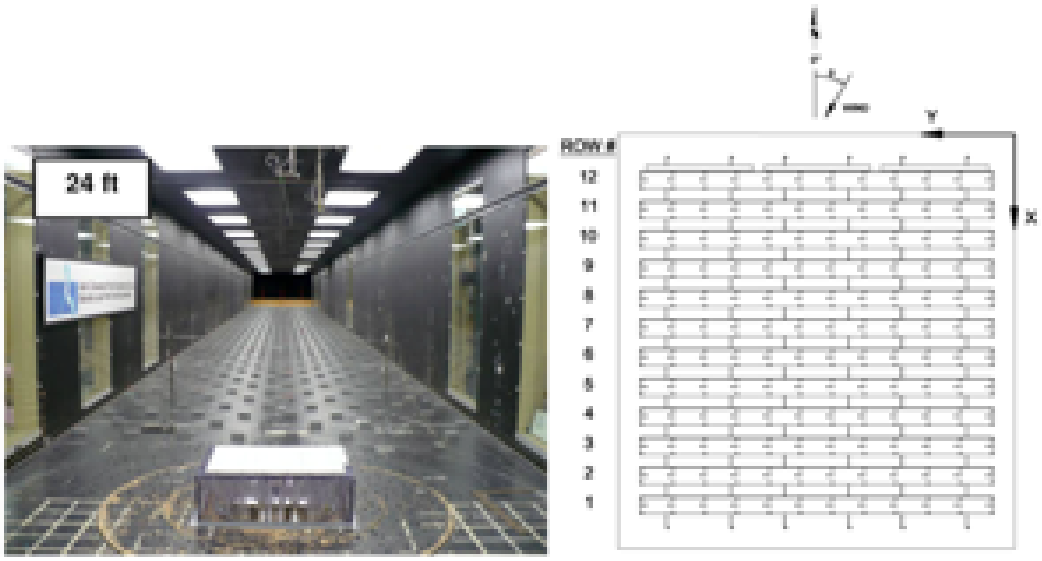

Figure 1. Photograph of the model array (left). Sketch of the array layout (right) with co-ordinate definitions (x, y), row numbers and wind direction, & Taps on the upper surface of the array are marked with '+', those on the underside are marked with 'O'.

Figure 28: Kopp wind tunnel test reference [53]

matching method as described by Banks (2011) and Dyrbye and Hansen (1997). This method matches the energy in the spectrum at frequencies above the quasi-steady threshold. GC_n values are calculated directly from Equation 22.

Results indicated GC_n varies with the gap above the roof $h2$, peak height above the roof $h1$, row spacing and deflector design as illustrated in Figure 30. Modules closest to the 0 and 90° edge with an offset of 0.03H and 0.2H were not found to have an appreciable difference in lift compared to center modules, suggesting the edge separation bubble has little impact. Modules between 1H and 3H from the 180° edge experienced uplift due to the reversed flow inside the separation zone. The author recommends utilizing an edge zone of 3H wide along the edge to which modules are oriented. The effect of parapet height ph normalized to building width B (ph/B) was found to increase uplift forces because the vortices are not disturbed up until a ph/B ratio of 0.04 at which point the vortices are safely above the module height although still stronger. Further, wind deflector design was found to have significant effect on wind pressures experienced by the module. The most dominant flow phenomena on

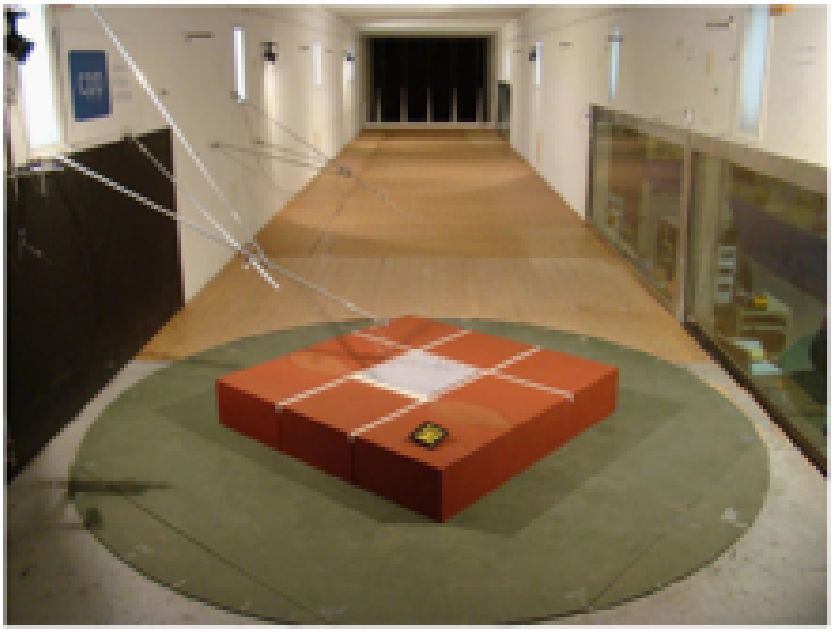

Fig. 3. Photo of a typical wind tunnel test to measure pressures on an array of solar panels. For this test, the array is positioned in the middle of a low rise building of height *H*. The building is square, with a side length of 6*H*. The array is tested in nine different roof positions.

Figure 29: Banks wind tunnel test reference [16]

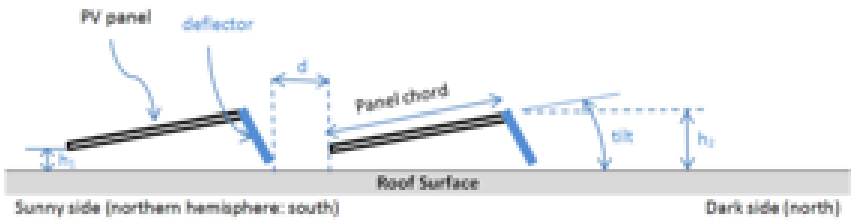

Figure 30: Banks array layout [16]

uplift forces was found to be corner vortices. In fact, cornering vortices were found to significantly impact uplift of modules beyond the ASCE traditional edge zones. As a result the authors recommended adoption of expanded edge and corner zones for codified PV wind loads.

Stathopoulos reported on an atmospheric boundary layer wind tunnel test to evaluate the effect of tilt angle, building height and module location of solar modules on flat roofs [70]. The experimental setup utilized a 1:200 module scale of a 20.6m by 30.6m building and heights of 7m and 16m. Module tilt angles ranged from 20° to 45° (Figure 31). Positive pressure was found to be greatest for windward modules and increased with module tilt angle. Wind uplift (suction) was found to be greatest for the leeward location and decreased with inclination. The reference of the model apparatus show in Figure 31 suggests the model building faade was not enclosed with a wall which has been reported to influence the formation of cornering vortices a significant factor in peak loads [16].

Browne utilized wind tunnel experimental data to evaluate the effect of load sharing in ballasted roof-top solar arrays. The experimental setup utilized a 1:70 scale building and array model with pressure taps distributed throughout the array to record the variation in wind loads. The results indicated a high level of spatial and temporal variation in loads due to the high frequency content of building generated turbulence as illustrated in the sample time history of peak forces on a module (Figure 32. Due to the rapid rate of change, adjacent modules are not expected to see a peak

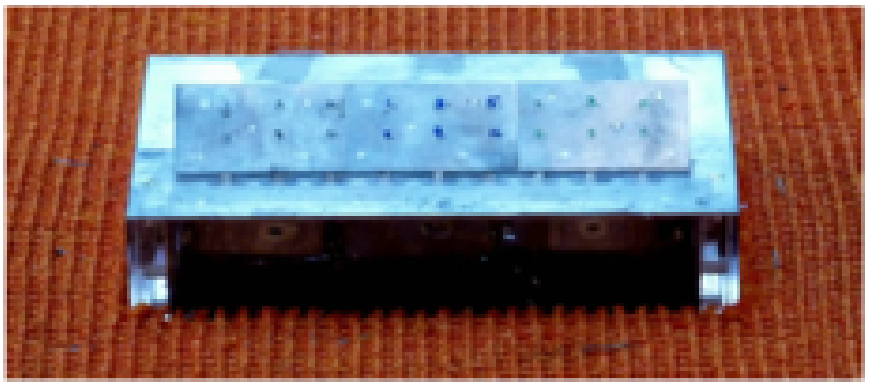

Figure 1. Wind tunnel building and solar panel model.

Figure 31: Stathopoulos wind tunnel test reference [70]

load simultaneously, thereby enabling the potential for load sharing among modules that are structurally connected. Although the concept of load sharing is clear, determination of how many modules actually participate in load sharing is less obvious given the wide array of beam materials (E) and stiffness (I) used to connect modules. Browne proposes a method for determining the number of load sharing modules that may be performed in a simulated or physical experiment. Application of the module and ballast load at each support provides a negative force that resists uplift. Lifting a single module 50mm will engage any load sharing modules resulting in a higher measured force used to perform the lift. Further, the participating modules will also experience lift and have a decreased resultant force at the connection. Once the number of load sharing modules are determined a calculation may be made to determine the ballast required at each module. Based on the results Browne concludes that a significant reduction in ballast weight may be achieved but the actual amount should vary based on the proximity to array edge. Further, Browne points out that this reduction in ballast may actually improve the safety of building occupants by reducing the roof-top live-loads and should not put pedestrians in harms way because during the design wind speed it is impossible for pedestrians to remain on their feet and they have most likely taken shelter [20].

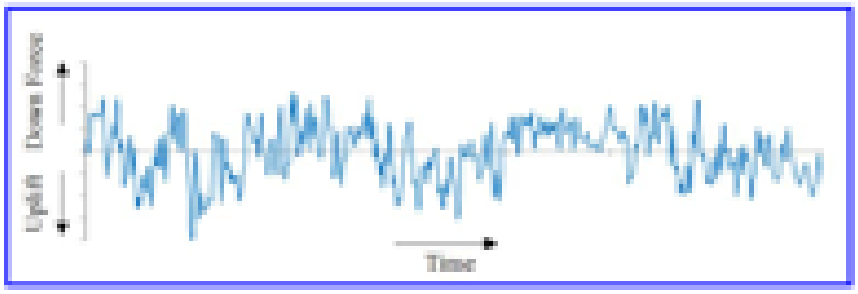

Figure 5. Example Time Series of Measured Pressures.

Figure 32: Sample wind pressure time series [20]

4.1.2 Residential PV system experiments and experimental methods

A full scale experiment was conducted on a residential 42° hipped roof in the Netherlands to determine wind pressures on PV modules. Two individual wooden panels with dimensions 1.6m by 0.8m and 18mm thick were mounted on opposing roof surfaces (Figure 33). Each panel had 3 pressure taps on the top surface and 3 pressure taps on the bottom surface mounted along the centerline. Pressure data was collected for wind speeds greater than 7m/s and analyzed to provide top, bottom and differential (net) pressure coefficients. Pressure coefficients recommended for use in building code are -0.3 for uplift and 0.2 for downward acting loads. These recommendations are only advised for use with a single row of modules in the center of the roof, all other configurations are advised to follow conservative values in NVN 7250 or BRE digest 489. The author recommends further work be conducted to explore actual forces in these configurations [40].

In a continuation of the field study conducted by Geurts and Blackmore [40] additional data was collected and compared against a wind tunnel study of the model scale site. Geurts motivates the work by noting: "The results from [the current body of work] are appropriate for a limited range of roof forms". The results are also assumed to be very conservative, and hence uneconomical in many cases. Also, the authors note the studies available do not cover common installation configurations

Figure 33: Geurts field test reference [40]

(Geurts and Blackmore 2013). The experimental setup utilized the same test roof and modules as Geurts [40] and a 1:100 model scale with 1:200 atmospheric boundary layer scale as shown in Figure 34. The model scale PV module utilized 24 pressure taps disturbed over the top and bottom surfaces, which necessitated a 200mm full scale panel thickness, approximately 3-6 times thicker than a typical panel. The apparatus was rotated every 10° between 180-360° and 30° increments for the remainder. In the analysis, data was screened to omit time series in which the mean pressure difference coefficient was not between -0.3 and 0.3 because this was believed to indicate a likely measurement error due to debris or water in the tubing. Subsequently, an extreme value analysis was conducted on the pressure coefficients to derive values with a 0.02 probability of non-exceedance. The results indicated high sensitivity in lift to the distance from eaves due to the separated flow region along the windward edge. The wind pressure was found to be independent of the gap between the module and roof surface. The wind tunnel experimental data for C_p was found to be conservative compared to full scale values for the 1 second averaging with 20% greater pressure coefficients. Geurts concluded that for cases similar to those tested with a single module away from the edges, design pressure coefficients of +0.4, -0.3 may be used. For system configurations with a larger array of modules, as typically found in U.S. installations, additional testing is recommended [38].

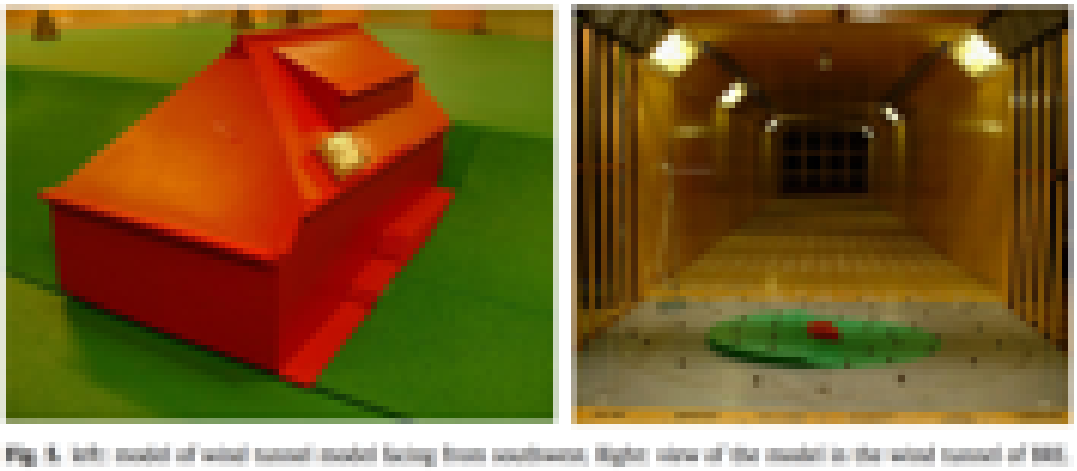

Figure 34: Geurts residential PV module wind tunnel test reference [38]

Erwin et. al. reported on a comparative study of wind loads on PV modules performed both at the FIU wall of wind (WoW) and RWDI boundary layer wind tunnel [34]. The experimental setup utilized a single module mounted on three buildings with roof slopes of 0° 22.6° and 30.2°. The scale at WoW was 1:1 while at RWDI a 1:10 scale was used (Figure 35. Five tilt tangles were tested with the flat roof and two with each of the pitched roofs. Forces were measured with four multi-axis load cells in the full scale test and pressures were measured with 28 pressure taps distributed top and bottom module surfaces. Analysis of the test data translated measurements into 3-second dynamic gust pressures, with 95% probability of non-exceedance. Results of the parallel mounted case indicated less than 5% change in lift pressures between the two pitched roof angles with 0° angle of attack, but a nearly 100% increase in lift was observed from the 30.2° to the 22.6° roof pitches with 180° angle of attack (i.e. module on leeward roof pitch). The cases with the module mounted on an incline relative to roof pitch are more relevant to solar thermal applications and not relevant to the scope of this solar photovoltaic study. For the flat roof, significant pressure changes were observed to occur with varying module inclination angles for all configurations. Further, increases in lift forces were observed between measurements from

WoW and RWDI for flush mounted configurations on all roof pitches. The authors suggest the difference may be due to the mean wind profiles but do not provide a conclusive explanation.

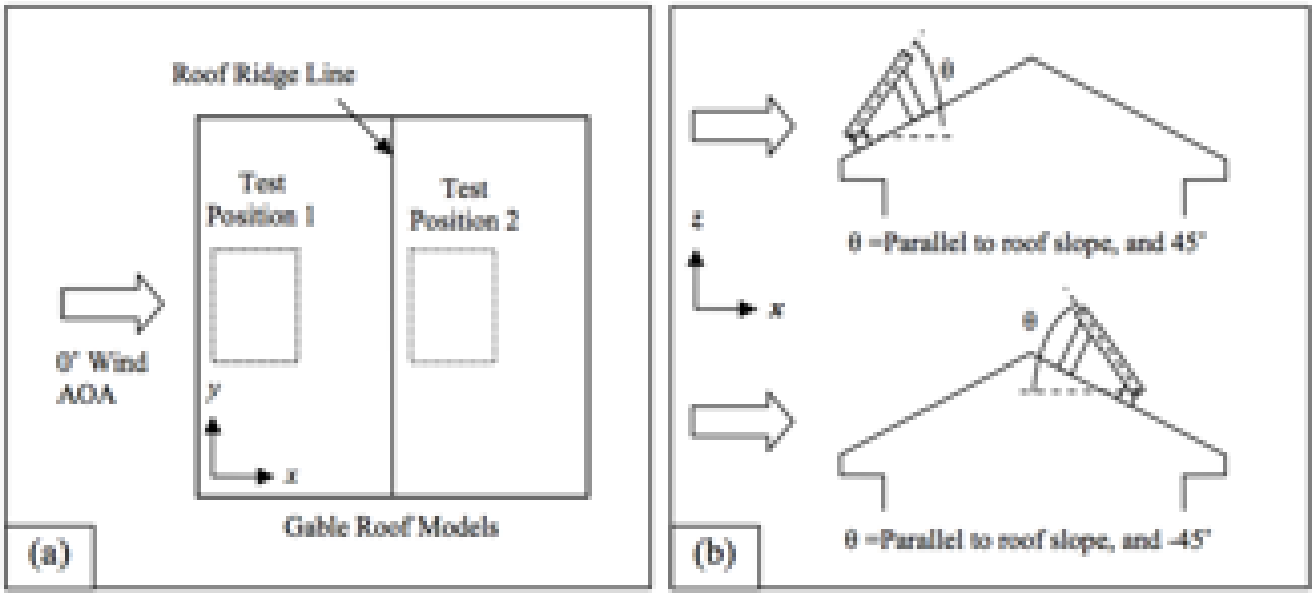

Figure 2. Test setup of a PV panel on the gable roof building models: (a) plan view showing test positions, and (b) elevation view showing PV inclinations.

Figure 35: Erwin test article reference [34]

Motivated by discrepancy in the limited prior residential PV system testing which reported low pressures on PV modules relative to bare roof surfaces for single modules [38] and approximately equivalent pressures for PV arrays compared to roof planes when the PV arrays are modeled as a monolithic plane Stenabaugh [71] studies the effect of array configuration. Alternative configurations were produced by varying the ratio of space between modules, G, and the gap between modules and the roof plane, H. In order to maintain adequate Reynolds number for laminar flow between the module and roof plane, a model scale of 1:20 was used for testing. Stenabaugh noted that choice of model scale prevented simulation of the full atmospheric boundary layer due to missing low frequency content. The proposed solution was to conduct full scale testing to validate results.

The authors proposed adoption of a pressure equalization factor C_{eq} to account for the reduction in net pressure compared to the pressure experienced by a bare roof. Experimental measurements on the configuration with $G = 0$ and $H = 0$ were considered to represent the bare roof condition. Comparison of the bare roof measurements with prior testing at much smaller model scales 1:400 provided "reasonably similar" results. The most significant reduction in C_{eq} was achieved when the module height was between $H = 2cm$ and $H = 4cm$ and larger gaps between modules, G, were found to further reduce C_{eq} up to $G = 12cm$ the maximum value tested. These results allowed the authors to conclude that "gaps between modules are essential for effective pressure equalization" with typical values of $C_{eq} = 0.6$ while the lowest values for a single module were $C_{eq} = 0.2$ [71]. Further when area averaging across multiple modules was considered, an even greater reduction to $C_{eq} = 0.1$ was reported. These results indicate that both G/H and load sharing have significant effects on C_{pnet}.

Fu et al reported on an effort to test residential buildings at model scales between 1:20 and 1:40 using partial turbulence simulation [36]. The work was motivated by a desire to test residential building features such as PV systems which are not easily

reproduced at typical wind tunnel scales of 1:100 and greater. Fu cites a body of literature that establishes small scale turbulence as being approximately equal to the separated shear layer, 1:10 of a low rise buildings height. The small scale turbulence is thought to be primarily responsible for the flow phenomena flow separation and conical vortices. In contrast large scale turbulence is considered to contribute slow moving gusts which may be accounted for in a wind tunnel experiment by post processing the data with an analytical correction of the mean wind speed U by Δ_U. Using procedures reported on by Tu, mean and peak pressure coefficients produced through the partial turbulence simulation method matched well with values produced from full atmospheric boundary layer simulation as shown in Figure 36. The greatest discrepancy occurred in the leeward corner taps with the partial turbulence simulation producing peak pressures with 20% lower values. The author does not suggest which method has greater accuracy but rather concludes that they are comparable. For the purpose of future testing including wind tunnel test conducted as part of this thesis, this article indicates that wind tunnel testing is subject to error at least some of the time, and that the magnitude of error may be 20% or greater in isolated locations. While the spatial resolution of the test was not adequate to extrapolate the results to estimate error when pressures are averaged across a whole module or array of modules, the results do suggest that the error may decrease with tributary area.

Based on further investigation of wind tunnel methods for Small Structures, Mooneghi et. al. [58] reported on an improved approach for matching the high frequency turbulence spectrum in partial turbulence simulations, PTS. PTS was of interest to the authors because of the ability to test small structures with minimal Reynolds number effects, and high measurement resolution. The continued effort was considered necessary because of the mismatch in critical locations hypothesized to occur because of high frequency turbulence intensity mismatch. The authors reference

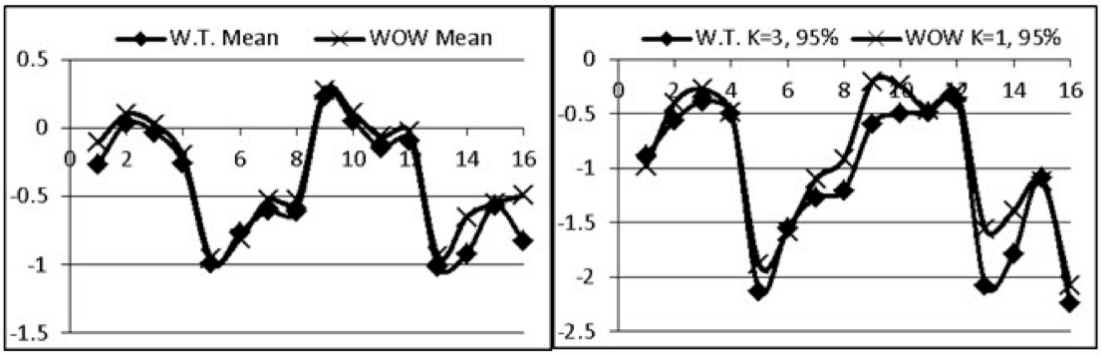

Figure 36: Cp values (y-axis) mean(Left) and peak(right) from partial turbulence simulation and full atmostpheric boundary layer simulation for 16 taps (x-axis) on a gable roof at 45 degree angle of attack [36]

past works which showed high frequency turbulence mismatch effects peak suction pressures, most acutely near the roof corners. As part of the approach, the authors calculate the desired model scale turbulence intensity based on ratios of integral length scale and building dimension. Next the authors calculate an appropriate cut off frequency to separate the high frequency turbulence that is experimentally simulated from the low frequency turbulence that will be analytically incorporated. After the wind tunnel experiment the authors employ a probabilistic approach for determining the mean and peak pressures based on the measured distribution of subinterval pressures along with an assumed Gaussian distribution of the low frequency component defined in Figure 37. Experiments conducted to validate the proposed PTS approach showed improved results especially when the transverse and vertical components of the low frequency turbulence were incorporated. Further, the authors conclude that the method is adequate to allow larger scale models to be tested with PTS and even advantageous when evaluating loads on specific features of residential scale buildings.

4.1.3 Code Application Guidance

Recently, application of ASCE to PV systems has received attention by the structural engineering community and has been criticized as not provid[ing] adequate guidance

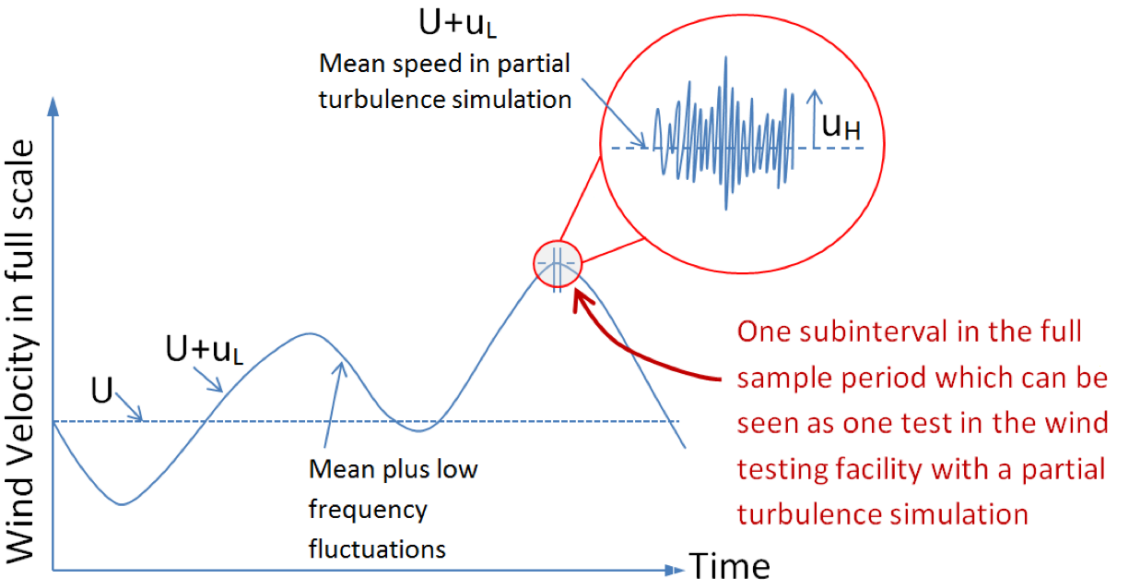

Figure 37: Illustration of subinterval, mean flow velocity, low frequency fluctuations and high frequency fluctuations [58]

to the design professionals and code officials tasked with assessing PV installations" [17]. The authors recommend engineers follow the main wind force resisting system calculation methodology when applying PV modules to a residential roof with a stand-off of 3 to 6 inches. They also recommend wind tunnel testing be conducted for the most common rooftop PV installations to verify methods and calculations and ultimately incorporation of results into codes and standards. In order to execute the recommended MWFRS method, an internal pressure coefficient, GC_{pi} must be selected based on the building enclosure , with an open building have a $GC_{pi} = 0$ and partially enclosed building $GC_{pi} = +/-0.55$. The authors recommend use of a GC_{pi} between +/-0.1 and +/-0.3. To support the recommendation for testing, they discuss that the pressure equalization phenomenon recognized by ASCE to occur with air permeable cladding likely also occurs with PV modules and may reduce wind loads on modules by 50% to 80% or more but they ultimately defer to wind tunnel testing.

In response to inadequacy of ASCE's guidance towards of roof mounted PV systems the structural engineers association of California, SEAOC, issued *Wind Loads*

on Low Profile Solar Photovoltaic Systems on Flat Roofs to bridge the gap between ad-hoc ASCE interpretations and adoption of PV module specific language. Net pressure coefficients are provided for shielded modules that are within a range of allowable configurations and located in either a corner zone, 3, edge zone, 2, interior zone 1 and deep interior, 0 where each zone has a progressively higher pressure coefficient. The depth of the edge zone and corners are equal to twice the building height, based on the size of cornering vortices which only develop to full strength for building widths four times the height. This points out the importance of conducting wind tunnel test with commercial building width at least four times greater than the height. A reduction factor to account for module size is applied to modules with inclination angles greater than 5° to account for array induced turbulence but not less than 5° because of the decreased aerodynamic effect. An edge factor is incorporated to account for the occurrence of flow reattachment when a gap greater than the module characteristic height, h_c, where

$$h_c = 1 + lp * sin(\omega). \tag{44}$$

The edge factor increases linearly between h_c and $8h_c$ after which it remains constant. Guidance for wind tunnel tests per ASCE 7 specifies inclusion of building features that influence flow environment such as varied parapet heights, and other roof top obstructions. It requires an array to be located in each of the roof zones and prevents extrapolation to other module geometries, inclination angles or roof forms. A 50% reduction from prescribed Cp_{net} values is permitted to be attained and an even greater reduction may be used if a third party review of the wind tunnel test report is preformed [77].

Most recently, proposed revisions to ASCE 7-16 have been released by Kopp et al [37]. The proposed revisions incorporate the pressure equalization factors as γ_a to be combined with an array edge factor γ_E. For modules within 1.5 chord lengths from an

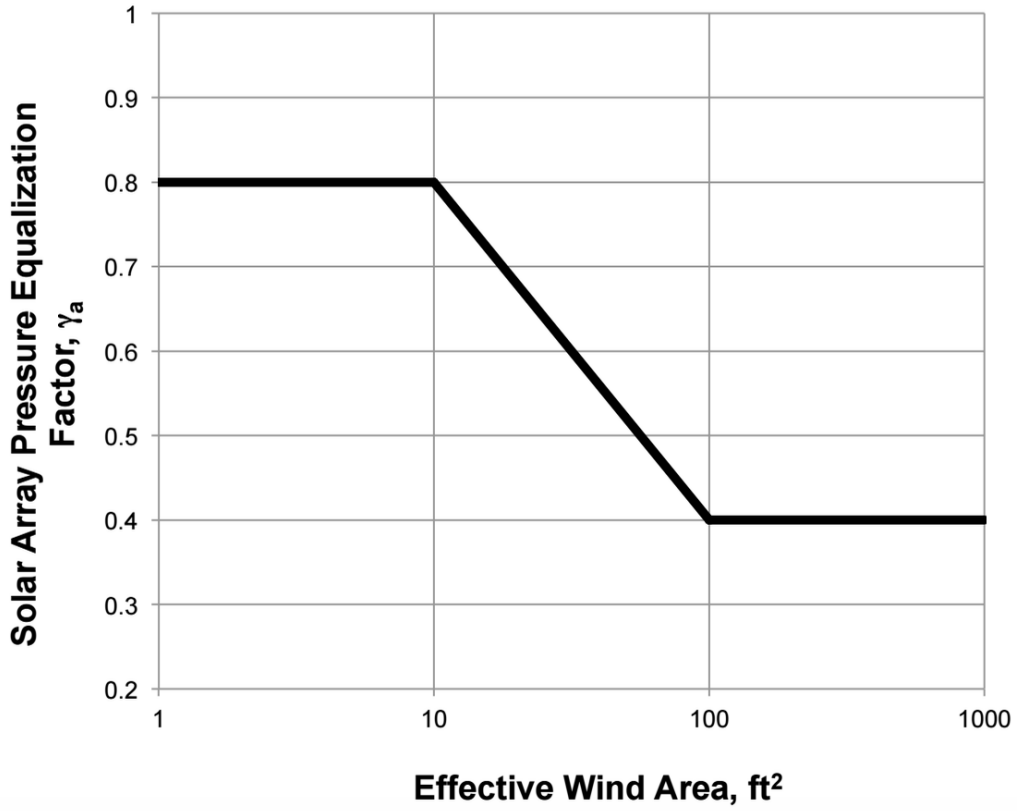

Figure 38: Proposal values for γ_a as a function of tributary area [71]

exposed edge $\gamma_E = 1.5$ and for all interior modules $\gamma_E = 1.0$. As shown in Figure 38 the allowable reduction due to equalization is 0.8 for a single module and 0.4 for a 4x4 configuration that shares loads. These values are 2-4 times the values reported [37] for G/H ratios of 1 because the proposed revision imposes minimal restrictions on G and H and therefore envelopes all allowable cases. Further the proposal recommends that the new equalization factors be used with components and cladding pressure coefficients as shown in Equation 45. The proposal does allow for greater reductions to be achieved through wind tunnel testing.

$$p = q_h(GC_p)(\gamma_E)(\gamma_a) \tag{45}$$

In a separate proposal to revise ASCE 7, Vickery proposed changes to the components and cladding values. Ci‘ting prior research Vickery showed components and

cladding values to be overly conservative for low to moderate roof slopes with low tributary area ($7° \leq \theta \leq 27°$) and for hip roofs with slopes greater than 27°. For example, zone 1 GCp- pressure coefficients are proposed to increase from -0.9 to -2 for tributary area less than $10ft^2$ and decrease from -0.8 to -0.5 for tributary area greater than $100ft^2$. In combination with [37] these two proposals propose a refined approach based on the exclusive use of components and cladding and in combination the proposed values for γ_a and GCp- result in design pressures 8 times greater for components with a $10ft^2$ tributary area than compared to a $100ft^2$ tributary area.

From the available literature, module location [77], load sharing area [20], module tilt and layout [34], [70], [53], roof geometry [77] and wall geometry [16] and most recently array configuration measured by G/H [71] are critical test parameters that have been proven to effect measured wind pressure. Moreover, experimental facilities and analysis techniques have been shown to impact results [34], reinforcing the consensus approach to codification.

4.2 Scale Model Wind Tunnel Experiment

Based on the available literature and ASCE guidelines for wind tunnel testing, [11], [13] wind tunnel testing has been conducted to refine the wind pressure coefficient statistics for the residential PV system design cases under consideration. This section will provide a summary of the test with a focus on reporting experimental conditions as required by ASCE and configuration parameters identified as relevant in the literature. Finally, wind tunnel results for each design case will be presented and used to re-evaluate the fragility curves from Chapter 3 with independent pressure coefficient statistics measured for the design cases under consideration.

4.2.1 Experimental Facility

The wind-tunnel experiment was conducted in the 12 Fan Wall of Wind (WoW) open circuit wind tunnel depicted in Figure 39 and described in detail by Fu[36]. Generally,

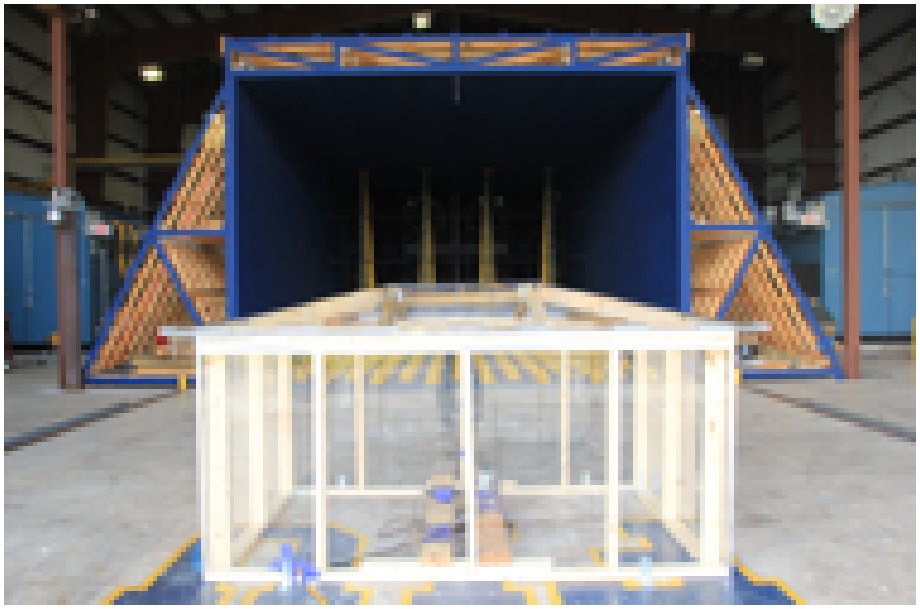

Figure 39: FIU 12 Fan Wall of Wind Tunnel with sample test article mounted on turn table [10].

air is sucked through the 12 fans then contracted to reach the desired wind speed and entering turbulence. Once at speed, the air passes through triangular spires and floor mounted roughness blocks to generate the desired boundary layer characteristics and turbulence.

4.2.2 Experimental Conditions

Wind tunnel experimental conditions for determination of wind pressure coefficients must fulfill prescriptive requirements of ASCE Chapter 6 Section 6: WIND TUNNEL PROCEDURE [11]. The experimental approach for complying with each of the required 7 test condition is described below:

1. Wall of Wind fans, trips and spires were configured and operated to produce a velocity and turbulence profile shown in Figure 40 and 41 consistent with the atmospheric boundary layer.

2. The spires and trips were also configured to generate micro-length scale turbulence matching the atmospheric boundary layer (Figure 42). Marco-length scale

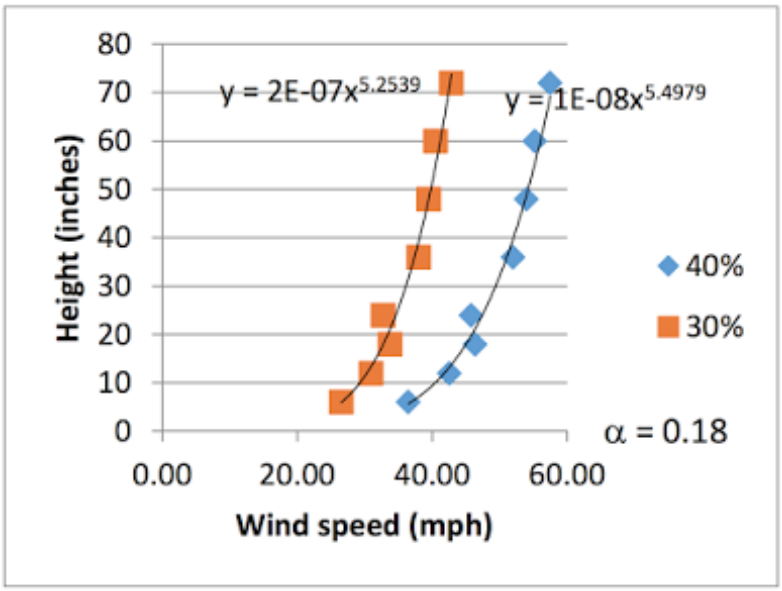

Figure 40: Test Section Wind Speed Profile [10]

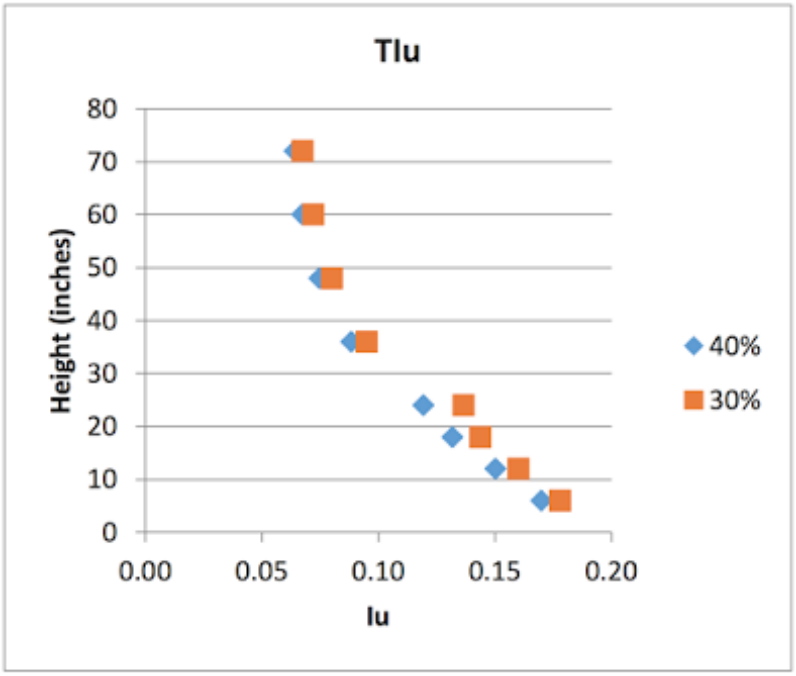

Figure 41: Test Section Turbulence Intensity Profile [10]

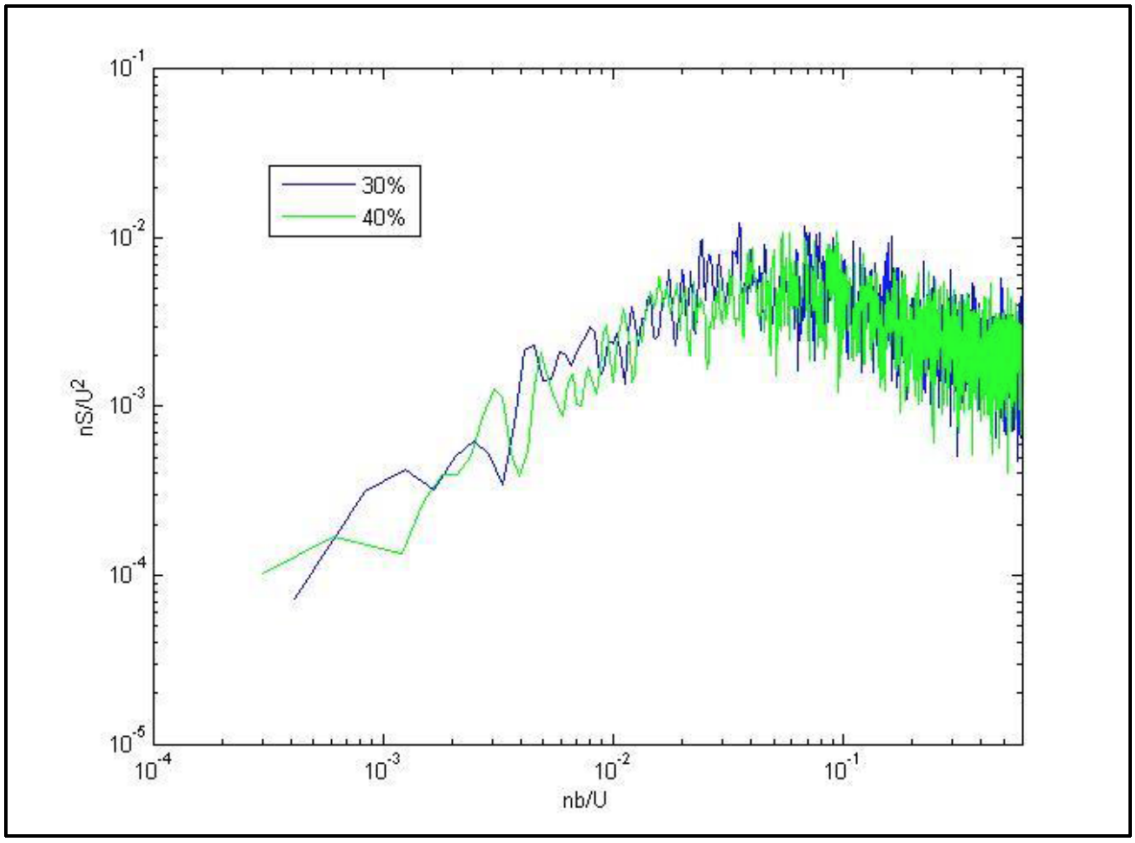

Figure 42: Wall of Wind Power Spectra [10]

turbulence was introduced through post-test linear extrapolation conducted at FIU [10].

3. The residential building and modules were 1:20 scale. The PV module thickness was scaled to typical module frame thickness's and was uniform throughout the module to allow for embedded pressure instrumentation.

4. The maximum model projected area was less than 8% of the wind tunnel cross section for all roof angles.

5. The longitudinal pressure gradients in the WOW were small enough to contribute negligible effects on the test results.

6. Reynolds number effects were minimized through testing at relatively large scale and high enough test speed for Reynolds number independence.

7. 512 simultaneous pressure measurements were collected at 120 Hz and any resonance in the pressure tubing was digitally corrected with FIU's proprietary algorithms [58] to ensure the response characteristics of the pressure measurement instrumentation were consistent with the required measurements.

4.2.3 Wind tunnel test design

Pressure taps on the top and bottom surfaces of the scaled solar modules allowed wind pressures to be measured with electronic pressure transducers connected with tubing to the module manifold. As shown in Figure 43 the 12 pressure taps were evenly distributed across both surfaces for a total of 24 taps and allowed for uniform weighting of measurements. The taps were laser cut through acrylic sheets and connected to the manifold with embossed flow channels sealed by adhering top and bottom layers. Each module was individually checked for flow continuity and leakage. The modules were then attached over the roof surface with a 6" (full-scale) gap. To resist wind loads during testing the module attachment clamp material thickness was 1/8" which corresponded to a 2.5" full scale. This hardware resulted in less than 10% blockage under the modules in the eaves to ridge direction and created a 2.5" full scale gap between modules. The PV module array was configured on a $5x5$ grid with an isolated $1x5$ column of modules followed by an empty column then a $3X5$ sub-array as shown in Figure 44. This layout provided an exposed edge column (left) and partially exposed edge column (right), as well as a partially exposed (center-left) and fully surrounded (center-right) interior columns. Each of these scenarios are common in actual residential PV installations where plumbing vents, or shading result in discontinuities and is considered critical for characterizing the uncertainty of wind loads on modules within the same roof zone. As depicted the array was permanently attached to a roof section that attached to multiple residential building models.

Additional blockage under the modules was created by the module pressure tab

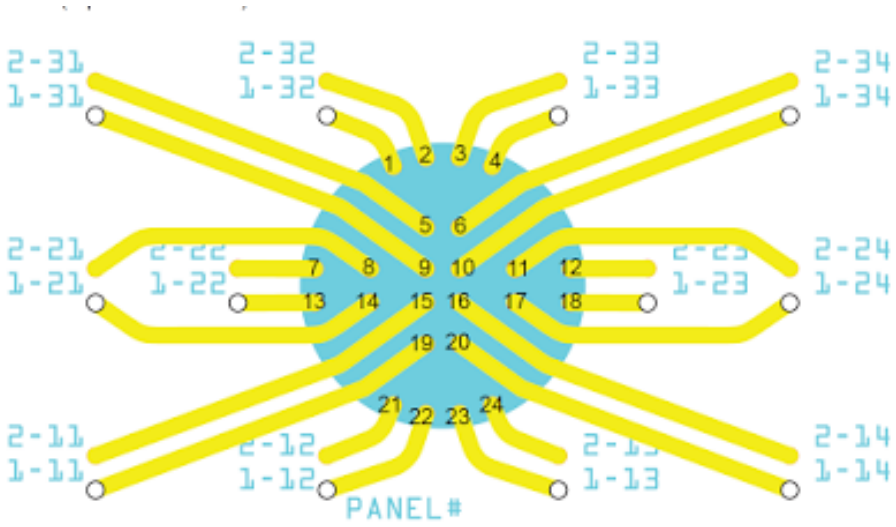

Figure 43: PV module pressure tap layout

tubing bundles attached to the module tube manifold and passing through the roof. The pressure taps were considered to represent a bundle of electrical strings commonly passing from a module back surface into a roof mounted combiner box. An air sealing gasket was used to minimize artificial air flow between the building interior and PV system. A gap between the ridge and top module edge was varied with set values of 6", 21", and 36" (full-scale). To enable the variable ridge offset, the test article roof was detachable from the building so that it can be moved up and down and spacers were inserted to seal the gap. The test article allows for two unique ridge conditions, exposed roof apex and contoured ridge cap. Alternative ridge conditions were used in the experiment to further account for uncertainty in actual scenarios of use due to variation in actual ridge conditions. The construction strategy described necessitated the use of tape during the experiment to seal seams between roof surfaces and wall surfaces. Tape introduced a surface condition that is different from the test article construction but is considered to have small impact on wind induced pressure compared to the building and PV system geometry (Figure 47).

Three residential building models were utilized for testing with three roof pitches

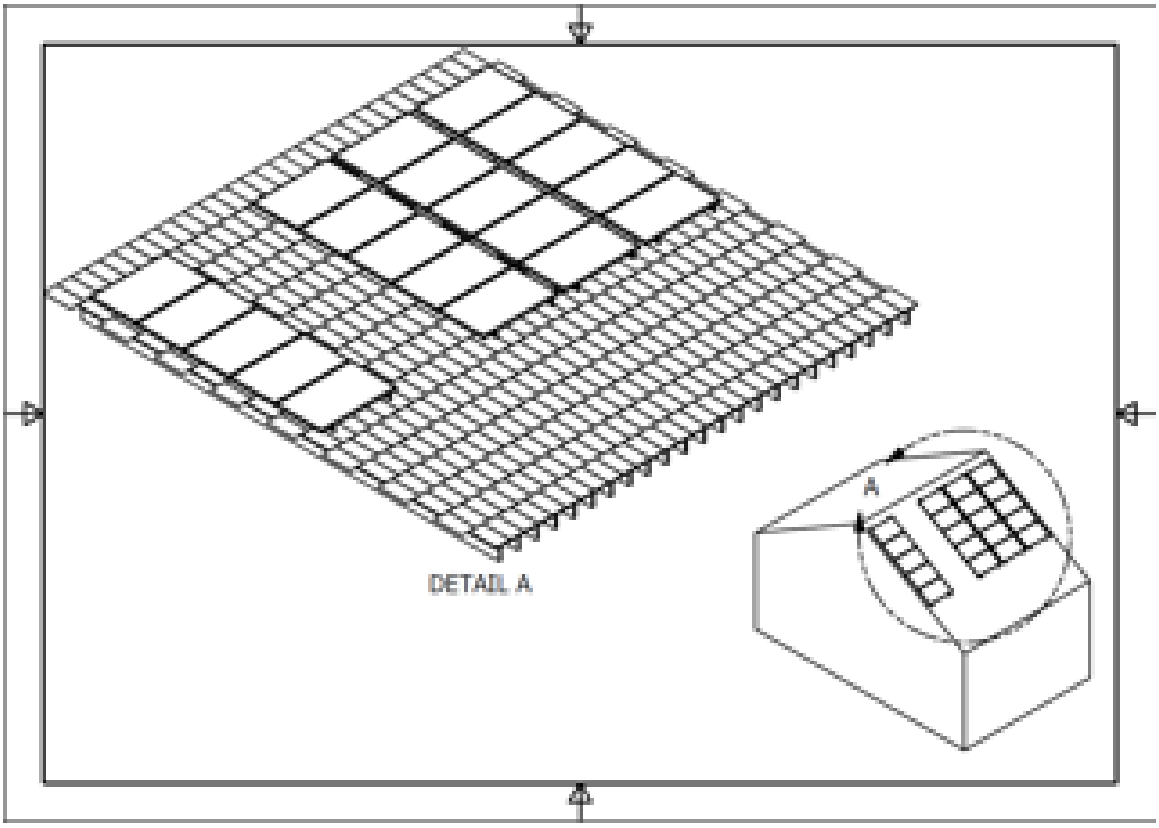

Figure 44: Test Article Array Layout

corresponding to ASCE published tables [11], these include 3 on 12 (15°), 7 on 12 (30°) and 12 on 12 (45°) as illustrated in Figure 45. Due to the importance of wall area [16] [11], the eaves height and E-W length was controlled for by having an instrumented section with equal length that could be added to with modular extensions if needed. Fixed pitch and height necessitated the N-S length to vary between buildings possibly influencing aerodynamic similitude most notably the interaction with the turbulent jet and the re-circulation zone [39].

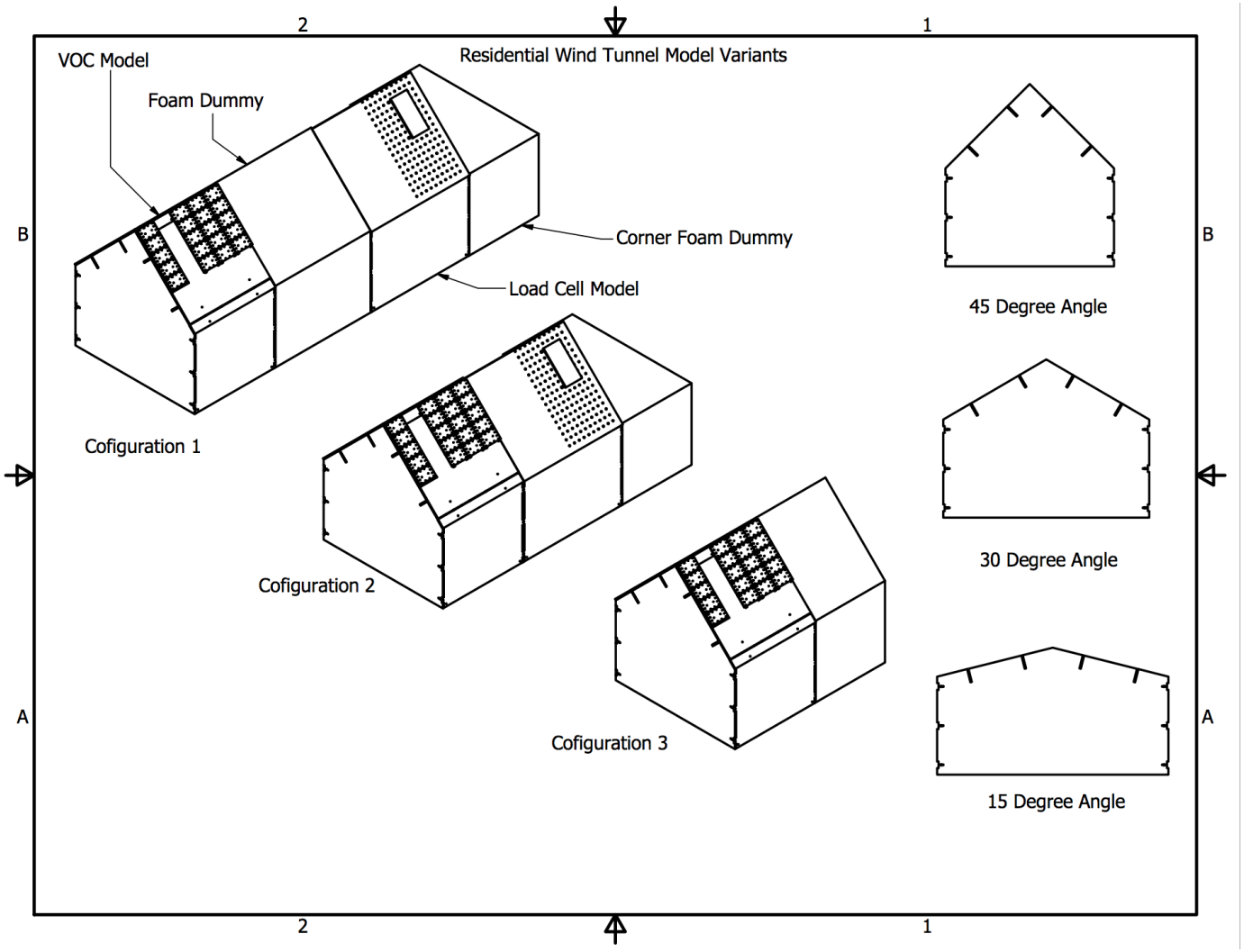

Figure 45: Test article drawings

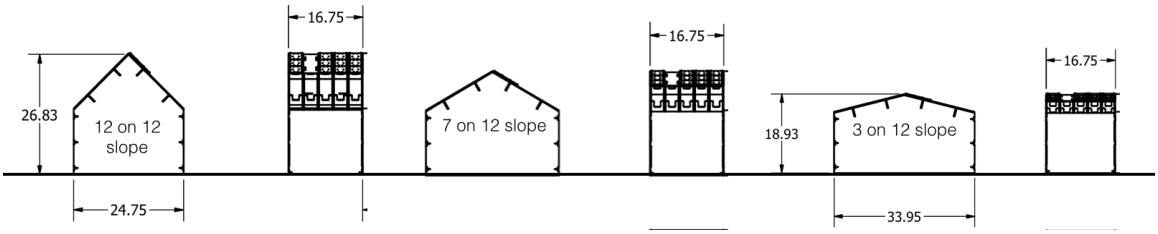

??

4.2.4 Experimental Test Plan

The experimental test plan utilized a hierarchical structure composed of runs, points and experiments. A run constitutes a unique test article configuration described in Table 10, a point corresponds to an angle of attack while an experiment is defined by the data collection period corresponding to a full-scale 3-second gust.

Test article physical parameters varied between runs including ridge condition, roof angle, and ridge offset. A full factorial experiment was utilized with roof angle and ridge offset. Only the 6" ridge offset was tested with the ridge cap installed and not installed as shown in Table 10. The ridge cap was considered most likely to impact modules close to the ridge based on available literature [39].

Each run included 36 points evenly distributed in 10° increments between 0° and 350°. Typically wind tunnel test employ symmetry to reduce the test duration by only testing from 0° to 180°. However, the array layout asymmetry (Figure 44) enabled a unique ASCE zoning from 0° to 180° compared to 180° to 360° when defining the zone based on the leading edge, ridge and eaves and not including the trailing edge as illustrated in Figures 48 and 49 [1]. Zoning diagrams document an aggregation of PV modules analyzed as a 2D system with 15 modules contributing to the 275 square foot influence area. Both ASCE Components and cladding zoning (red lines) and MWFRS zoning (blue lines) are shown.

[1]Statistical analysis using paired T-test was conducted to verify this strategy by comparing wind pressures measured in each zone.

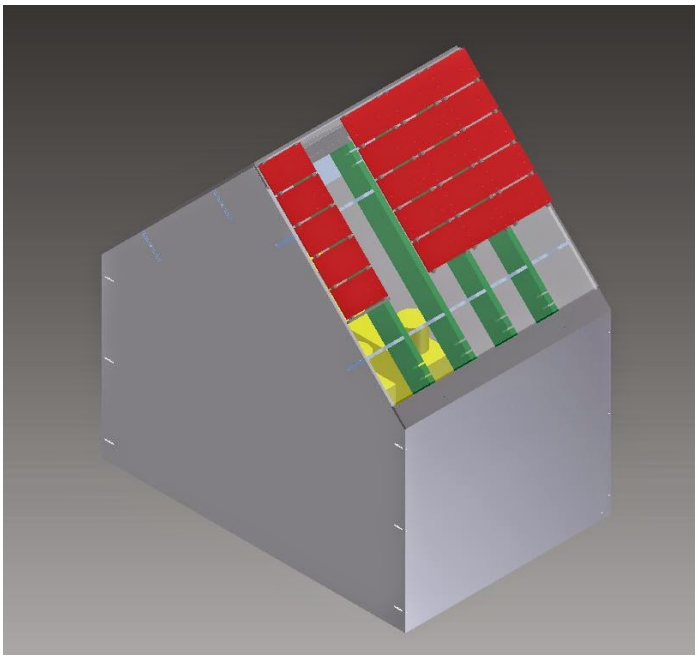

Figure 46: 3D CAD model of the wind tunnel test article with transparent roof surface.

Figure 47: Physical test article installed in the wind tunnel

Table 10: Experimental Configurations

Run #	Ridge Cap	Roof Angle (degrees)	Ridge Offset (in)
201	Not Installed	15	6
202	Installed	15	6
203	Installed	15	21
204	Installed	15	36
205	Not Installed	30	6
206	Installed	30	6
207	Installed	30	21
208	Installed	30	36
209	Not Installed	45	6
210	Installed	45	6
211	Installed	45	21
212	Installed	45	36

For each run and point the test article is in a fixed position for 30 seconds of continuous testing and pressure data collection from each of the 240 pressure taps (24 per module) to comply with ASCE 7-05 31.2 condition 7. Through the time scale t conversion shown in Equation 46 from model scale, $_m$ to full scale, $_p$ an equivalent of 50 scaled 3-second wind gusts experiments were conducted at each point. In total 21,600 experiments were conducted and analyzed.

$$\frac{t_m}{t_p} = \frac{b_m}{b_p}\frac{U_m}{U_p} \tag{46}$$

where T =time scale, b = length scale and U = velocity scale.

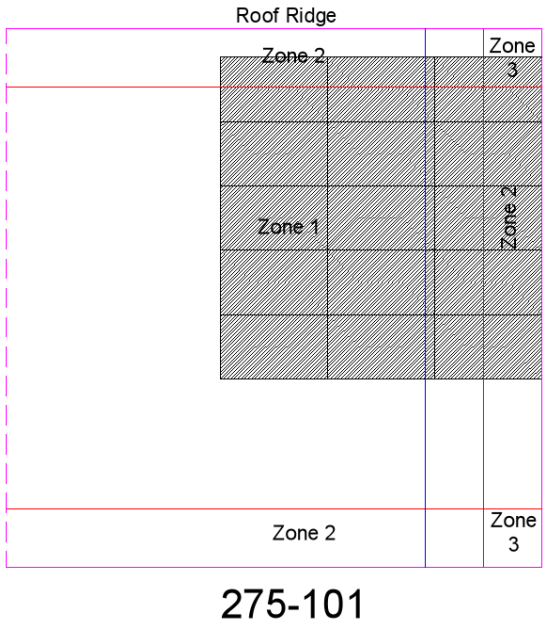

Figure 48: Structural zoning for tributary area, TA = 275 sq.ft., Points 0-180.

4.3 Experimental Data Analysis

The measured tap pressures were analyzed to provide area averaged pressure coefficients for each design case influence area under consideration. This analysis was performed in collaboration with FIU according to the "Partial Turbulence Simulation Methodology For Small Structures" [58]. While the detailed methodology is described by Irwin [58], a summary of the analysis steps follows:

Local top surface and bottom surface pressure time series, $P_{i,net}(t)$ were applied to the local measurement area, A_i and summed for each influence area to generate a net force time series $F(t)$ for each influence area under consideration using Equation 47.

$$F(t) = \sum A_i P_{i,net}(t) \tag{47}$$

Force time series were then converted into net pressure coefficient time series, $Cp_{net}(t)$ using the reference height dynamic pressure, q_{ref}, and influence area, A,

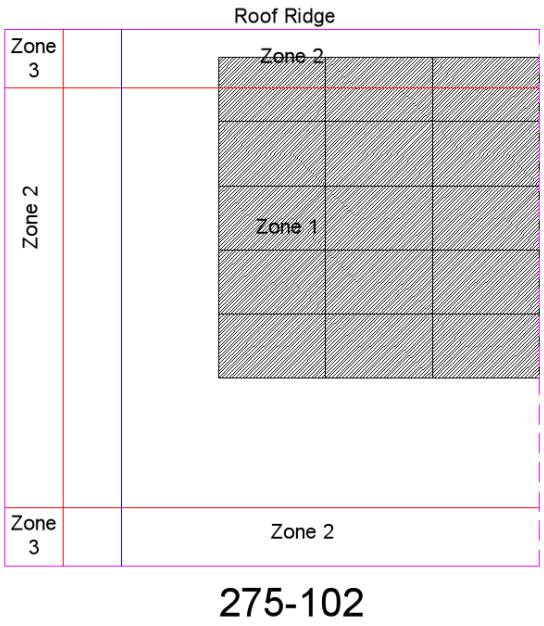

Figure 49: Structural zoning for tributary area, TA = 275 sq.ft., Points 180-350.

$$Cp_{net}(t) = \frac{F(T)}{q_{ref}A} \tag{48}$$

Subsequently, the pressure coefficient time series' for each experiment, was corrected for the macro-scale turbulence not experimentally modeled and analyzed in a WOW algorithm as a Gumbel distribution to determine the most likely, maximum and minimum pressure coefficients, GCn for a 3 second gust [10] as originally described and validated by Mooneghi and Irwin [58]. According to this method and more general wind tunnel testing, GCn is reported with the sign notation illustrated in Figure 8. A maximum pressure coefficient is typically positive and denotes a net pressure towards the roof surface (downforce) while a minimum is typically negative and denotes a pressure away from the roof (Uplift). For some roof angle, wind direction combinations, the maximum and negative are of the same sign indicating only uplift or downforce can be expected for that specific configuration. Figures 50 and 51 graph the maximum and minimum GCp values by wind angle and illustrate two critical conclusions.

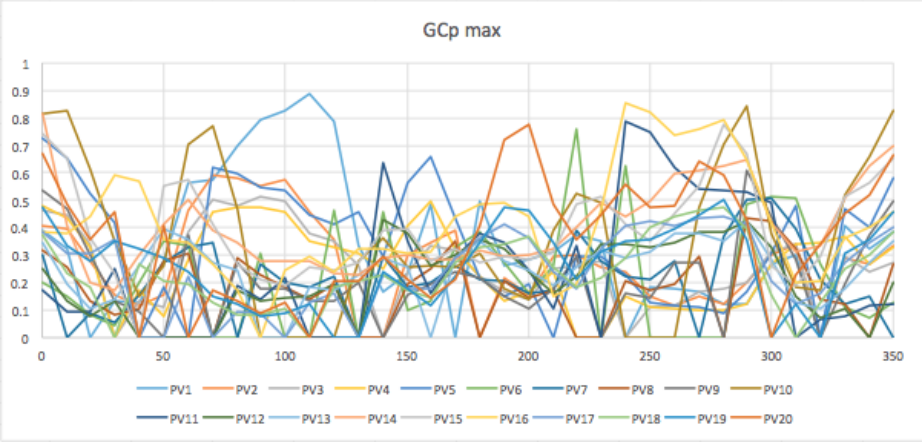

Figure 50: Maximum module GC_p by wind angle

For a fixed wind angle there is significant variation of the maximum and minimum pressure coefficients between modules. The variation is supported by the literature on turbulent vortices that show the high pressure zones of the vortex to have a narrow contact zone with the roof and that the location of the vortex contact zone is sensitive to roof angle [16]. This finding suggests that as multiple modules are aggregated to form a larger influence area, the area averaged pressure coefficients should be significantly below the maximum and minimum local values. Second, the extreme peak maximum and minimum are nearly 3 standard deviations above the mean maximum and minimum indicating the low probability that the peak wind speed direction will coincide with the direction of peak structural response. This effect is addressed by the directionality factor, k_d which has published statistics [33] assumed applicable to residential PV systems. Future work should refine the directionality factor statistics specifically for residential PV systems.

Once a set of maxima and minima for each 10° increment wind direction between 0° and 350° are determined, the sets are divided into two subsets corresponding to 0-180° and 180-350° based on the unique zoning for each subset that supports multiple design cases. Subsequently the subsets are enveloped by selecting the global maximum and minimum to be used in design.

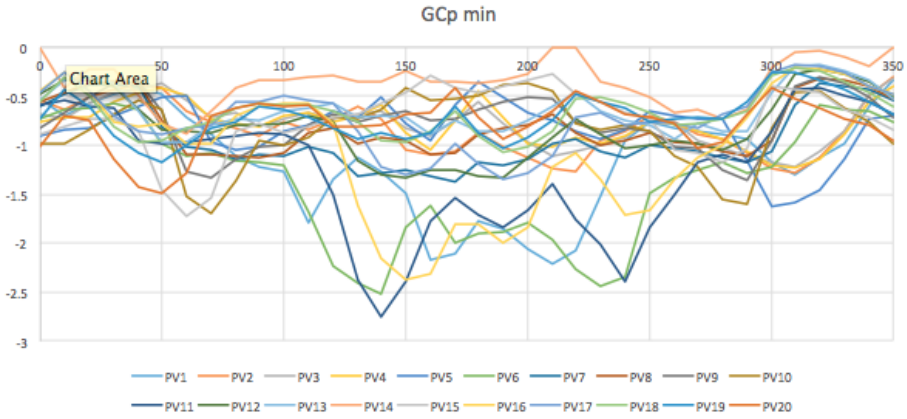

Figure 51: Minimum module GC_p by wind angle

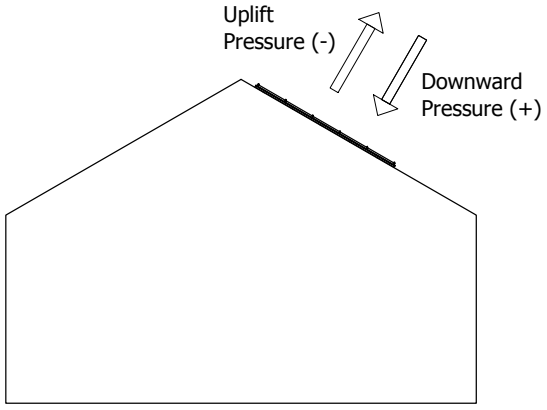

Figure 52: Pressure coefficient sign notation

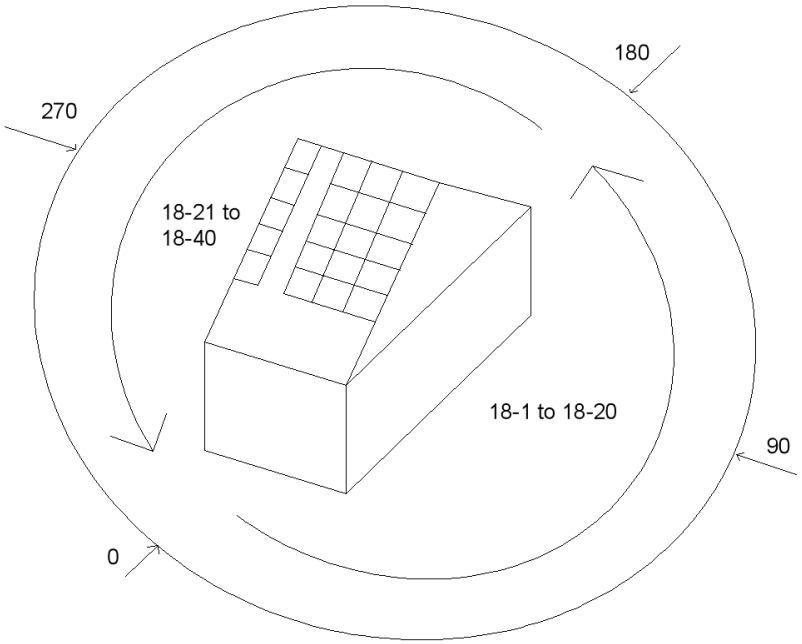

Figure 53: Asymmetric Envelope Approach

The resulting pressure coefficient statistics are assumed to be normally distributed [33] and represented with mean and standard deviation as shown in Figure 54 for the positive pressure coefficients and Figure 55 for the negative pressure coefficients. Both data sets illustrate the single module (18 sq.ft. influence area) have large absolute mean values and standard deviations compared to aggregations of modules with influence of 90, 180, 270 sq. ft for all roof angles. These results are consistent with the variation observed in Figures 50 and 51 along with the rational for the components and cladding approach [11].

Table 11: Wind Tunnel GCp+ statistics

	15 Degree		30 Degree		45 Degree	
	Mean	St. Dev.	Mean	St. Dev.	Mean	St. Dev.
180-101	0.14	0.010	0.32	0.038	0.53	0.010
180-102	0.17	0.027	0.28	0.068	0.42	0.068
18-101	0.49	0.159	0.49	0.087	0.82	0.115
18-102	0.50	0.159	0.58	0.104	0.81	0.116
18-103	0.60	0.155	0.59	0.178	0.66	0.115
18-104	0.58	0.162	0.53	0.111	0.60	0.088
270-1	0.12	0.029	0.30	0.033	0.49	0.022
270-2	0.11	0.019	0.22	0.028	0.36	0.026
90-101	0.26	0.038	0.42	0.048	0.62	0.032
90-102	0.25	0.050	0.31	0.042	0.44	0.065

Table 12: Wind Tunnel GCp- statistics

	15 Degree		30 Degree		45 Degree	
	Mean	St. Dev.	Mean	St. Dev	Mean	St. Dev
180-101	-0.67	0.10	-0.54	0.03	-0.43	0.02
180-102	-0.57	0.12	-0.53	0.09	-0.43	0.06
18-101	-1.82	0.29	-1.05	0.19	-1.03	0.08
18-102	-1.36	0.23	-0.97	0.07	-0.86	0.13
18-103	-1.54	0.53	-1.10	0.14	-1.00	0.10
18-104	-1.10	0.26	-0.98	0.22	-0.88	0.16
270-1	-0.60	0.13	-0.48	0.02	-0.42	0.02
270-2	-0.48	0.11	-0.42	0.02	-0.35	0.01
90-101	-1.05	0.08	-0.73	0.06	-0.63	0.08
90-102	-0.73	0.14	-0.66	0.11	-0.57	0.09

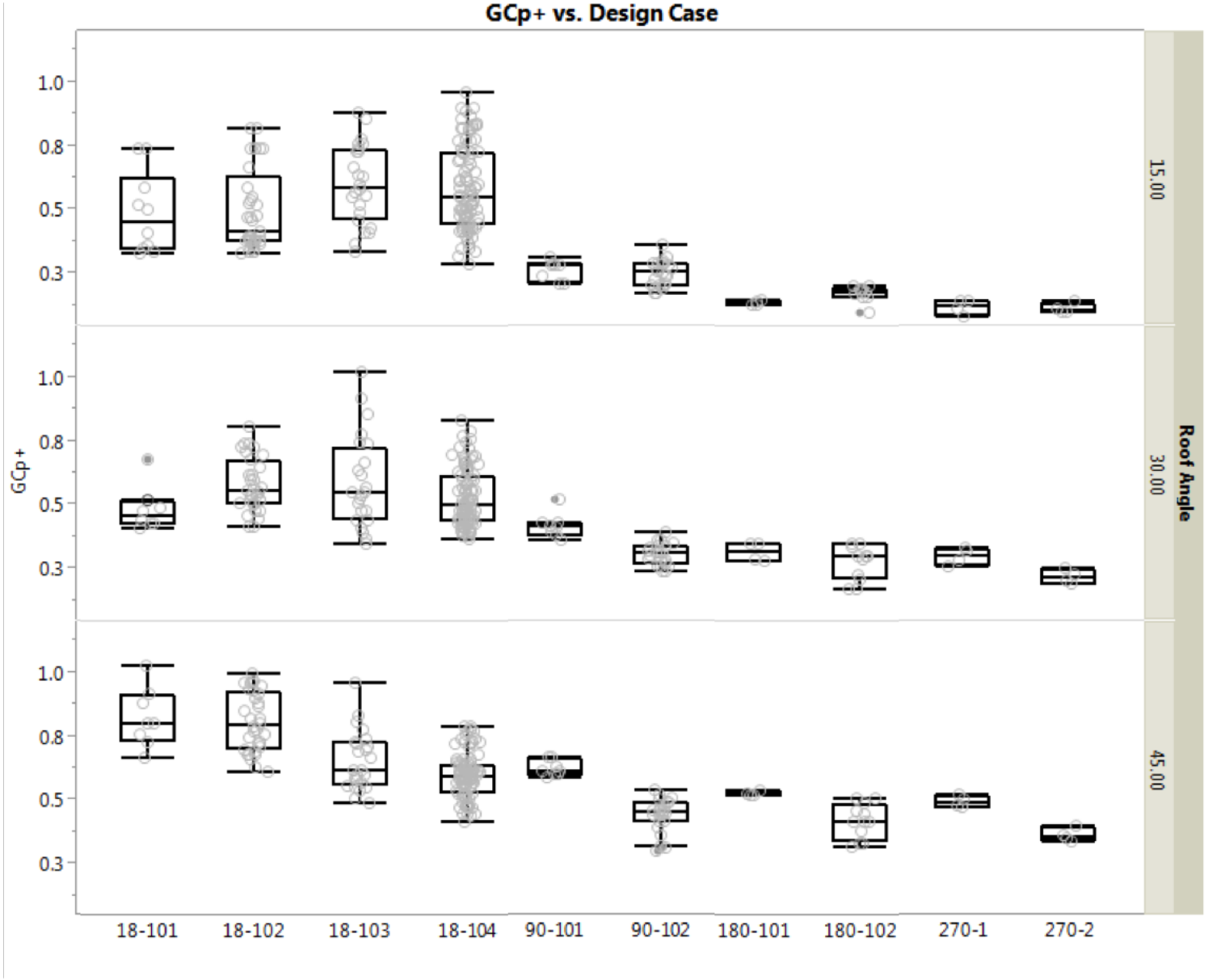

Figure 54: Mean and standard deviation GC_p+ statistics by design case and roof angle

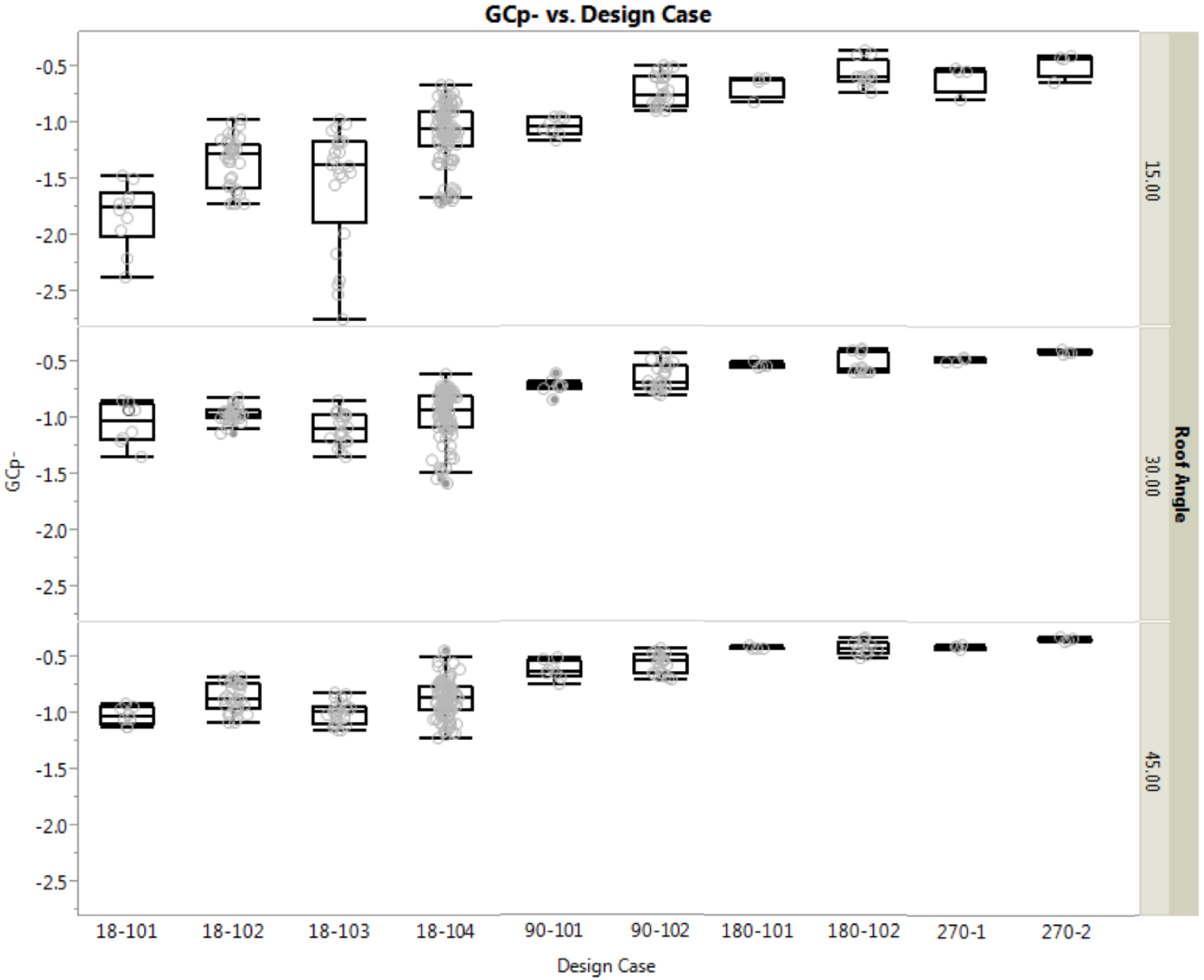

Figure 55: Mean and standard deviation GC_p- statistics by design case and roof angle

4.3.1 Case study fragility curves

In the last section the experimentally measured pressure coefficients were shown to be statistically different than the code prescribed values. this section will examine the the effect on structural performance through revised fragility curves. The importance of utilizing pressure coefficients measured from wind tunnel tests on residential PV systems is tested through the following hypothesis.

Hypothesis Fragility curves developed with experimentally derived wind load statistics will suggests significantly different performance compared to fragility curves based on current code prescribed values.

Sub-Hypothesis Application of state of the art design guidance [17] to the divergent system types results in non-uniform performance measures.

Revision of the case study fragility curves with the wind tunnel derived pressure coefficient statistics results in the updated fragility curves in Figures 56, 57 and 58. The only change in the revised curves is the replacement of the delphi's pressure coefficient statistics with the experimentally derived statistics. In each Figure, design cases with increased risk outcomes relative to ASCE derived curves are illustrated with dashed lines while those with decreased risk outcomes are illustrated with sold lines. For the 15° roof, each of the 0-D design cases experienced an increase in risk with the probability of failure going from 50% at 130mph to over 80%. Conversely, the 1-D and 2-D design cases experienced a decrease in risk with 2-D cases dropping from 50% probability of failure at 130mph to less than 10%. The Fragility curves for the 30° and 45° illustrate the trend that as the roof slope increase an ASCE design PV system becomes more likely to have a LS#1 failure. In the 45° case each system is more likely to experience a LS#1 failure during a wind speed gust with V between 90 and 150 mph compared to what ASCE code values suggest. Also there is a significant difference in the probabilities of failure between system types given occurrence of a 3-second gust in the specified range.

For both the hypothesis and sub-hypothesis, the results allow rejection of the null-hypothesis. Based on these results, wind tunnel testing of residential PV systems appears necessary to accurately quantify the structural performance risk of a code engineered system.

Further, the results provide motivation for an improved approach to risk management in future code revisions. One approach could be to increase the uncertainty in the wind load statistics so that the diverse system types fall within the distribution. This approach is not recommended because some system types would be significantly over-engineered. Another approach is to update the wind pressure statistics for residential solar PV by conducting additional experimentation at multiple facilities to develop regression models similar to those published in the SEAOC guidance. When planning this approach the literature suggest wind tunnel facilities should be selected to include multiple testing and analysis methods including smaller scale facilities to model the complete boundary layer and full scale facilities to quantify testing error. Given the solar industries high sensitivity to cost, this path is preferable since it provides for right sized systems with quantifiable structural performance.

Finally, the results for wind speeds $V \leq 70$ mph and $V \geq 170$ mph should be considered. In each of these ranges, the LS#1 reliability performance is equivalent, with near 0 likelihood of failure for $V \leq 70$ mph and near certain failure for $V \geq 170$ when installed on a 45° roof. A logical question is which of the wind speed ranges matters for a system with 25 year design service life. This question is addressed in Chapter 5 by developing a coupled reliability model through incorporation of an extreme wind speed model.

h

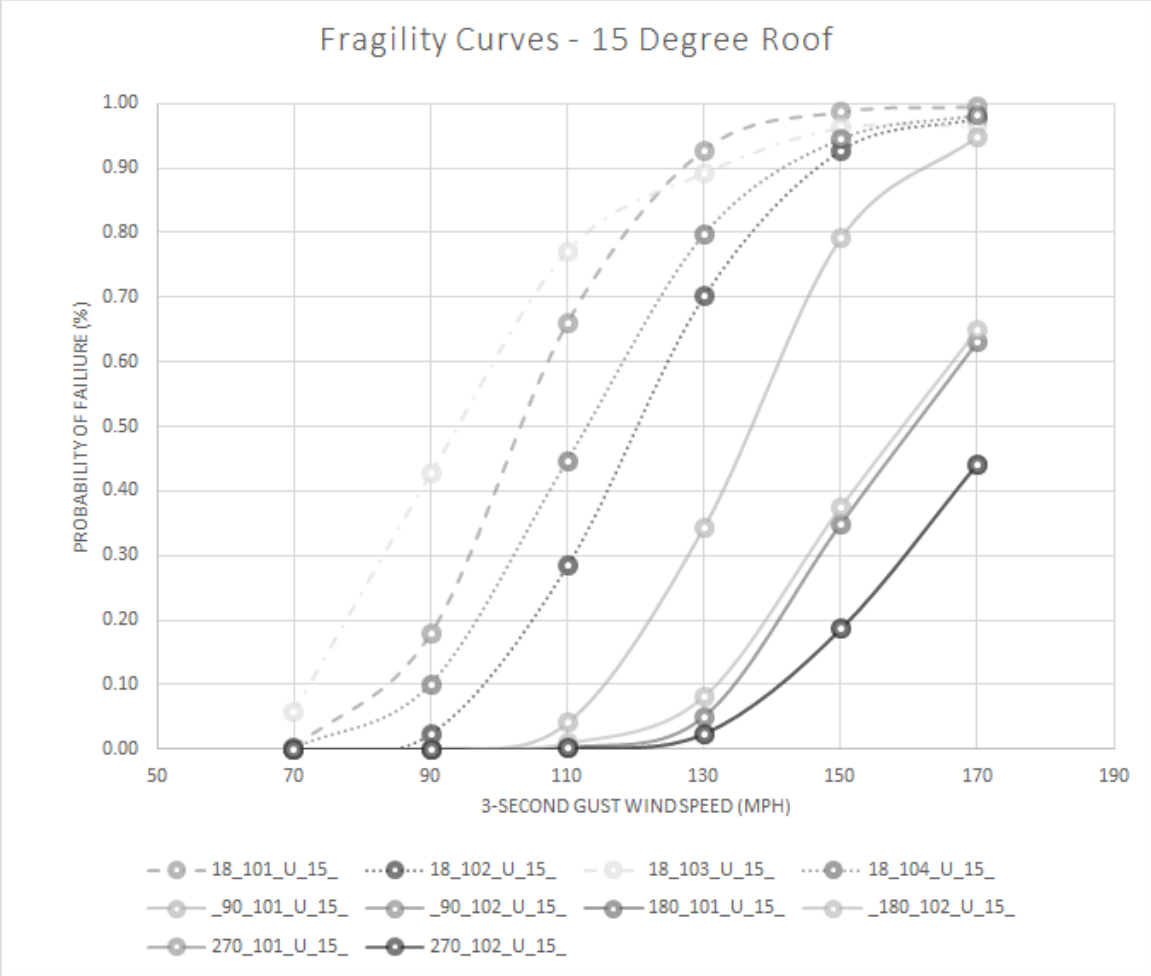

Figure 56: Fragility curves for 15 deg roof

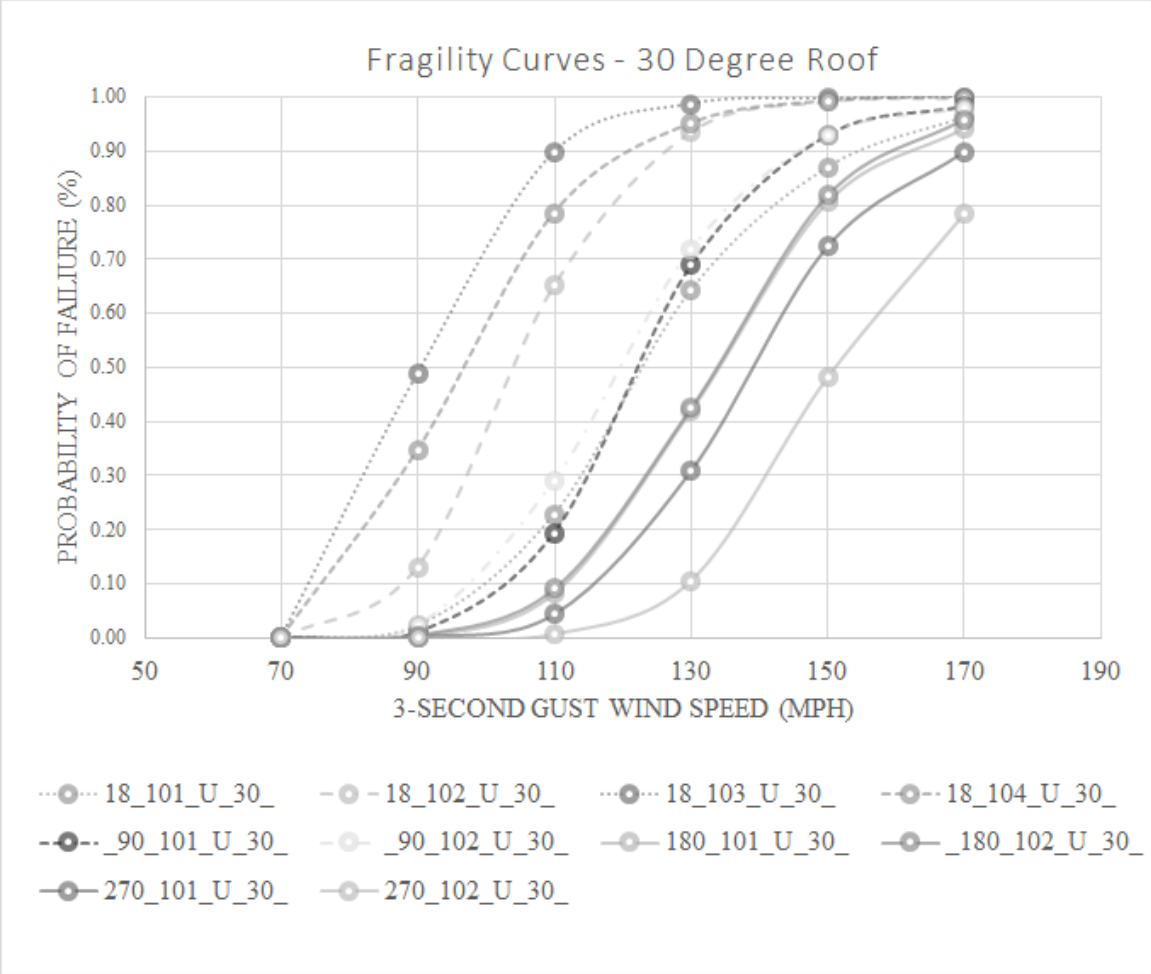

Figure 57: Fragility curves for 30 deg roof

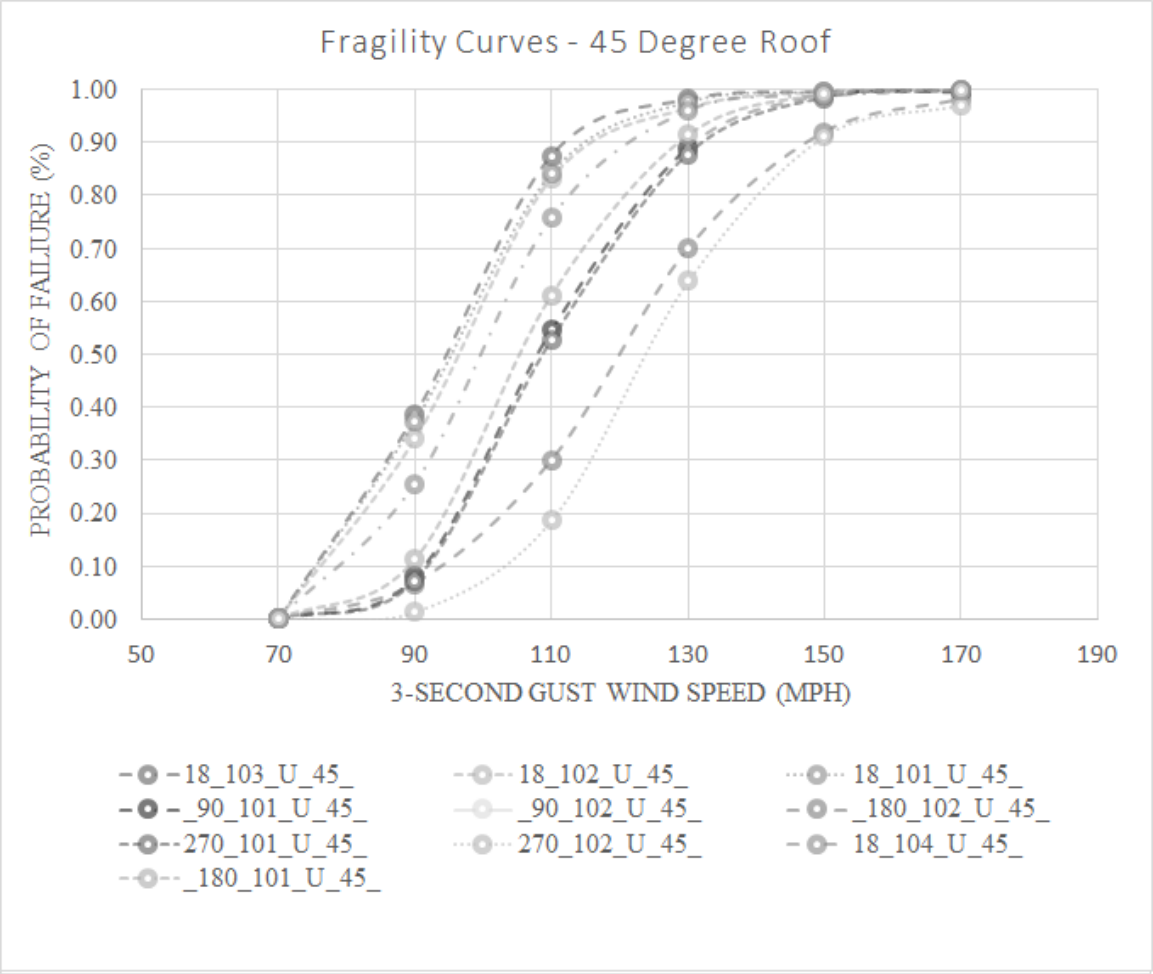

Figure 58: Fragility curves for 45 deg roof

CHAPTER V

COUPLED RELIABILITY MODEL

Chapter 4 presented the process and effects of reducing epistemic error in wind pressure coefficients through incorporation of wind pressure coefficient statistics measured in a residential PV system wind tunnel experiment. Chapter 4 also demonstrated application of the measured pressure coefficients to the case study fragility models. The fragility models indicated a significant effects on the probability of failure over a range of wind speeds. This chapter will address the yet unanswered question of how to consider a set of failure probabilities conditioned to wind speeds given historical wind speeds and required service life. This question is answered through application of a reliability performance measure for code engineered PV systems that couples the probabilistic structural analysis with a probabilistic extreme wind speed model. Ultimately, this chapter in conjunction with Chapter 3 will show that the fragility analysis and reliability analysis may be conducted in two distinct steps. First the fragility analysis may be conducted for a specific technology and defined scenario of use as demonstrated in Chap 3. Then the fragility analysis can be coupled to a site specific wind speed model to provide a site specific reliability performance measure.

5.1 Background

To support the development of a coupled reliability model for residential PV systems, background on wind speed modeling and uncertainty will be provided.

5.2 Probabilistic models for 3-second gust

Significant efforts have been completed to develop mathematical models of maximum annual wind speed for a location of interest based on limited historical data. In the

analysis of historical data sets, daily maximum wind speeds compose an annual set which is typically well characterized by the general Weibull or special case, Raleigh distribution [66]. Weibull distributions have been used to conduct fatigue analysis [56]. However, the short spans of residential PV system structural rails tend to be treated as rigid structures with fundamental frequency above 1hz according to Equation 49 [11].

$$\omega = (\frac{\pi}{L})^2(\frac{EI}{\rho_m A})^{\frac{1}{2}} \tag{49}$$

When fatigue is not a design constraint and the yield stress governs, extreme loads are of interest, which are not well characterized by Weibull distributions [66]. Methods for the mathematical modeling of a set of maximums or minimums are described by Extreme Value Theory [8]. Application of extreme value theory to wind loads has been completed for tornado, hurricane, thunderstorms and mixed sources [63]. A focus of current extreme value research is on the accurate shape of the distribution's tale. This is particularly relevant to reliability assessments with low probability of failure. The Type 1 extreme value distribution, also known as the Gumbel distribution, has a CDF given by Equation 50 and has been recognized as a best fit for extreme wind speeds [66].

$$F(x) = e^{-e^{-(x-\mu)/\beta}} \tag{50}$$

Where β = the Gumbel shape parameter and μ = the scale parameter.

5.2.1 Parameter estimation

Alternative methods and software [45] are available for the estimation of maximum annual wind speeds based on historical data. The method of moments shown in Equation 51 has been shown to accurately predict a wind speed V_N with recurrence interval N measured in years. This method has been used with weather data from

single stations and more recently from superstation weather series[1] data [62].

$$V_N = V_{mean} + 0.78(lnN - 0.577)SD \tag{51}$$

Where

V_{mean} is the sample mean wind speed in mph

N is the recurrence interval in years for wind speed V_N

SD is the sample standard deviation

The method of moments is valuable for setting a design wind speed based on a specified recurrence interval, but does not support stochastic modeling of annual maximum wind speeds. Alternatively, a graphical method has also been shown to produce accurate parameter fits for the Gumbel distribution. The graphical method for Gumbel parameter estimation utilizes the linear fit of a probability plot with wind speed plotted against ordered sample count. In the graphical method, the Gumbel shape parameter, β is estimated with the Y intercept and the scale parameter, μ is estimated with the slope [8]. The graphical fitting methodology will be demonstrated in the case study.

5.2.2 Model statistical uncertainty

Development of mathematical models for extreme wind speeds relies on historical records with limited length and accuracy. Up until the 1993 ASCE wind maps, wind speeds utilized the fastest mile measurement collected from 129 airport stations with 10-50 years of operation. A switch to peak gust wind speed maps was motivated by the obsolescence of fastest mile sensors and prevalence of peak gust sensors. BY 1988 487 National CLimatic Data Centers (NCDC) stations were operating with 5-45 years of data. The limited operating history of both fastest mile and peak gust stations is

[1]Superstations, are aggregations of weather-years from regional stations proven to have statistically independent but belonging to the same parent distribution[62]

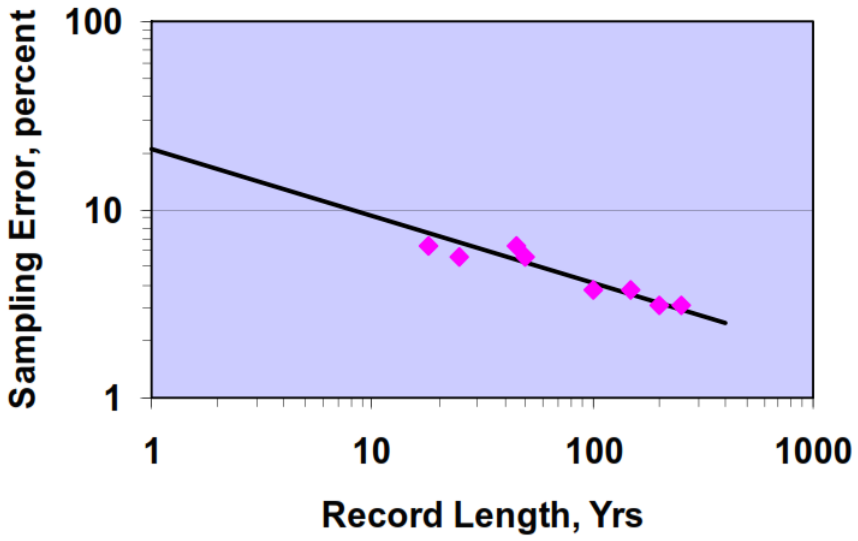

Figure 59: Sampling error standard deviation vs sample size adapted from CPP [63]

the primary source of sampling error. A quantification of sampling error is provided by the standard deviation of sample means $SD(V_N)$ given in Equation 52 [62].

$$SD(V_N) = 0.78(1.64 + 1.46(ln(N - 0.577)) + 1.1(ln(N - 0.577^2))^{\frac{1}{2}} S/n^{\frac{1}{2}} \qquad (52)$$

Where n is the sample size (years of record).

As shown in Figure 59 the effect of sample size on sampling error from typical weather station records with less than 100 years of data is between 5% and 10% or approximately 5 mph. Aggregation of large data sets through super-stations reduces sampling error to approximately 3% [63].

5.3 Application to residential PV systems

Investigation of extreme wind speed modeling methods for renewable energy applications has been principally focused on wind power applications. Investigations of wind speed modeling for solar power have not been identified through literature review conducted as part of this thesis. A primary reason for this gap in effort is the extreme wind speed is by definition a reference wind speed at 10 meters above ground. The

extreme wind speed is not affected by the building structure nor the presence of a PV system but rather the surrounding environment. The building structure and other site specific contextual variables influence the dynamic pressure calculation, wind speed is an input into the the dynamic pressure calculations along with variables that account for these contextual factors. For this reason, the body of knowledge characterizing extreme wind speed distributions is considered adequate for the evaluation of residential PV systems.

Current codified design practice condenses the wind speed distribution into a single design wind speed based on a recurrence interval [11]. In order to evaluate the reliability of a design engineered to code a more exact method is needed. Therefore, the proposed performance measure is based on Monte Carlo simulation to select a wind speed from the Gumbel probability distribution function for each sample, n, in an experiment. This approach should lead to the benefits identified in the following hypothesis.

Hypothesis: A coupled reliability model provides a platform for combining structural risk with stochastic wind speeds for a single reliability measure.

Sub-Hypothesis: A coupled reliability model provides a platform for comparing alternative system types given a stochastic model for extreme wind speeds.

Sub-Hypothesis: A coupled reliability model has the capability to assess if a code engineered system is under-engineered or over-engineered compared to independent reliability targets.

This Hypothesis is distinct from the fragility hypothesis because the latter hypothesized capability to make comparison at a particular wind speed and the former proposes comparison given a wind speed model applicable to a geographic location. Evaluation of the hypothesis will be conducted through this chapter's case study.

5.4 Case study

This section of the case study demonstrates coupling of an extreme wind speed model with a fragility model to provide a site specific reliability performance measure.

For the case study location, Atlanta GA, 42 years of extreme 3-second wind speeds are avail able from NIST [8]. The 42 year data set has a mean value of 59 mph, and maximum value of 90 mph. Utilization of the linear fit approach [8] produces a Gumbel distribution with location, $\mu = 54.1$ and scale, $\beta = 8.6$. The linear fit shown Figure 60 has an $R^2 = 0.98$. Using Equation 50 to the define the CDF of V (Equation 53) allows determination of an N year wind speed V_N. The 50 year wind speed V_50 with 2% likelihood of exceedance is found to equal 88mph. Given the sampling error of the 42 year data set, this is statistically similar to the ASCE 90 mph wind zone for Atlanta.

$$F(V) = exp(-e^{(x-\mu)}/\beta) \tag{53}$$

To execute the Monte Carlo method a random number generator was used to produce a synthetic 1000 year set of extreme gust from the Gumbel distribution. The synthetic set of extreme values, was found to be statistically similar to the 42 year historical data set. Figure 61 of the synthetic set shows the probability of exceedance for a 90mph gust to be 1%.

Coupling the fragility model with the wind distribution, represented by the synthetic wind data, produces a reliability model capable of estimating annual survival probabilities. This is achieved through repetition of 1000 samples in a Monte Carlo experiment where for each sample the random variables distributions are sampled to generate unique values of wind speed V, wind pressure Q, moment demand, M_d and actual moment M_a. Using these random variables, the limit state function is evaluated for each sample with the outcome equal to failure or survival. The annual probability of failure P_f is then calculated by dividing the number of samples that

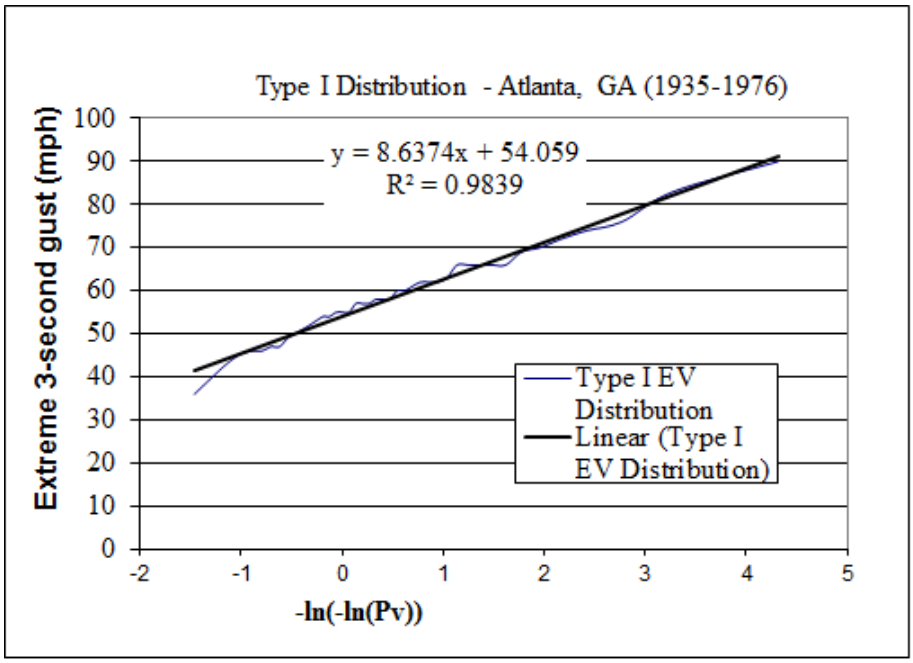

Figure 60: Gumbel theoretical vs empirical quartiles plot of Atlanta extreme 3-second gust

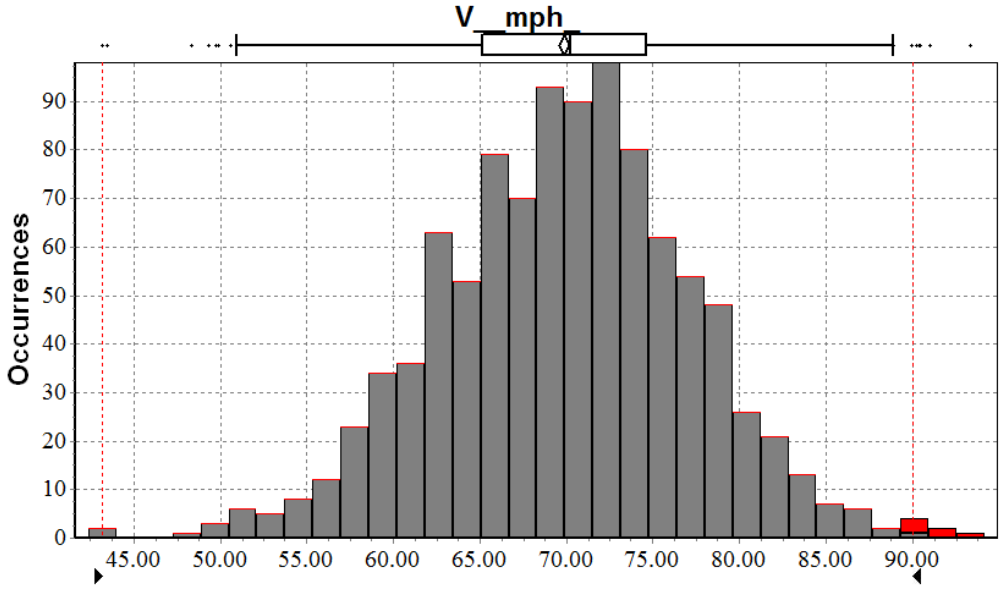

Figure 61: Frequency plot of Synthetic set of extreme wind speeds for Atlanta (n=1000)

resulted in a failure by the total number of samples. Finally P_f is used in the binomial distribution shown in Equation 54 to predict the probability of failure in 25 years $P_f(25)$ by defining that a 25 year survival requires exactly 0 failures.

$$P_f(x) = \frac{n!}{x!(n-x)!} p_f^x (1-p_f)^{(n-x)} \tag{54}$$

where x = the number of failures n = the operating life in years p = the probability of failure

Similarly, the survival probability may be calculated for other periods. This approach assumes that the system is either operating with similar strength to its original installation condition or that the system has an ultimate failure. This approach does not allow for structural degradation due to fatigue from non-catastrophic wind events. For failure modes that are susceptible to partial degradation, incorporation of discrete event simulation into the reliability analysis has proven to adequately model degradation events leading to partial strength operation [47].

5.4.1 Case study reliability results

An experiment using the coupled reliability model was conducted for each of the ten design case applied to three roof angles; 15°, 30° and 45° for 30 total experiments. Each experiment consisted of 1000 Monte Carlo samples. Using the 1000 samples from each experiment, an experimental standard deviation for $G(X)$ was found to range from 0.006 to 0.3 over the 30 experiments. With standard deviations in this range and sample size = 1000 the model uncertainty given by Equation is estimated to be less than 0.01.

Table 13 summarizes the results from each of 30 experiments with a 1 year and 25 year probability of survival reported to the thousandths decimal. More specifically, the results may be interpreted as a structural reliability quantification of code designed PV racking design cases, using the high fidelity ("exact") Monte Carlo method.

The reliability reported is only in regard LS #1 and does not quantify the likelihood of failure due to other structural failure modes for which the proposed method may be repeated.

The results indicate the 1 year survival probability for code engineered 0-D design cases (18_101 − 18_104) range between 0.857 and 1.000 depending on roof zone and slope.

In contrast, the minimum 1 year survival probability for code engineered 1-D (90_101 and 90_102) and 2-D (180_101 − 270_102) system is 0.999 and 0.995 respectively. Further, the experimental results suggest, each of the 1-D and 2-D design cases have a 1.000 chance of survival, when installed on a 15 degree and 30 degree roof.

Table 13: Survival probabilities for design cases engineered for 90 mph wind zone

	15 deg		30 deg		45 deg	
Design Case	1 year	25 year	1 year	25 year	1 year	25 Year
18_101	0.990	0.778	0.999	0.975	0.963	0.390
18_102	1.000	1.000	0.997	0.928	0.957	0.333
18_103	0.910	0.095	0.943	0.231	0.953	0.300
18_104	0.990	0.778	0.963	0.390	0.857	0.021
_90_101	1.000	1.000	1.000	1.000	0.999	0.975
90_102	1.000	1.000	1.000	1.000	1.000	1.000
180_101	1.000	1.000	1.000	1.000	0.995	0.882
180_102	1.000	1.000	1.000	1.000	0.998	0.951
270_101	1.000	1.000	1.000	1.000	0.998	0.951
270_102	1.000	1.000	1.000	1.000	1.000	1.000

Discussion of Results

A comparison of alternative system types is made through statistical analysis of the 25 year survival rates for alternative systems types with a fixed roof angle. A T-Test is used with the null hypothesis that there is no difference between sample means. 1-D and 2-D systems have $P > 0.05$ indicating that the null hypothesis can not be rejected and the survival rates for the two systems types are statistically similar. Next, comparison is made between 0-D samples and the combined set of 1-D and 2-D samples. For each roof angle, $P < 0.05$ (P=0.03 for 15°, P=0.02 for 30°, and P=0.002 for 45°) indicating a statistical difference between system types and supporting rejection of the null hypothesis.

In order to assess the consistency in reliability of code engineered systems applied to varying roof angles, paired T-Test are used to compare the reliability of each design case across roof angles with the null hypothesis indicating no statistical difference in means between roof angles. In comparison of the 25 year probability of survival for design cases installed on a 15° roof to a 30° roof, the null hypothesis could not be rejected due to $p = 0.4$. However, comparison of probability of survival for design cases installed on a 15° roof to a 45° roof as well as a 30° roof to a 45° roof resulted in $p = 0.048$ and $p = 0.03$ respectively. These results allow rejection of the null hypothesis and suggest that code engineered PV systems have statistically different 25 year reliability depending on the roof angle.

These finding support the sub-hypothesis that a coupled reliability model provides a platform for comparing alternative system types. Further, the findings suggest a statistical difference in reliability of code engineered residential PV systems across system types and also across roof angles.

Next, comparison of system reliability to a reliability target requires a benchmark reliability target and calculation of the percent above or below the reliability target. The E.U. building code, EN1990, provide for a reliability approach with quantified

β reliability targets. EN1990 establishes reliability targets for three Reliability class' (RC) that correspond to three consequence classes (CC) (Table 14). Each consequence class from CC1 to CC3 corresponds to increasingly higher risk to human life with CC2 defined as medium risk typically found in residential or commercial buildings. However, loss of life is not the only consequence of concern captured in the Eurocode, each consequence class is also defined in terms of the capacity for economic, social or environmental impact [3]. More recently, ASCE 7-10 published acceptable 1 year β values that may be used in lieu of the more established EN1990 values. For reference, a system installed in occupancy category II (residential) with sudden or wide spread failure is permitted a minimum β value of 3.5.

Table 14: EN 1990 minimum reliability index, β by reliability class [3]

Reliability Class	1 year reference period	50 year reference period
RC3	5.2	4.3
RC2	4.7	3.8
RC1	4.2	3.3

As shown, the reliability target is not based on the survival probability but rather the reliability index, β. One limitations of the survival probability is illustrated by considering a survival probability of 1.000 as calculated for multiple design cases. For this case there is limited ability to interpret how reliable the system is compared to a high reliability benchmark given the quantified uncertainty. This limitation is graphically illustrated by Figure 62 which shows a clear failure region for 18_101 where the load probability distribution function (pdf) exceeds the resistance pdf; the 1 year survival rate for this case is 0.99. In contrast, there is no clear failure region illustrated for 90_101 or 180_101 both of these have a 1 year survival rate of 1.000 yet there is a clear visual difference in reliability because the standard deviation of loads for 180_101 is less than the standard deviation of loads for 90_101. This case illustrates the value of the the reliability index β used to establish reliability performance targets by accounting for the difference in means and the standard deviations,

as shown in Equation 55 [29].

$$\beta = \frac{\mu_R - \mu_S}{\sqrt{\sigma_R^2 + \sigma_S^2}} \tag{55}$$

To benchmark the reliability of each design case and roof angle calculation, β_1 is calculated using equation 55 and compared against the target reliability index for residential consequence class, RC2 in Figure 63. In practice, a design professional is restricted by code from having a reliability less than the target, and for economic reasons may minimize the degree to which the target is exceeded. However, for the purpose of bench marking a tolerance range is established by setting RC1 as a lower limit and RC3 as an upper limit. These upper and lower specs are relevant in the context of perspectives that place a greater importance on energy infrastructure as well as perspectives that account for actual pedestrian behavior during storm events. Grouping of each roof angle for a design case clearly confirms the trends identified by reviewing the survival rates. Further, Figure 63 shows that for all 0-D design cases except a single 15° roof case, neither the target reliability, RC2 or the RC1 reliability are met. On the other hand, each of the 1-D and 2-D design case exceed the target reliability for 15° and 30° roofs while 66% are below the target reliability when installed on a 45° roof. Among the systems that exceed the target reliability, β for 2-D cases compared to the 1-D cases supports the conclusion that 2-D cases are significantly over-engineered compared to both the target reliability and 1-D cases ($p = 0.0005$). If the ASCE value is a preferred target, similar trends hold with 4 of the 12 O-D systems exceeding the target performance and all of the 1-D and 2-D systems meeting or exceeding the target value.

For benchmarking reliability over periods other than 1 year the target β_n for a n year period can be calculated from the $1 - year$ β target, β_1 according to Equation 56.

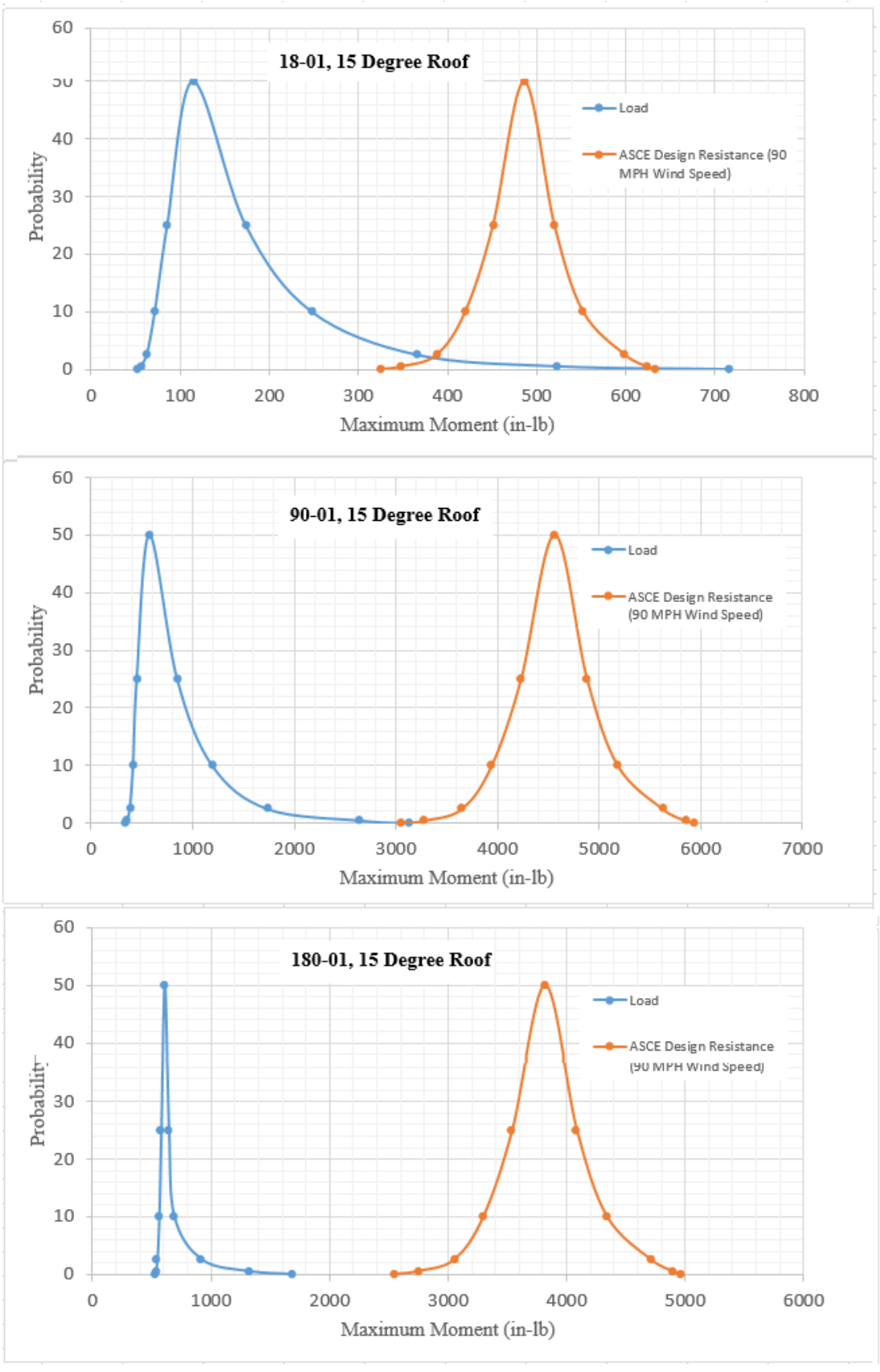

Figure 62: Frequency Distribution of Atlanta annual maximum 3-second gust

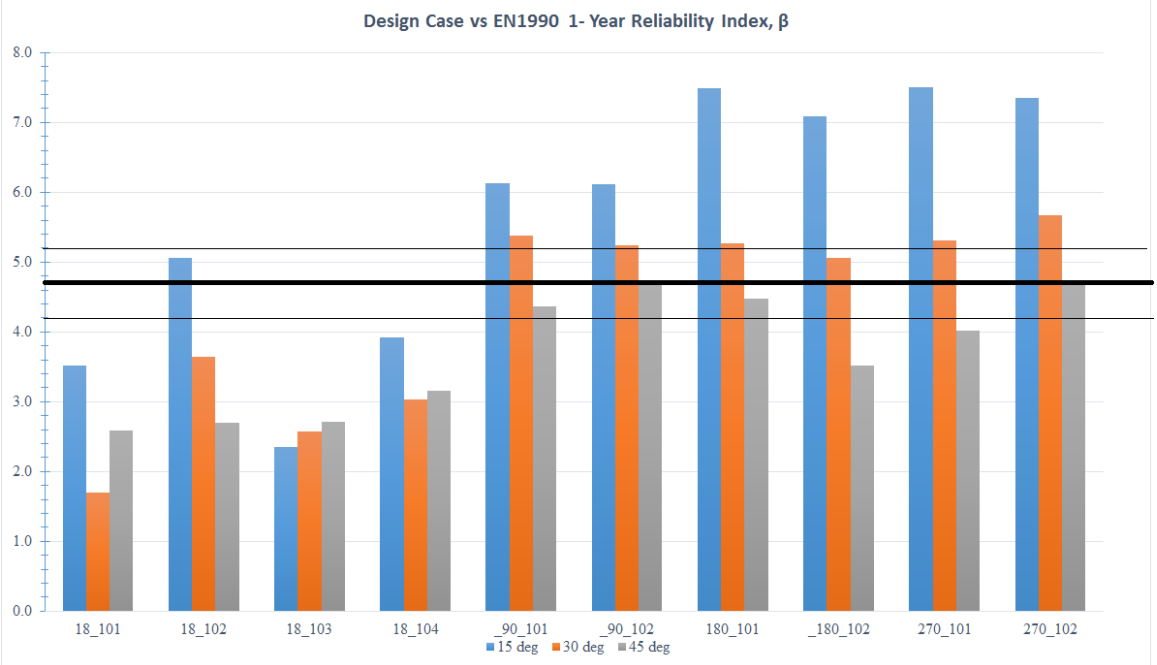

Figure 63: Reliability index, β_1 for limit state #1 for each design case in the Atlanta case study. Benchmark target reliability values are illustrated for reliability class, RC, 2 with upper spec RC3 and lower spec RC1.

$$\Phi(\beta_n) = [\Phi(\beta_1)]^n \tag{56}$$

CHAPTER VI

SUMMARY, CONCLUSIONS AND FUTURE WORK

6.1 Summary

Recent investigations into wind loads on residential PV systems suggest actual wind loads may vary considerably compared to wind loads prescribed by recommended codified methods. In other words, the ASCE 7-2005 and ASCE 7-2010 codes does not appear to be calibrated with actual pressure coefficient on currently system types. Further, recently developed racking system types have introduced an order of magnitude variation in influence areas (1 to 10 Module areas), a parameters known to impact wind loads. The current mis-calibration does not appear to be uniform across system types. In combination, three potential consequences exist. 1) The structural risk of a code engineered system is not adequately quantified to support risk based decisions. 2) Actual structural risk may not be consistent with the level of risk intended by code. 3) Structural risk may not be consistent across system types and building geometries. Mitigation of these consequences requires better tools and understanding of residential PV structural reliability. For this purpose, general methodologies to assess fragility and structural reliability have been proposed for application as structural performance measures for residential PV systems. Through a series of case studies these two performance measures have been shown to work in concert by first assessing the conditional failure probability and then incorporating site specific extreme wind speed models. In order to demonstrate the fragility and reliability index methodologies, initial limit states for performance based design have been drafted even though understanding of structural supply is well established and not the focus of this thesis. Demonstration of fragility and reliability index methods completed

through the case studies presented in this thesis have quantified the probability of a limit state (LS#1) failure for systems engineered according to the ASCE code 90mph wind zones. Alternatively, the demonstrated methodology is readily applicable to systems engineered according to industry standards.

The Fragility analysis accounted for uncertainties in both the dynamic pressure prediction and material strength prediction. Sources of model form uncertainty were identified but not quantitatively incorporated. Because a limited set of publications suggested actual wind pressure coefficients on residential PV systems may be inconsistent with code prescribed values, wind tunnel testing was conducted to reduce epistemic uncertainty. Incorporation of the experimentally derived pressure coefficients into revised fragility curves yielded statistically significant inconsistencies between system types and roof conditions. Subsequently, the fragility curves were coupled with site specific extreme wind speed models in the reliability index β. The proposed approach demonstrated use of Gumbel distribution to model historic extreme wind speeds. The Gumbel distribution was then sampled to create a synthetic set of extreme wind speeds for use in Monte Carlo simulation.

6.2 Conclusions

Fragility analysis can be used to quantitatively assess the probability of a structural limit state failure for a code engineered system across an array of wind speeds. Incorporation of uncertainties that influence the resistance and load effects is critical for a complete fragility analysis. Fragility analysis has shown a significant difference in the probability of failure for alternative code engineered system types given a design wind speed event. However, fragility analysis has also shown that when any of the system types are engineered according to code for 90 mph wind zone, the probability of $LS\#1$ failure in a wind event 70 mph or less is near zero. These findings demonstrate the importance of a single reliability measure to assess the probability of

failure during a systems service life. Treatment of the annual extreme wind speed as a random variable described by the Gumbel distribution supported a coupled model capable of predicting the reliability in 1 year or multiple years. Significant differences in the 25 year probability of failure were found due to system type and roof angle. Use of probability of failure as a metric was found to have limited capability to differentiate between systems with near zero probability of failure. Alternatively, the reliability index β was found to be a more descriptive metric capable of clearly differentiating between two reliable systems. Comparison of the calculated β values for each system type roof angle combination indicated significant differences in reliability predictions across system types and roof angles. Benchmarking the calculated β values against performance targets set by EN1990 and ASCE indicated poor precision of the current perspective code when implemented according to recent industry recommendations. Predicted reliability for the generalized $O-D$ system types is less than the performance targets for all consequence classes suggesting these systems might be under-engineered when engineered according to code. The generalized $1-D$ and $2-D$ systems are predicted to have reliability greater than the target spec for residential structures when installed on 15° and 30° roofs but less than the target when installed on 45° roofs. These findings do successfully demonstrate and motivate the proposed performance measures. They do not support analysis of any specific commercially available systems because of two critical limitations. 1) Neither the geometry or the structure design method is intended as an exact representation of commercially available system, in fact significant deviations must be expected. 2) The wind tunnel testing and analysis methods utilized recently developed methods for small buildings. The wind tunnel method has been subject to only limited peer review and may introduce additional uncertainty. Despite these significant limitations, the results are adequately compelling to suggest that fragility curves and the reliability index each plays a useful role in quantifying the structural performance of

residential PV systems.

6.3 Next steps

Opportunities exist to both refine and expand upon this body of thesis. Refinements may be made through incorporation of additional sources of uncertainty including construction quality, and model form uncertainty. Repetition should be made of the wind tunnel testing in alternative wind tunnels with an expanded design of experiment incorporating additional geometries and features in an effort to gain expert consensus. Limit state definitions may be advanced and additional limit states should be incorporated through systems reliability methods. Expanded limit states should include serviceability limit states which address PV production. Also, PV racking system designers and manufacturers may be engaged to understand if additional safety factors or alternative measures or procedures such as testing are in place that may suggest actual reliability values deviate from predicted values.

Together, these refinement activities may support a longer term effort to update future code revisions with more accurate wind pressure coefficients. However, because the conclusions suggest that code has failed to provide a consistent level of reliability across system types, code committee members may consider if a prescriptive code remains preferable or whether the proposed performance based reliability engineered methods should be promoted. Further, this thesis has assumed that structural reliability intended by the ASCE code and targeted in the E.U. code are appropriate targets for power generation equipment. Currently, the switch to solar energy is being motivated by financial performance and risk from existing power generation technologies. Future work should use a life cycle assessment methodology to compare the full life cycle effects of alternative power generation technologies [27], [61]. This analysis should support determination of how much reduction in risk should code require of solar when replacing a high risk alternative such as coal power generation. Ideally,

this decision should also incorporate the marginal cost of risk reduction and marginal adoption rates. One possible scenario is that a higher level of risk from PV systems may be accepted so that more severe global warming risk and air quality risk [68], [69] may be mitigated faster. Already the metric lives lost per trillion kWh enables consistent comparison of risk across system types. Another area of investigation required for improved risk assessment and risk based decision making is a more rational mapping of limit states to damage levels. Speculation in the literature has suggested lives lost due to structural failure of a solar panel system during an extreme wind event may be low because people tend to go inside. Clearly in our present state of increasingly complex hazards the role of the building safety code must evolve. A modest starting point is improved transparency of the structural performance derived from engineering systems according to code.

CHAPTER VII

BIBLIOGRAPHY

Bibliography

[1] *UL 2703: Outline of Investigation for Mounting Systems, Mounting Devices, Clamping/Retention Devices, and Ground Lugs for Use with Flat-Plate Photovoltaic Modules and Panels*. UL Standards, 2 ed.

[2] "General principles on reliability for structures," The International Organization for Standardization, 1998.

[3] "EN 1990 Eurocode - Basis of Structural Design," Tech. Rep. BS EN 1990:2002+A1:2005 EN 1990:2002+A1:2005, Eurocode, 2002.

[4] *UL 1703: Standard for Flat-Plate Photovoltaic Modules and Panels*. UL, 3rd ed., 2002.

[5] "Development of skills facilitating implementation of eurocodes," ch. Handbook 2 Reliability Backgrounds, Prague: Leonardo da Vinci Pilot Project CZ/02/B/F/PP-134007, April 2004.

[6] "Development of skills facilitating implementation of eurocodes," ch. Handbook 1 Basis of Structural Design, Prague: Leonardo da Vinci Pilot Project CZ/02/B/F/PP-134007, October 2005.

[7] "North american specification for the design of cold-formed steel structural members," tech. rep., American Iron and Steel Institute, 2007.

[8] "Extreme value distribution," National Institute of Science of Technology, 2014.

[9] "Photovoltaics Report," tech. rep., Fraunhofer Institute For Solar Energy Systems ISE, Freiburg, October 2014.

[10] "Wall of Wind Testing of Photovoltaic (PV) Systems," tech. rep., September 2014.

[11] ASCE, *Minimum design loads for buildings and other structures*, vol. ASCE 7-05. Reston, VA: American Society of Civil Engineers, 2005.

[12] ASCE, *Minimum design loads for buildings and other structures*, vol. ASCE 7-10. Reston, VA: American Society of Civil Engineers, 2010.

[13] ASCE, *Wind Tunnel Testing For Buildings and Other Structures, 49-12*. American Society of Civil Engineers, 2012.

[14] Ayyub, B. and Haldar, A., "Practical structural reliability techniques," *Journal of Structural Engineering*, vol. 110, no. 8, p. 17071724, 1984.

[15] Baker, J., "Structural reliability course notes," Palo Alto: Stanford University, 2015.

[16] Banks, D., "The Role of Corner Vortices in Dictating Peak Wind Loads on Tilted Flat Solar Panels Mounted on Large, Flat Roofs," *Journal of Wind Engineering and Industrial Aerodynamics*, no. 123, pp. 192–201, 2013.

[17] Barkaszi, S. and O'Brien, C., "Wind load calculations for pv arrays," *Solar American Board for Codes and Standards Report*, June 2010.

[18] Bony, L., Doig, S., Hart, C., Maurer, E., and Newman, S., "Achieving low-cost solar PV: Industry workshop recommendations for near-term balance of system cost reductions," tech. rep., Rocky Mountain Institute, 2010.

[19] Bronkhorst, A., "Wind Tunnel and CFD modeling of Wind Pressures on Solar Energy Systems on Flat Roofs," *Computational Wind Engineering*, 2010.

[20] Browne, M. T., Gibbons, M. P., Gamble, S., and Galsworthy, J., "Wind loading on tilted roof-top solar arrays: The parapet effect," *Journal of Wind Engineering and Industrial Aerodynmics*, vol. 123, pp. 202–213.

[21] Ciampoli, M., "Performance-Based Wind Engineering: Towards a general procedure," *Structural Safety*, vol. 33, pp. 367–378, 2011.

[22] Cinnamon Solar, "Solar panels last 25 years - but will they stay safely attached to your roof?," pp. 1–25, Cinnamon Solar and Solar Marketing Group LLC, 2014.

[23] Coates, R. C., *Structural Analysis, Third Edition*. London: Chapman and Hall, 1998.

[24] Corporation, S., "Suniva," 2014.

[25] Corporation, S., "Sunlink," 2014.

[26] Council, A. T., "Seismic Performance Assessment of Buildings methodology fema p-58-1," vol. 1, September 2012.

[27] Curran, M., "Life Cycle Assessment, Chapter 13," *Elsevier BV*, pp. 2168–2174, 2008.

[28] Department of Energy, "Solar Innovation Timeline,"

[29] Ditlevsen, O. and Madsen, H. O., *Structural Reliability Methods*. Chichester: John Wiley & Sons Ltd, 1996.

[30] Duke Energy, "Enhancing the development of solar technologies in florida," tech. rep., Duke Energy, St. Petersburg Florida, June 2015.

[31] Ellingwood, B., *Development of a probability based load criterion for American National Standard A58: Building code requirements for minimum design loads in buildings and other structures*, vol. 577. 1980.

[32] Ellingwood, B., "Probability based load criteria for structural design," tech. rep., National Institute of Standards and Technology, Washington, D.C., 2001.

[33] Ellingwood, B. and Tekie, P., "Wind Load Statistics for Probability Based Design," *Journal of Structural Engineering*, vol. 125, April 1999.

[34] Erwin, J., "Full Scale and Wind Tunnel Testing of a Photovoltaic Panel Mounted on Residential Roofs," *Advances in Hurricane Engineering*, pp. 471–482, November 2012.

[35] Faber, M. H., "11th Lecture: Methods of Structural Reliability Analysis," 2006-2007.

[36] Fu, T.-C., Chowdhury, A., Bitsuamlak, G., and Baheru, T., "Partial turbulance simulation and aerodynamic pressure validation for an open-jet testing facility," *Journal of Wind and Structures*, vol. 19.1, pp. 15–33, 2014.

[37] G Kopp and D Banks and J Maffei and R LaPlante and K Telleen, "Asce 7-16 solar#2revised," tech. rep., ASCE, Reston Virginia, April 2013.

[38] Geurts, C. and Blackmore, P., "Wind Loads on Stand-off Photovoltaic Systems on Pitched Roofs," *Journal of Wind Engineering and Industrial Aerodynamics*, vol. 123, pp. 239–249, 2013.

[39] Giorges, A. T., "Numerical simulation of aerodynamic force on solar modules," 2013.

[40] Guerts, C. P. W. and Steenbergen, R. D. J. M., "Full scale measurements of wind loads on stand-off photovoltaic systems," 2009.

[41] Hamburger, R. O., "A Framework for Performance-Based Earthquake Resistive Design," January 31-February 1 1997.

[42] Hammersley, J. M. and Handscomb, D. C., *Monte Carlo Methods*. London: Methuen & CO Ltd, 1964.

[43] Hoerner, S., "Fluid Dynamic Drag," 1965.

[44] inc, R. T., "Roof tech," 2014.

[45] Inc", S. I., "Using JMP 10," 2012.

[46] Isyumov, N., *Wind Studies of Buildings and Structures (ASCE 67)*. American Society of Civil Engineers, 1999.

[47] Juan, A. A., Monteforte, A., Ferrer, A., and Faulin, J., "Applications of Discrete-Event Simulation to Reliability and Avabilability Assessment in Civil Engineering Structures," Proceedings of the 2009 Winter Simulation Conference in Austin: IEEE, 2009.

[48] Kaimal, J. C. and Finnegan, J. J., "Atmospheric Boundary Layer Flows: Their Structure and Measurement," New York: Oxford University Press.

[49] Kann, S., Shiao, M., Mehta, S., Honeyman, C., Litvak, N., and Jones, J., "GTM Research/SEIA: U.S. solar Market Insight," pp. 6–16, Greentech Media Inc and Solar Energy Industries Association.

[50] Kijewski-Correa, T., Kilpatrick, J., Kareem, A., Kwon, D., Bashor, R., Kochly, M., Young, B., Abdelrazaq, A., Galsworth, J., Isyumov, N., Morrish, D., Sinn, R., and Baker, W., "Validating wind-induced response of tall buildings: Synopsis of the chicago full-scale monitoring program," *Journal of Structural Engineering*, vol. 132, no. 10, pp. 1509–1523, 2006.

[51] Kolios, A. and Proia, S., "Evaluation of the reliability performance of failure criteria for composite structures," *World Journal of Mechanics*, vol. 2, no. 3, pp. 162–170, 2012.

[52] Kopp, G. A., "Wind loads on low profile tilted solar arrays placed on low-rise building roofs," 2013.

[53] Kopp, G. A., "Wind Loads on Low-Profile, Tilted, Solar Arrays Placed on Large, Flat, Low-Rise Building Roofs," *Journal of Structural Engineering*, vol. 140, no. 2, 2013.

[54] Kuitche, J. M. and Pan, R., "Investigation of Dominant Failure Mode(s) for Field-Aged Crystalline Silicon PV Modules Under Desert Climatic Conditions," *IEEE Journal of Photovoltaics*, vol. 4, May 2014.

[55] Lee, Y., "Pitched-Roof PV Mounting: Design and Engineering Considerations," Feb/Mar 2010.

[56] Lemos, D. F. A., Pereira, A. L., and Feitosa, E. A. N., "Influence of the Weibull Parameters on the Estimation of Wind Turbine Loads," 2006.

[57] Meroney, R. N. and Neff, D. E., "Wind Effects on Roof-Mounted Solar Photovoltaic Arrays: CFD and Wind Tunnel Evaluation," *Computational Wind Engineering*, 2010.

[58] Mooneghi, M. A., Irwin, P., and Chowdhury, A., "Partial turbulence simulation for small structures," 2015.

[59] Morris, J., Calhoun, K., and Seif, D., "Reducing Solar PV Soft Costs, A Focus on Installation Labor," tech. rep., Rocky Mountain Institute, December 2013.

[60] Murphy, L. M., "An Assessment of Existing Studies on Wind Loading on Solar Collectors," tech. rep., 1981.

[61] NREL, "Life Cycle Assessments of Energy Technologies," 2013.

[62] Peterka, J. and Shahid, S., "Design Gust Wind Speeds in the United States," *Journal of Structural Engineering*, vol. 124, no. 2, pp. 207–214, 1998.

[63] Peterka, J. A., "Design Wind Loads for Wind Power Applications," tech. rep., CPP Inc, Fort Collins, 2008.

[64] Rahim, M., "Effects of Global Warming on the Average Wind Speed Field in Central Japan," *Journal of Sustainable Energy & Environment*, vol. 3, pp. 165–171, 2012.

[65] Rosowky, M. and Ellingwood, B., "Performance-Based Engineering of Wood Frame Housing Fragility Analysis Methodology," *Journal of Structural Engineering*, vol. 128, pp. 32–38, January 2002.

[66] Sarkar, A., "Wind Climate Modeling Using Weibull and Extreme Value Distributions," *International Journal of Engineering Science and Technology*, vol. 3, no. 5, pp. 100–106, 2011.

[67] Schafer, B. W., "The Direct Strength Method of Cold-Formed Steel Member Design," *Journal of Construction Steel Research*, vol. 64, pp. 766–778, 2008.

[68] Skone, T., "Life cycle analysis of natural gas extraction and power generation," 1617 Cole Boulevard Golden, Colorado 80401: Department of Energy, National Renewable Energy Laboratory, May 2014.

[69] Spath, P. L., Mann, M. K., and Kerr, D. R., "Life cycle assessment of coal-fired power production," 1617 Cole Boulevard Golden, Colorado 80401: National Renewable Energy Laboratory, June 1999.

[70] Stathopulos, T., "Wind Loads on Solar Collectors and PV Panels on Roofs," Pittsburgh: ASCE Structures Congress, 2013.

[71] Stenabaugh, S., Lida, Y., Kopp, G., and Karava, P., "Wind Loads on Photovoltaic Arrays Mounted Parallel to Sloped Roofs on Low-rise Buildings,"

Journal of Wind Engineering and Industrial Aerodynamics, no. 139, pp. 16–26, 2015.

[72] Sun, Y., Su, H., Wu, C., and Augenbroe, G., "Quantification of model form uncertainty in the calculation of solar diffuse irradiation on inclined surfaces for building energy simulation," *Journal of Building Performance Simulation*, vol. 8, pp. 253–265, 2015.

[73] Sunshot Systems Integration Group, "Extreme balance of system cost out reduction funding opportunity announcement," tech. rep., Department of Energy, Washington D.C., April 2011.

[74] TamizMani, G. and Kuitche, J., "Accelerated lifetime testing of photovoltaic modules solar america board for codes and standards," Solar America Board for Codes and Standards, July 2013.

[75] van de lindt, J., Amini, M. O., Standohar-Alfano, C., and Dao, T., "Systematic study of the failure of a light-frame wood roof in a tornadao," *Buildings*, pp. 519–533, December 2012.

[76] Verderaime, V., "Structural determinister safety factors selection criteria and verification," Washington D.C.: National Aeronautics and Space Adminisitration, Office of Management, Scientific and Technical Information Program, 1992.

[77] Wind Subcommittee on Solar Photovoltaic Systems, S., "Wind Loads on Low Profile Solar Photovoltaic Systems on Flat Roofs," tech. rep., Structural Engineers Association of California, 2012.

[78] Zepsolar, "Instruction Manual for Composition Shingle Roofs- u.s.," September 2013.

[79] Zilla, "Solar Racking Systems and Solutions," 2014.